UNIVERSITÀ
DEGLI STUDI
DI PADOVA

University of Padova

Department of Management and Engineering

PhD School in Mechatronics and Product Innovation Engineering

Curriculum: Mechanics of Materials

Cycle XXXI

METALLURGICAL AND MECHANICAL CHARACTERIZATION OF STANDARD AND NEW GENERATION CAST IRONS

Thesis written with the financial contribution of VDP Fonderia S.p.A.

Coordinator: Prof. Daria Battini

Supervisor: Ch.mo Prof. Paolo Ferro

Ph.D. Candidate: Thomas Borsato

September, 2018

UNIVERSITÀ
DEGLI STUDI
DI PADOVA

Università degli Studi di Padova

Dipartimento di Tecnica e Gestione dei Sistemi Industriali

Scuola di Dottorato di Ricerca in Ingegneria Meccatronica e
dell'Innovazione Meccanica del Prodotto
Curriculum: Meccanica dei Materiali
Ciclo XXXI

CARATTERIZZAZIONE METALLURGICA E MECCANICA DI GHISE TRADIZIONALI E DI NUOVA GENERAZIONE

Tesi scritta con il supporto finanziario di VDP Fonderia S.p.A.

Direttore della Scuola: Prof. Daria Battini

Supervisore: Ch.mo Prof. Paolo Ferro

Dottorando: Thomas Borsato

Settembre, 2018

Table of Contents

List of Figures

List of Tables

Abstract

The demand for ductile cast iron components, with weights ranging from a few kilograms to several tons, has increased significantly in recent years, both for technical and economic reasons. In fact, the lower cost compared to other materials, the good castability, which allows to obtain near-net shape components in as-cast conditions, and the mechanical properties that can be obtained, are just some of the motivations that attract mechanical designers.

In the case of large components, the knowledge of mechanical behaviour is however limited and incomplete. What is known is that, by increasing the thicknesses of the castings, the solidification times increase and the cooling rates are greatly reduced. In these critical conditions, solidification can lead to the formation of microstructural defects, sometimes unavoidable, which negatively influence the local mechanical properties of ductile cast iron components.

From an initial and in-depth bibliographic analysis, it emerged that, in literature, these issues have been studied in a systematic way only in the recent years. As a result, the number of data available for engineers is limited and it can be noted that there are many lacks, especially with regard to the mechanical characterization and fatigue behaviour of these materials. Specifically, most of the work has been carried out considering traditional ferritic ductile iron used, for example, in the production of wind turbine components. In some studies, traditional cast irons with pearlitic matrix have been characterized, while the data concerning the mechanical and microstructural properties of new-generation cast irons with a solid solution strengthened ferritic matrix are very limited.

The *First Chapter* contains a brief introduction concerning the above mentioned topics, with particular attention to the state of the art and to the recent works published in the literature

The *Second Chapter* describes the experimental campaign conducted during the doctorate, following which an in-depth microstructural and mechanical characterization of different types of spheroidal cast iron characterized by different conditions of cooling and solidification was carried out. During the experimental campaigns, microstructural analyses were performed using an optical microscope and image analysis software on polished and etched samples. In addition, tensile and fatigue tests were performed on specimens obtained from the areas of interest within the castings. The fracture surfaces were then analysed by SEM to identify the causes of fracture.

In the *Third Chapter* the most significant experimental results obtained from the microstructural and mechanical characterization of a traditional ferritic matrix iron are reported. The aim is to expand the literature with further experimental data on this type of material in specific cooling and solidification conditions.

In the *Fourth Chapter*, because of the few works in the literature, cast iron with pearlitic matrix was studied. In particular, through the realization of three experiments, the effect that the post-inoculation process have on the microstructural parameters and on the mechanical properties has been investigated.

In the *Fifth Chapter*, the results obtained on new-generation solution strengthened ferritic ductile irons are reported. In particular, the effect of different amount of silicon and antimony on the properties of castings characterized by long solidification times has been investigated.

In the *Sixth Chapter*, the microstructural, mechanical and fatigue properties of a particular grade of solution strengthened ferritic ductile iron have been evaluated as a function of different section thicknesses and solidification times.

In the *Seventh Chapter*, a model that allows estimating the fatigue strength of as-cast ductile irons containing solidification defects is proposed based on the new experimental data.

The *Eighth Chapter* presents concluding remarks on the work in order to discuss the main results.

Sommario

La domanda di componenti in ghisa sferoidale, con pesi che variano da pochi chilogrammi diverse tonnellate, è aumentata di molto negli ultimi anni, per motivi sia tecnici che economici. Infatti, il più basso costo rispetto ad altri materiali, la buona colabilità, che permette di ottenere componenti near-net shape nelle condizioni as-cast, e le proprietà meccaniche che si possono ottenere, sono solo alcune delle motivazioni che attraggono i progettisti meccanici.

Nel caso di componenti di notevoli dimensioni, la conoscenza del comportamento meccanico è però limitata e incompleta. Quello che è noto è che, aumentando gli spessori dei getti, aumentano di conseguenza i tempi di solidificazione e si riducono di molto le velocità di raffreddamento. In queste condizioni critiche, le condizioni di solidificazione possono portare alla formazione di difetti microstrutturali, a volte inevitabili, che vanno a influenzare negativamente le proprietà meccaniche locali dei componenti in ghisa sferoidale.

Da una iniziale e approfondita analisi bibliografica è emerso come, in letteratura, questi temi siano stati studiati in maniera sistematica soltanto negli ultimi anni. Di conseguenza, il numero di lavori presenti nei database e a disposizione degli ingegneri progettisti è tutt'altro che ampio e si nota come siano presenti numerose lacune, specialmente per quanto riguarda la caratterizzazione meccanica e il comportamento a fatica di questi materiali. Nello specifico, la maggior parte dei lavori sono stati svolti considerando ghise tradizionali a matrice ferritica impiegate ad esempio in componenti utilizzati per lo sfruttamento dell'energia eolica. In alcuni studi sono state effettuate delle caratterizzazioni di ghise tradizionali a matrice perlitica, mentre sono molto limitati i dati che riguardano le proprietà meccaniche e microstrutturali di ghise di nuova generazione, a matrice ferritica rafforzata per soluzione solida.

Nel *Primo Capitolo* viene riportata una breve introduzione riguardante le tematiche sopracitate, con particolare attenzione allo stato dell'arte e ai recenti lavori pubblicati in letteratura.

Nel *Secondo Capitolo* viene descritta la campagna sperimentale condotta durante il dottorato, seguendo la quale si è svolta una approfondita caratterizzazione microstrutturale e meccanica di diverse tipologie di ghisa sferoidale contraddistinte da diverse condizioni di raffreddamento e solidificazione. Durante le campagne sperimentali condotte sono stati eseguiti controlli microstrutturali utilizzando microscopio ottico e software di analisi di immagine su campioni lucidati e attaccati. Inoltre si sono eseguiti test di trazione e fatica su provini ricavati dalle zone di interesse all'interno dei getti. Le superfici di frattura sono state quindi analizzate al SEM per individuare le cause di innesco della frattura.

Nel *Terzo Capitolo* sono riportati i risultati sperimentali più significativi ottenuti dalla caratterizzazione microstrutturale e meccanica di una ghisa tradizionale a matrice ferritica, con lo scopo di ampliare la letteratura con ulteriori dati sperimentali su questa tipologia di materiale in specifiche condizioni di raffreddamento e solidificazione.

Nel *Quarto Capitolo*, a causa dei pochi lavori presenti in letteratura, si sono studiate ghise a matrice perlitica. In particolare, tramite la realizzazione di tre sperimentazioni, si è voluto indagare l'effetto che il processo di post-inoculazione può avere sui parametri microstrutturali e sulle proprietà meccaniche.

Nel *Quinto Capitolo*, sono riportati i risultati ottenuti su ghise di nuova generazione rafforzate per soluzione solida. In particolare si è condotto uno studio riguardante l'effetto dell'aggiunta di silicio e antimonio sulle proprietà di getti aventi lunghi tempi di solidificazione.

Nel *Sesto Capitolo*, sono state valutate le proprietà microstrutturali, meccaniche e a fatica di un particolare grado di ghisa ferritica rafforzata per soluzione solida in funzione di differenti sezioni e tempi di solidificazione.

Nel *Settimo Capitolo* viene proposto, sulla base dei risultati sperimentali, un modello in grado di stimare con una buona approssimazione la resistenza a fatica di diverse tipologie di ghisa sferoidale considerando le proprietà statiche locali e i difetti di solidificazione presenti all'interno dei getti.

Nell' *Ottavo Capitolo* sono riportate le osservazioni conclusive sul lavoro svolto e sui risultati più importanti ottenuti.

1. Introduction

1.1 Background and motivations

Over the last years, the production of heavy section ductile cast iron components with structural functions increased thanks to the relatively low manufacturing cost, excellent castability, and good combination of mechanical properties. The typical microstructure of as-cast ductile irons is characterized by spheroidal graphite particles dispersed within a metal matrix that can be ferritic, pearlitic, or ferritic/pearlitic, depending, for example, on the chemical composition of the alloy and on the cooling conditions.
It is well known that the ferritic matrix gives higher ductility and toughness, at the expense of ultimate tensile and yield stress. On the contrary, pearlitic ductile irons are characterized by high strength and hardness, but, due to the brittleness of pearlite, they do not reach high values of elongation at failure and fracture toughness. Finally, ferritic/pearlitic ductile irons are mix of the two previous alloys, with intermediate properties [1,2].

Recently, ductile irons with ferritic matrix strengthened by solid solution (SSF DI) through the addition of balanced amount of silicon have been introduced in the UNI EN 1563:2012 standard [3].
Ferritic ductile irons strengthened by silicon addition, have higher $Rp_{0.2\%}$/Rm ratio and higher elongation than conventional ferritic, ferritic/pearlitic and pearlitic ductile irons at the same level of tensile strength. SSF DI exhibit also very small hardness variation in the whole casting due to their single-phase metal matrix. This uniform hardness results in improved machinability and low tool wear [4]. The influence of silicon content on the static mechanical properties have been investigated in the past [5]. It has been found that, starting from 2.4 wt% Si, the tensile strength increases until 4.3 wt% Si is reached. Above this silicon content, the tensile strength and elongation at failure start to decrease. The yield strength

decreases when silicon content is higher than 4.6%. It was also observed that at 5% Si the yield strength and tensile strength coincide. Also in some recent references it was observed that, when silicon content is increased up to 4.3%, ultimate tensile strength, yield strength and hardness increase, while elongation at failure, Charpy energy and fracture toughness decrease [6–8]. This is due to the decrease in plasticity and increase embrittlement of ferrite strengthened by solid solution [9]. A comparison of mechanical properties between a ferritic/pearlitic grade and a solution strengthened ferritic ductile iron has been recently made [10]. It has been found that the new grade has double elongation at failure with respect to the traditional one at the same tensile strength, and improved hardness range across a casting section, that leads to high machinability and cost savings. This was observed also in other recent works taken from the literature [11–13]. As reported above, an upper limit exists on the silicon content. This behaviour is due to the decrease in plasticity and increase of embrittlement of solid solution–strengthened ferrite. In a study of Weiss et al [14] ductile irons with silicon contents varying between 3.95 and 5.63 wt% have been investigated using transmission electron microscopy diffraction. It has been found that the predominant cause for the embrittlement phenomena is due to the presence of B2 and $D0_3$-ordered phases in the matrix that strongly increases with the silicon content increasing.

In order to further improve the mechanical strength, the effect of potential additional solution strengthening elements has been investigated in literature [15–17]. In particular, the influence of nickel and cobalt on the microstructure has been studied. It was found that 4% cobalt increases the nodule count and ferrite content and also improves the mechanical properties, such as yield and tensile strength, impact and fracture toughness, as compared to unalloyed. In contrast, 4% nickel decreases nodule count and increases pearlite content in the microstructure, resulting in improved hardness, yield and ultimate strength but low ductility and toughness.

Ten years ago, Iacoviello et al. [18] investigated the microstructure influences on the damaging micromechanisms in traditional ductile irons by means of tensile tests and in situ SEM observations. On the basis of the experimental results, they found that both the graphite elements and the metal matrix play an important role during

the damage process. In particular, it was proposed that the graphite particles/metal matrix debonding is not the only damaging micromechanism, but also an "onion-like" damage mechanism exist. Moreover they observed that the matrix damaging differs changing the matrix structure.

By increasing the thickness of the components, the solidification times will increase with the increased risk of finding coarse grains and anomalous structures [19–22]. A parameter that is widely used for the control of the quality of ductile iron is the nodule count, defined as the ratio between the number of spheroidal graphite nodules and the observation area. The nodularity and the nodule count will decrease with decreasing cooling rates, while the dimensions of graphite particles will increase. Furthermore, the greater the casting dimensions, the greater the probability of finding degenerated graphite (exploded, chunky or spiky), large microshrinkage porosities, non-metallic inclusions or undesired segregations [23–26].

Segregations are due to the fact that in heavy sections, the distance between spheroids is greater and the last to freeze (LTF) areas become significantly larger. Most of the elements that segregate in these areas are the ones which promote carbides and enhance the stability of austenite; thus pearlite and carbides are formed.

Also microshrinkage porosities will form in the LTF regions because liquid metal solidify and other liquid can not fully reach those areas.

Among the different defects found in heavy-section DI casting, chunky graphite is certainly the more frequent. Chunky graphite forms at the thermal centre of heavy-section DI and appears macroscopically as black spots in the fracture or saw-cut surface. With particular reference to CHG, many studies were carried out in the past but no generally accepted theory for its formation has yet been proposed [27–36].

It is important to highlight that all these defects can be avoided only partially through the optimization of the production process (casting temperature, spheroidization or inoculation process, adjusted chemical composition, optimized pouring system). Consequently, especially in thick walled components, some defects are unavoidable.

For all these reasons, it is important to know the effects of microstructural defects on the mechanical properties of structural components made by ductile irons, especially regarding static and fatigue properties. In the case of ductile irons, the amount of works in literature is much more limited compared to other materials, and a lack of experimental data regarding the mechanical behaviour of heavy section components is present.

In some works in literature, the effect of various solidification defects on the mechanical and fatigue properties have been studied.

First of all, it has been observed that high nodule count increases the strength of pearlitic ductile irons, while increases the ductility in the case of ferritic matrix. Moreover, small nodules with high nodularity increase the low temperature impact energy.

High nodule count, decreases also the LTF regions, with associated lower segregations, carbides and porosities.

Canzar [37] showed experimentally that size, shape and distribution of the graphite nodules play a major role in the crack initiation and propagation process. It was also shown that the largest irregularly shaped nodules reduce the fracture toughness and the fatigue strength.

Iacoviello et al. [18,38–43] studied the influence of microstructure on the fatigue crack propagation resistance of different types of ductile cast iron with various matrix structure. They found that graphite particles do not only act as crack arresters but, depending on matrix microstructure, they can also increase the fatigue crack propagation resistance by means of an increase of the crack closure effect.

In the work of Sujakhu et al [44], the fatigue damage micromechanisms of SSF DI have been carefully studied. Based on the experimental observations, it was found that the crack initiation is affected by the degenerated graphite particles and casting defects, while the crack propagation stage is characterized by the interface decohesion between the spheroidal graphite and the ferritic matrix. During the final failure, the graphite particles behave like voids that grow and coalesce to form microcracks.

Mechanical properties and fatigue resistance of ductile irons is mainly controlled by the presence of casting defects such as microshrinkages or inclusions [45,46]
Nadot et al. [47,48] observed that crack initiation point is a single microporosity in proximity of the specimen surface. They also found that in uniaxial fatigue tests, the fatigue limit is much more sensitive to surface defects than internal defects. These results were confirmed in other works [49–59] where it was observed that microshrinkage cavities strongly influence the fatigue behaviour of ductile cast irons.
Endo et al. [60–64] confirmed that the largest defect, such as the maximum size of graphite particle, artificial notches, or casting defect (e.g., micro-shrinkage cavity) play a dominant role in determining fatigue strength of ductile cast irons.

Some researchers investigated the effect of chunky graphite on the mechanical and fatigue properties of heavy section ferritic ductile cast irons [65–67]. They found that this type of degenerated graphite morphology negatively affects the mechanical properties of the material; in particular it reduces the ultimate tensile strength and mostly the elongation to failure, without affecting the yield strength and the hardness. Moreover, it was found that also the fatigue strength is lowered by the presence of chunky graphite; while the graphite spheroids act as crack arresters, in the presence of chunky graphite, the cracks passes easily through the branched and interconnected graphite particles, lowering the fatigue strength of the material.
Some authors [5,17,24,68], have been studying the effect of increased Silicon content on the formation of microstructural defects. They concluded that by increasing the amount of Silicon, the tendency for chunky graphite formation also increases in the thermal centre of large castings, with detrimental effects on the mechanical properties. In particular, Källbom et al. [24] found that chunky graphite, similarly to traditional ductile irons, has a negative effect on ultimate tensile strength and elongation at failure, but does not affect the yield strength and hardness of solution strengthened ferritic ductile cast irons.

1.2 Purpose of the study

Due to the limited works in literature, the first purpose of this Ph.D. study was to partly fill the lack of experimental data regarding microstructural and mechanical characterization of heavy section castings characterized by long solidification times. The goal was to give the mechanical engineers some useful data for the correct design of load bearing components, made by using traditional or new generation ductile irons.

Another topic concerned the evaluation of the effect of microstructural defects on the mechanical behaviour of the alloys, especially regarding fatigue loading conditions.

The main objective was to provide the designers with a method that allows estimating, with good accuracy, the mechanical behaviour of components under fatigue cycling loading conditions.

References

[1] Davis JR. ASM specialty handbook: cast irons. ASM international; 1996.

[2] Labrecque C, Gagné M. Ductile Iron: Fifty Years of Continuous Development. Can Metall Q 1998;37:343–78.

[3] UNI EN 1563:2012, Founding - Spheroidal graphite cast irons.

[4] Larker R. Solution strenghened ferritic ductile iron ISO 1083/JS/500-10 provides superior Consistent properties in hydraulic rotators. China Foundry 2009;6:343–51.

[5] Stets W, Löblich H, Gassner G, Schumacher P. Solution Strengthened Ferritic Ductile Cast Iron Properties, Production and Application. Int J Met 2014;8:35–40. doi:10.1007/BF03355580.

[6] Glavas Z, Strkalj A, Stojakovic A. The properties of silicon alloyed ferritic ductile irons. Metalutgija 2016;55:293–6.

[7] de la Torre U, Loizaga A, Lacaze J, Sertucha J. As cast high silicon ductile irons with optimised mechanical properties and remarkable fatigue properties. Mater Sci Technol 2014;30:1425–31.

[8] Alhussein A, Risbet M, Bastien A, Chobaut JP, Balloy D, Favergeon J. Influence of silicon and addition elements on the mechanical behavior of ferritic ductile cast iron. Mater Sci Eng A 2014;605:222–8.

[9] Lin H, Lui T, Chen L. Effect of Silicon Content on Intergranular Embrittlement of Ferritic Spheroidal Graphite Cast Iron Suffered from Cyclic Heating. Mater Trans 2003;44:173–80. doi:10.2320/matertrans.44.173.

[10] Herfurth K, Gorski R, Beute K, Hering M. Cast material for mechanical engineering with higher strength and breaking elongation and highly homogeneous hardness distribution. http://www.gontermann-peipers.de/uploads/media/fachartikel_GOPAG_engl_01.pdf.

[11] Bjorkegren LE, Hamberg K, Johannesson B. Mechanical properties and machinability of Si-solution-hardened ferritic ductile iron. AFS Trans 1996;104:139–45.

[12] Björkegren LE, Hamberg K. Silicon alloyed ductile iron with excellent ductility and machinability. Proc. Keith Millis Symp., 2003.

[13] Kasvayee KA, Ghassemali E, Svensson IL, Olofsson J, Jarfors AEW. Characterization and modeling of the mechanical behavior of high silicon ductile iron. Mater Sci Eng A 2017;708:159–70. doi:10.1016/j.msea.2017.09.115.

[14] Weiß P, Tekavčič A, Bührig-Polaczek A. Mechanistic approach to new design concepts for high silicon ductile iron. Mater Sci Eng A 2018;713:67–74. doi:10.1016/j.msea.2017.12.012.

[15] Hsu C, Chen M, Hu C. Microstructure and mechanical properties of 4 % cobalt and nickel alloyed ductile irons. Mater Sci Eng A 2007;444:339–46.

[16] Weiß P, Brachmann J, Bührig-Polaczek A, Fischer SF. Influence of nickel and cobalt on microstructure of silicon solution strengthened ductile iron. Mater Sci Technol 2015;31:1479–85.

[17] Okunnu R. High Strength Solution-Strengthened Ferritic Ductile Cast Iron. Aalto University, 2015.

[18] Iacoviello F, Di Bartolomeo O, Di Cocco V, Piacente V. Damaging micromechanisms in ferritic–pearlitic ductile cast irons. Mater Sci Eng A 2008;478:181–6. doi:10.1016/j.msea.2007.05.110.

[19] Minnebo P, Nilsson K-F, Blagoeva D. Tensile, Compression and Fracture Properties of Thick-Walled Ductile Cast Iron Components. J Mater Eng Perform 2007;16:35–45. doi:10.1007/s11665-006-9005-z.

[20] Ceschini L, Morri A, Morri A. Effects of Casting Size on Microstructure and Mechanical Properties of Spheroidal and Compacted Graphite Cast Irons: Experimental Results and Comparison with International Standards. J Mater Eng Perform 2017;26:2583–92. doi:10.1007/s11665-017-2714-7.

[21] Shinde VD, Ravi B, Narasimhan K. Solidification behaviour and mechanical properties of ductile iron castings with varying thickness. Int J Cast Met Res 2012;25:364–73. doi:10.1179/1743133612Y.0000000024.

[22] Bočkus S, Venckunas A, Žaldarys G. Relation between section thickness, microstructure and mechanical properties of ductile iron castings. Medziagotyra 2008;14:115–8.

[23] Ecob CM. A review of common metallurgical defects in ductile cast iron 2005.

[24] Kallbom R, Hamberg K, Wessén M, Bjorkegren LE. On the solidification sequence of ductile iron castings containing chunky graphite. Mater Sci Eng A 2005;414:346–51.

[25] Zhou, Jiyang. Colour metallography of cast iron. vol. 7. 2009.

[26] Regordosa A, Llorca-Isern N. Microscopic Characterization of Different Shrinkage Defects in Ductile Irons and their Relation with Composition and Inoculation Process. Int J Met 2017;11:778–89. doi:10.1007/s40962-016-0120-9.

[27] Ferro P, Fabrizi A, Cervo R, Carollo C. Effect of inoculant containing rare earth metals and bismuth on microstructure and mechanical properties of heavy-section near-eutectic ductile iron castings. J Mater Process Technol 2013;213:1601–8.

[28] Jiyang, Z., Schmitz, W., Engler S. Formation of austenite shell around spheroidal graphite and its effect on deterioration of graphite. Acta Metall Sin 1989;2:261–5.

[29] Itofuji, H., Uchikawa H. Formation mechanism of chunky graphite in heavy-section ductile cast irons. Trans Am Foundrymen's Soc 1990;98:429–46.

[30] Karsay SI. Ductile Iron: Production: the State of the Art 1976; Quebec Iron and Titanium Corporation.

[31] Zhang Z, Flower HM, Niu Y. Classification of degenerate graphite and its formation processes in heavy section ductile iron. Mater Sci Technol 1989;5:657–64. doi:10.1179/mst.1989.5.7.657.

[32] de la Torre U, Lacaze J, Sertucha J. Chunky graphite formation in ductile cast irons: effect of silicon, carbon and rare earths. Int J Mater Res 2016;107:1041–50. doi:10.3139/146.111434.

[33] Wessén, M., Svensson, I.L., Aagaard R. Influence of antimony on microstructure and mechanical properties in thick-walled ductile iron castings. Int J Cast Met Res 2003;16:119–24.

[34] Loper, C.R., Heine RW, Reesman RW, Shah BH. Thermal Analysis of Ductile Iron. Trans Am Foundrymen's Soc 1967;75:541–7.

[35] Sertucha J, Suárez R, Asenjo I, Larrañaga P, Lacaze J, Ferrer I, et al. Thermal Analysis of the Formation of Chunky Graphite during Solidification of Heavy-section Spheroidal Graphite Iron Parts. ISIJ Int 2009;49:220–8. doi:10.2355/isijinternational.49.220.

[36] Larrañaga P, Asenjo I, Sertucha J, Suarez R, Ferrer I, Lacaze J. Effect of antimony and cerium on the formation of chunky graphite during solidification of heavy-section castings of near-eutectic spheroidal graphite irons. Metall Mater Trans A Phys Metall Mater Sci 2009;40:654–61. doi:10.1007/s11661-008-9731-y.

[37] Čanžar P, Tonković Z, Kodvanj J. Microstructure influence on fatigue behaviour of nodular cast iron. Mater Sci Eng A 2012;556:88–99. doi:10.1016/j.msea.2012.06.062.

[38] Cavallini M, Di Bartolomeo O, Iacoviello F. Fatigue crack propagation damaging micromechanisms in ductile cast irons. Eng Fract Mech 2008;75:694–704. doi:10.1016/j.engfracmech.2007.02.002.

[39] Di Cocco V, Iacoviello F, Cavallini M. Damaging micromechanisms characterization of a ferritic ductile cast iron. Eng Fract Mech 2010;77:2016–23. doi:10.1016/j.engfracmech.2010.03.037.

[40] Iacoviello F, Cocco V Di. Ductile Cast irons: microstructure influence on fatigue crack propagation resistance. Frat Ed Integrità Strutt 2010;13:3–16. doi:10.3221/IGF-ESIS.13.01.

[41] Di Cocco V, Iacoviello F, Rossi A, Iacoviello D. Macro and microscopical approach to the damaging micromechanisms analysis in a ferritic ductile cast iron. Theor Appl Fract Mech 2014;69:26–33.

[42] Di Cocco V, Iacoviello F, Rossi A, Cavallini M, Natali S. Graphite nodules and fatigue crack propagation micromechanisms in a ferritic ductile cast iron. Fatigue Fract Eng Mater Struct 2013;36:893–902. doi:10.1111/ffe.12056.

[43] Iacoviello F, Cocco V Di. Degenerated graphite nodules influence on fatigue crack paths in a ferritic ductile cast iron. Frat Ed Integrita Strutt 2015;9:406–14. doi:10.3221/IGF-ESIS.34.45.

[44] Sujakhu S, Castagne S, Sakaguchi M, Kasvayee KA, Ghassemali E, Jarfors AEW, et al. On the fatigue damage micromechanisms in Si-solution–strengthened spheroidal graphite cast iron. Fatigue Fract Eng Mater Struct 2018;41:1–17. doi:10.1111/ffe.12723.

[45] Murakami Y. Metal fatigue: effects of small defects and nonmetallic inclusions. 2002.

[46] Ostensoon B. Influence of Microshrinkage Cavities on the Endurance Limit of Nodular Cast Iron. J Iron Steel Inst 1972;Sept:628–31.

[47] Nadot, Mendez, Ranganathan, Beranger. Fatigue life assessment of nodular cast iron containing casting defects. Fatigue Fract Eng Mater Struct 1999;22:289–300. doi:10.1046/j.1460-2695.1999.00162.x.

[48] Nadot Y. Influence of casting defects on the fatigue limit of nodular cast iron. Int J Fatigue 2004;26:311–9. doi:10.1016/S0142-1123(03)00141-5.

[49] Collini L, Pirondi A, Bianchi R, Cova M, Milella PP. Influence of casting defects on fatigue crack initiation and fatigue limit of ductile cast iron. Procedia Eng 2011.

[50] Collini L, Pirondi A. Fatigue crack growth analysis in porous ductile cast iron microstructure. Int J Fatigue 2014;62:258–65.

[51] Kainzinger P, Guster C, Severing M, Wolf A. Influence of micro-shrinkage on the fatigue behavior of ductile iron. 13 Int. Conf. Fract., 2013, p. 1–9.

[52] Kainzinger P, Wohlfahrt M, Grün F. Einfluss der lokalen Gefügeausbildung auf die Schwingfestigkeit von Gusseisen mit Kugelgraphit. BHM Berg- Und Hüttenmännische Monatshefte 2015;160:2–8. doi:10.1007/s00501-014-0328-z.

[53] Shirani M, Härkegård G. A review on fatigue design of heavy section EN-GJS-400- 18-LT ductile iron wind turbine castings. Energy Equip Syst 2014;2:5–24.

[54] Shirani M, Härkegård G. Damage tolerant design of cast components based on defects detected by 3D X-ray computed tomography. Int J Fatigue 2012;41:188–98. doi:10.1016/j.ijfatigue.2011.09.011.

[55] Shirani M, Härkegård G. Fatigue life distribution and size effect in ductile cast iron for wind turbine components. Eng Fail Anal 2011;18:12–24. doi:10.1016/j.engfailanal.2010.07.001.

[56] Shirani M, Härkegård G. Large scale axial fatigue testing of ductile cast iron for heavy section wind turbine components. Eng Fail Anal 2011;18:1496–510.

[57] Bleicher C, Wagener R, Kaufmann H, Melz T. Fatigue Assessment of Nodular Cast Iron with Material Imperfections. SAE Int J Engines 2017;10:2017-01–0344. doi:10.4271/2017-01-0344.

[58] Luo J, Harding RA, Bowen P. Evaluation of the fatigue behavior of ductile irons with various matrix microstructures. Metall Mater Trans A Phys Metall Mater Sci 2002;33:3719–30. doi:10.1007/s11661-002-0244-9.

[59] Foglio E, Gelfi M, Pola A, Goffelli S, Lusuardi D. Fatigue Characterization and Optimization of the Production Process of Heavy Section Ductile Iron Castings. Int J Met 2017;11:33–43. doi:10.1007/s40962-016-0112-9.

[60] Endo M, Iseda K. Prediction of the Fatigue Strength of Nodular Cast Irons under combined loadings. Int J Mod Phys B 2006;20:3817–23.

[61] Endo M. Effects of graphite shape, size and distribution on the fatigue strength of spheroidal graphite cast irons. J Soc Mater Sci Japan 1989;38:1139–44. doi:10.2472/jsms.38.1139.

[62] Endo M, Wang X-B. Effects of graphite and artificial small defect on the fatigue strength of current ductile cast irons. J Soc Mater Sci Japan 1994;43:1245–50. doi:10.2472/jsms.43.1245.

[63] Endo M. Fatigue Strength Prediction of Ductile Irons Subjected To Combined Loading. ECF13, San Sebastian, vol. 43, 2000.

[64] Endo M, Yanase K. Effects of small defects, matrix structures and loading conditions on the fatigue strength of ductile cast irons. Theor Appl Fract Mech 2014;69:34–43. doi:10.1016/j.tafmec.2013.12.005.

[65] Mourujärvi A, Widell K, Saukkonen T, Hänninen H. Influence of chunky graphite on mechanical and fatigue properties of heavy-section cast iron. Fatigue Fract Eng Mater Struct 2009;32:379–90. doi:10.1111/j.1460-2695.2009.01337.x.

[66] Ferro P, Lazzarin P, Berto F. Fatigue properties of ductile cast iron containing chunky graphite. Mater Sci Eng A 2012;554:122–8.

[67] Foglio E, Lusuardi D, Pola A, La Vecchia GM, Gelfi M. Fatigue design of heavy section ductile irons: Influence of chunky graphite. Mater Des 2016;111:353–61. doi:10.1016/j.matdes.2016.09.002.

[68] Nakae H, Fukami M, Kitazawa T, Zou Y. Influence of Si , Ce , Sb and Sn on chunky graphite formation. China Foundry 2010;8:96–100.

2. *Experimental Procedures*

Highlights

In this section, the experimental procedures conducted during the doctorate are described, following which an in-depth microstructural and mechanical characterization of different types of spheroidal cast iron characterized by different conditions of cooling and solidification was carried out. During the experimental campaigns, microstructural analyses were performed using an optical microscope and image analysis software on polished and etched samples. In addition, tensile and fatigue tests were performed on specimens obtained from the areas of interest within the castings. The fracture surfaces were then analysed by SEM to identify the causes of fracture.

2.1 Castings geometries

All the experiments have been carried out in VDP Fonderia S.p.A. production plant, consuming materials and products that are used daily in the foundry production practice.
In order to investigate the effect of different solidification times on the properties of the alloys, specific casting geometries have been used.

In particular, in order to represent some solidification conditions of real casting components, a geometry was designed, characterized by a 300x250x300 mm^3 parallelepiped to which a feeder with exothermic sleeve has been added on the top surface. The furan bonded sand mould contained four blocks with common gating system. (see Figure 2.1).

Another heavy section casting was considered, consisting of a cylinder ø300 mm and 520 mm in height. In order to reduce casting defects, the ingate system was placed at the bottom of the casting (see Figure 2.2).

Finally, in the automatic green sand moulding and pouring line, three different cast samples have been considered having geometries according to UNI EN 1563:2012 standard. In particular, round bar-shaped and Y-shaped samples have been produced, with thicknesses varying from 25 to 75 mm, as shown in Figure 2.3.

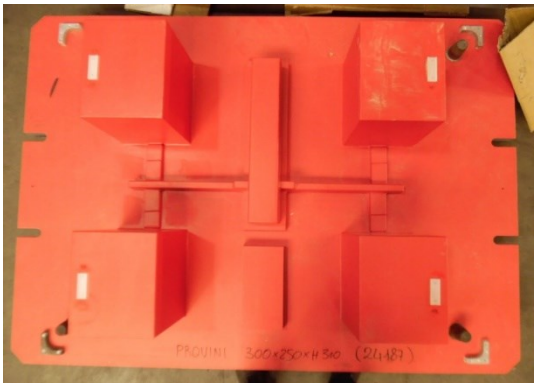

Figure 2.1. Geometry of the pattern of 300x250x300 mm^3 casting blocks.

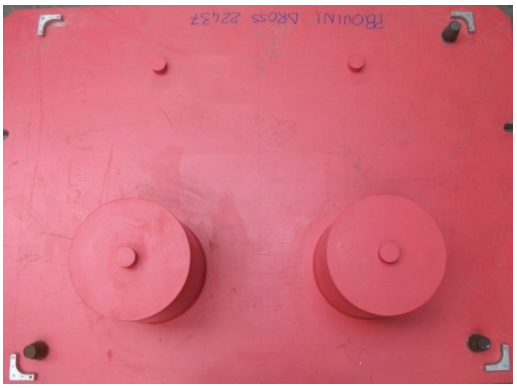

Figure 2.2. Geometry of the pattern of the cylinder ø300 mm, h 520 mm.

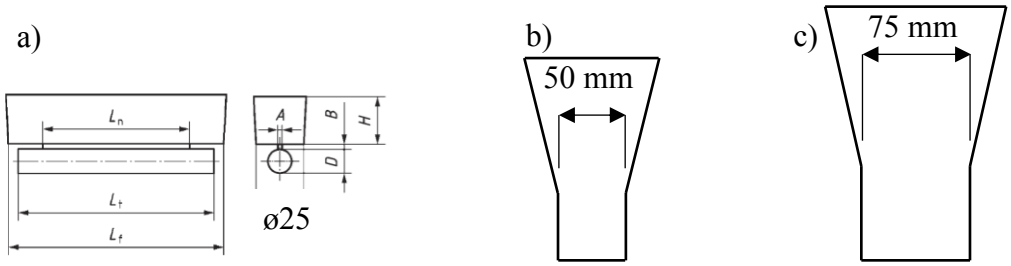

Figure 2.3. Geometry of cast samples produced in the green sand pouring line. Round bar-shaped sample (a), Y-shaped type III sample (b) and Y-shaped type IV sample (c).

2.2 Thermal analysis

Thermal analysis has been performed by acquiring the temperature/time curve using a standard cup, containing a thermocouple, filled with liquid metal. Moreover, the cooling rate, defined as the first time derivative (dT/dt) of the cooling curve has been calculated. By analysing the curves, it is possible to identify the phase transformations during solidification and the solid-state transformation, the most important characteristic temperature of the alloy and to control the quality of the material.

After the spheroidizing and inoculation process, and just before pouring the iron into the moulds, a metal sample was taken from the ladle and analysed by optical emission spectrometry to determine the chemical composition. At the same time, a standard cup for the thermal analysis, containing the same weight percentage of inoculant of the real casting, was filled.

Moreover, in addition to standard thermal analysis, and in order to control the real thermal history of the metal, cooling curve has been also analysed directly on the casting by using an optimized temperature recording apparatus by means of a K-type thermocouple (chromel (Ni-Cr)(+)/alumel(Ni-Al)(-)) connected with a digital data logger TC-08.

With the purpose to protect it from the melted alloy, the thermocouple was inserted in a ceramic pipe (Al_2O_3) and locked within, through a subsequent pipe filling with an alumina-based ceramic solution, then dried.

The thermocouple was positioned inside the cavity during the mould forming process in order record the temperature in the centre of the casting.

2.3 Mechanical characterization

2.3.1 Tensile test

Specimens for the mechanical tests have been taken directly from the castings, from zones characterized by specific solidification times, identify by using numerical simulations (see next chapters).

Tensile tests have been conducted at room temperature by using an INSTRON 5500R tensile test machine under strain rate control, according to ISO 6892-1:2016 standard. Strain has been measured by means of an axial extensometer mounted on the samples. Cylindrical specimens, with gauge diameter of 14 mm and parallel length equal to 84 mm have been used, according to UNI EN 1563:2012. Ultimate tensile strength, yield stress at 0.2% of plastic extension and elongation at failure have been recorded.

2.3.2 Brinell hardness test

Brinell hardness tests have been carried out by using a Wolpert hardness tester equipped with a indenter of diameter ø 5 mm and applying a load of 7.355 kN, in order to obtain a force-diameter ratio $0.102 \cdot F/D^2$ equal to 30 N/mm^2 according to ISO 6506-1:2005 standard. The diameter of each indentation has been measured in two directions perpendicular to each other, and the arithmetic mean of the two readings has been used for the calculation of Brinell hardness.

2.3.3 Charpy V-notch impact test

Charpy V-notch impact tests have been carried out according to ISO 148-1: 2009 by using a Galdabini 300J Impact Tester. V-notched samples have been machined according to the standard.

Test have been carried out at room temperature and at -20°C.

2.3.4 Fatigue test

Uniaxial tension fatigue tests have been carried out at room temperature by using different two testing equipment under nominal load ratios equal to R = 0 and R = -1. A universal MTS machine (250 kN) running under load control at a frequency of about 15 Hz and a resonant testing machine Rumul Testronic 150 kN running with a sinusoidal pulsating load at a frequency of approximately 120 Hz (Figure 2.4). The resonant load frequency depends, among other variables, on the stiffness of the tested specimen, which is influenced by specimen geometry and elastic modulus of the material. In case it is possible to examine, in a rather precise way, the cracks initiation and propagation stages. In fact, crack growth will reduce the specimens cross-section area, and thus its stiffness and resonance frequency will be reduced. Fatigue specimens geometries are shown in Figure 2.5.

In one case, also rotating bending fatigue tests have been carried out, on 6.5 mm diameter specimens and by applying cycling loadings at a frequency of 100 Hz, using the staircase method and applied stress step of 10 MPa.

In both cases, fatigue data have been statistically analysed according to ISO 12107:2012 standard.

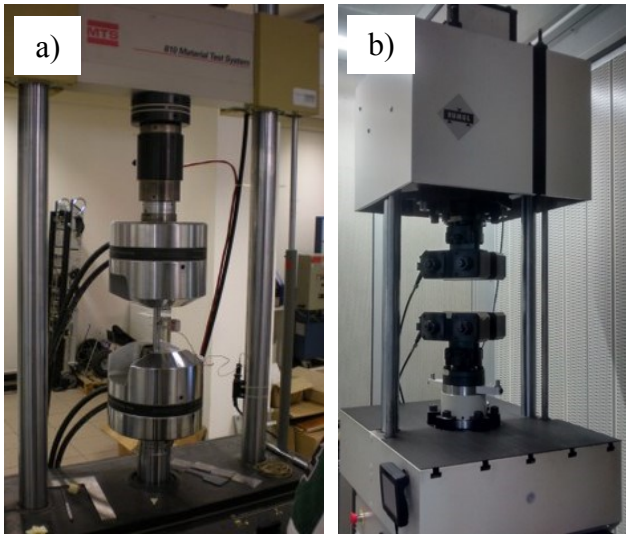

Figure 2.4. Fatigue test machines. MTS 250 kN (a) and Rumul Testronic 150 kN (b).

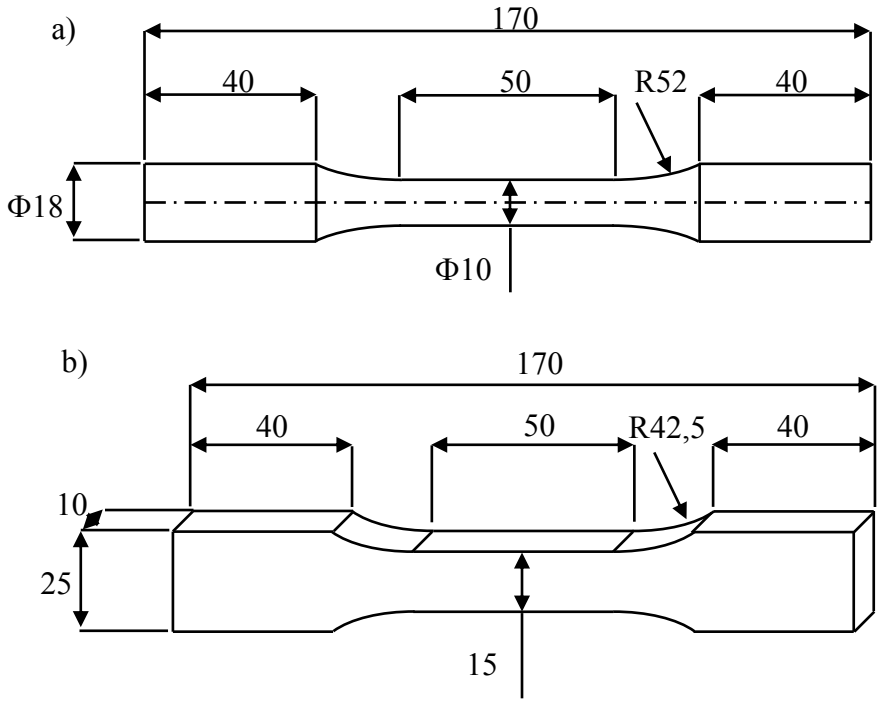

Figure 2.5. Fatigue specimens geometries. Dimensions in mm.

2.4 Microstructural characterization

2.4.1 Metallographic analysis

Microstructural investigations have been performed on samples taken near the fracture surfaces of tensile and fatigue broken specimens. The procedure is described below.

Samples were incorporated in resin through hot compression mounting (Figure 2.6a), in order to improve the handling and the subsequent activities. Samples have been then polished on an automated polishing machine and successively finer abrasives (180, 240, 1000 mesh SiC abrasive papers and 6 μm, 3 μm diamond paste) until a mirror-finishing surface was obtained (Figure 2.6b).

In order to reveal the matrix structure, samples have been etched with Nital 5%.

Microstructures has been investigated by mean of an inverted reflected light microscope, with magnification from 50x to 1000x, interfaced with an image analysis software (Figure 2.6c). Among other applications, the software permits to

evaluate most important microstructural parameters according to ISO or ASTM standards.

Once the appropriate standard is chosen, it is possible to calculate, for example, the nodule count, shape and dimensions of graphite particles and the type of matrix (percentage of ferrite and/or pearlite).

Figure 2.6. Images of metallographic analysis apparatus. Metallographic compression mounting press (a), automated polishing machine (b), inverted reflected light microscope interfaced with image analysis software (c)

2.4.2 Fractographic analysis

Fracture surfaces of fatigue broken specimens have been investigated by using a a field emission gun–environmental scanning electron microscope (FEG–ESEM) (FEI, Quanta 250 FEG) in the metallurgy laboratory of the Department of Management and Engineering of University of Padova.

Prior to put the samples inside the microscope chamber, they have been firstly immersed in denatured ethyl alcohol and then dried, in order to clean up the fracture surfaces.

The aims of the analysis were to identify the fatigue crack initiation cause and to characterize the crack propagation and the fracture mechanisms that happened during the final failure stage.

2.4.3 Statistical analysis of extreme values

Particular attention was paid to the evaluation of the effect of microstructural defects that acted as nucleation points of fatigue cracks.

It is well recognized that the fatigue strength is controlled by the largest defect that is present in a material subjected to fatigue loading conditions, rather than the average dimension of inhomogeneities.

For this reason, the dimensions of each initiating defect detected on the fracture surface have been measured by means of an image analysis software, and collected data have been processed through the statistical analysis of extreme values.

In order to evaluate the maximum occurring defect, largest extreme value distribution (LEVD) has been used, the parameters of which have been estimated by adopting the Maximum Likelihood method.

The LEVD follows a two-parameter Gumbel distribution and the probability density function is given by the equation:

$$f(x) = \frac{1}{\delta}\left[\exp\left(-\frac{x-\lambda}{\delta}\right)\right] \cdot \exp\left[-\exp\left(-\frac{x-\lambda}{\delta}\right)\right] \qquad (1)$$

and cumulative probability function:

$$F(x) = \exp\left[-\exp\left(-\frac{x-\lambda}{\delta}\right)\right] \qquad (2)$$

where λ and δ represent the location and scale parameter, respectively, that have to be estimated.

The dimension of the maximum defect with T return period is expressed as:

$$x(T) = \lambda - \delta \cdot \ln\left[-\ln\frac{T-1}{T}\right] \qquad (3)$$

The estimation of the parameters has been performed by maximizing the log of the distribution function, which is for the data set:

$$L = \sum_i \ln[f(x_i, \delta, \lambda)] \qquad (4)$$

where $f(x_i, \delta, \lambda)$ represents the probability density function of each *i*-defect.

Once the optimized parameters (δ_{ML} and λ_{ML}) have been obtained, the approximate confidence band can be calculated according to the equation:

$$x(T) \pm K_\gamma \cdot \delta_{ML} \cdot \sqrt{\frac{1.109 + 0.608 \cdot y^2 + 0.514 \cdot y}{N}} \qquad (5)$$

where K_γ=1.96 for a probability of 95% and y the reduced variate of the LEVD.

2.5 Scheme of the experimental activities

Experimental activities have been conducted following a procedure, as shown in the scheme of Figure 2.7.

The first part has been focused on the characterization of traditional cast irons affected by long solidification times. First of all, traditional ferritic ductile iron has been studied; subsequently, cast irons with pearlitic matrix have been considered.

In the second part new generation solution strengthened ferritic ductile irons have been considered. In this case, due to limited available data in literature, the effects of both long and short solidification times have been analysed.

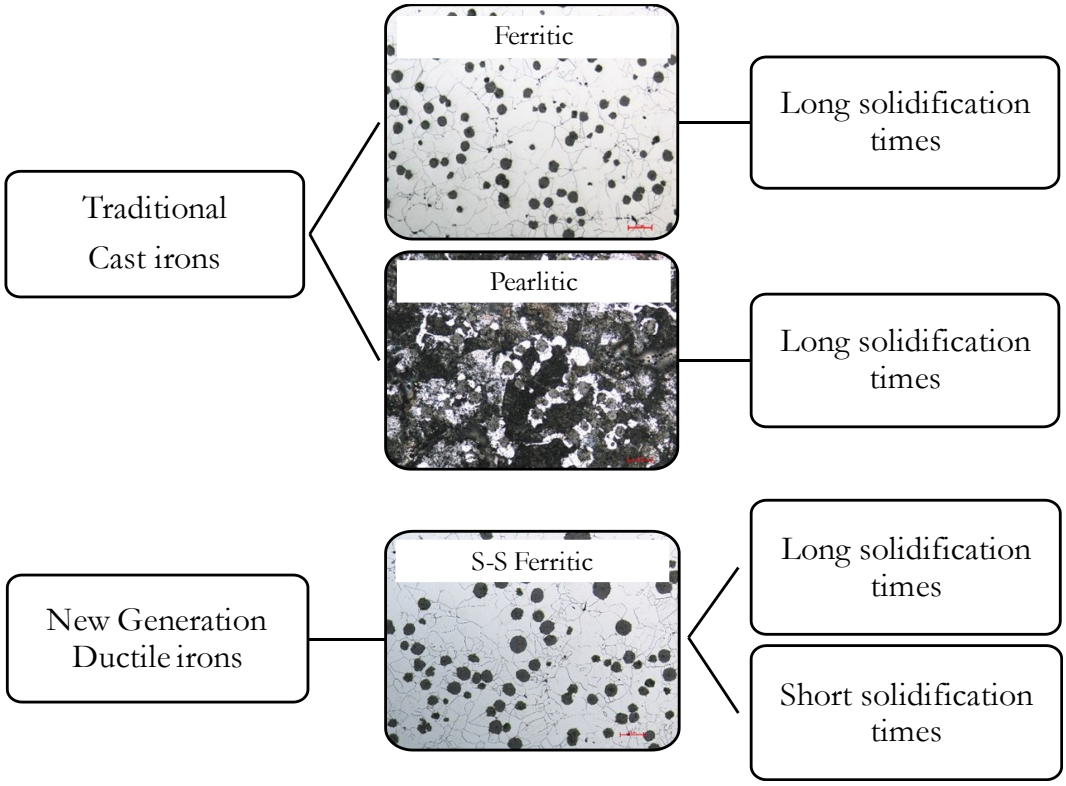

Figure 2.7 Scheme of the experimental activities.

3. *Traditional Ferritic ductile iron (GJS 400-18 LT)*

Highlights

This chapter summarizes data from the microstructural, mechanical and fatigue characterization of a traditional ferritic ductile cast iron, GJS 400-18 LT according to UNI EN 1563:2012 standard, and characterized by solidification time longer than 2.5 hours.

The aim of this activity is to improve the knowledge of the mechanical behaviour of this alloy by means of a new set of experimental data, in a specific cooling condition.

The castings used in this work were four blocks 300x250x300 mm^3 in dimensions with feeders on the top surfaces. During the pouring procedures, a standard cup for thermal analysis has been filled. Moreover, a system has been optimized in order to record the temperature during the cooling and solidification of the castings. Tensile, Brinell hardness, Charpy impact test and fatigue tests have been conducted using specimens taken from the most critical zones within the blocks. Metallographic analysis have been performed in order to evaluate the most important microstructural properties of the alloy. Fractography has been carried out in order to identify crack initiation points and fracture mechanisms. Finally, statistical analysis of extreme values has been used with the aim of estimate the maximum dimensions of defects that can be present inside the castings.

3.1 Material

The material under investigation was an EN GJS 400-18 LT ductile cast iron, which final chemical composition is summarized in Table 3.1. In particular, the "LT" in the material designation stands for low temperature applications. For this reason, the amount of Silicon is kept low, with an amount of about 2 wt%. The carbon content is chosen in order to maintain a near-eutectic composition. It is also important to note that, with the aim of counteracting the formation of degenerated chunky graphite in the thermal centre of the castings, small amount of Antimony was added to the alloy.

Table 3.1. Final chemical composition of GJS 400-18 LT ductile iron. (wt%).

C	Si	S	P	Mn	Cu	Sb	Mg	Ceq
3.79	2.06	0.007	0.030	0.215	0.07	0.0024	0.064	4.49

3.2 Thermal analysis

Using the thermal analysis technique, it is possible to understand the way of solidification and cooling and to check the quality of the alloy, but it does not provide a perfect indication of what happens inside a casting due to different cooling conditions. Moreover, the solid-state transformation can be studied using this technique. The cooling curve obtained from the standard cup and the calculated first time derivative are shown in Figure 3.1, where it can be observed that the alloy solidify in an eutectic manner, with eutectic temperature of about 1143 °C. In can also be observed that, due to the low amount of Silicon content and the high cooling rate, during the solid-state transformation, pearlite was formed. In the case of castings with greater section thickness and lower cooling rate, a fully ferritic matrix can be achieved with this chemical composition.

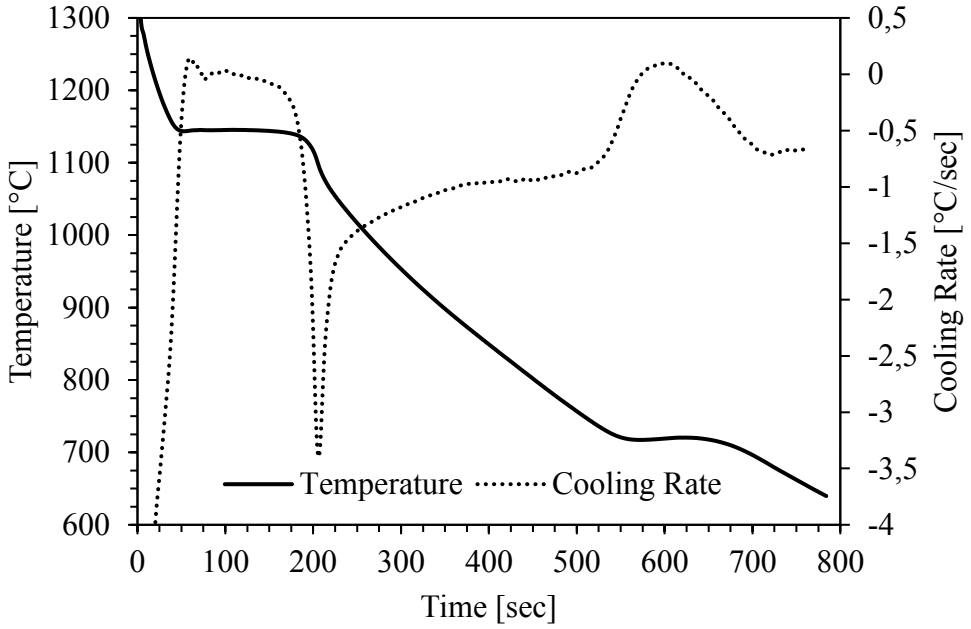

Figure 3.1. Cooling curve (solid line) and its first derivative (dotted line) of a traditional ferritic ductile iron (GJS 400-18 LT) from standard thermal cup.

In order to control the real thermal history of the alloy, thermal analysis has been also performed directly on one of the castings by using an optimized temperature recording apparatus. In particular, a type k thermocouple has been inserted in an alumina tube and connected with a digital data logger TC-08. The thermocouple was positioned inside the cavity during the mould forming process in order record the temperature in the centre of the block. For this purpose, it was necessary to remove the feeder from the top surface. In Figure 3.2, the position of the thermocouple inside the block is shown, while in Figure 3.3, an image of the recording apparatus, just before the pouring process, is shown.

Data has been analysed in order to obtain a temperature profile and to calculate the cooling rate, and it was found that the solidification still happens in a near-eutectic conditions.

Comparing the experimental results with the temperature profile found in the standard thermal cup, some differences can be noted. First of all the solidification time, which has been measured to be longer than two hours, and the cooling rate. It

should also be noted that, in order to reach temperatures below the eutectoid, the time required is greater than 12 hours.

Variations are visible also in the transformation temperatures. In particular, due to a higher heat removal in the standard cups, the eutectic undercooling is much higher than that found in the centre of the casting, where a eutectic temperature of about 1155°C was found. The same behaviour has been observed in the solid-state transformation temperature, which was measured to be about 760°C.

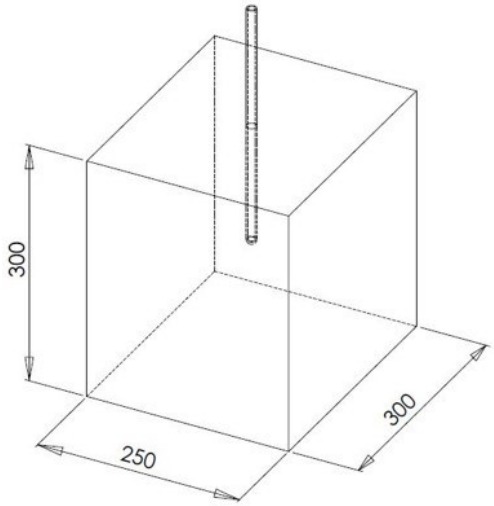

Figure 3.2. Scheme of the position of thermocouple inside the casting.

Figure 3.3. Image of the recording apparatus just before pouring the casting.

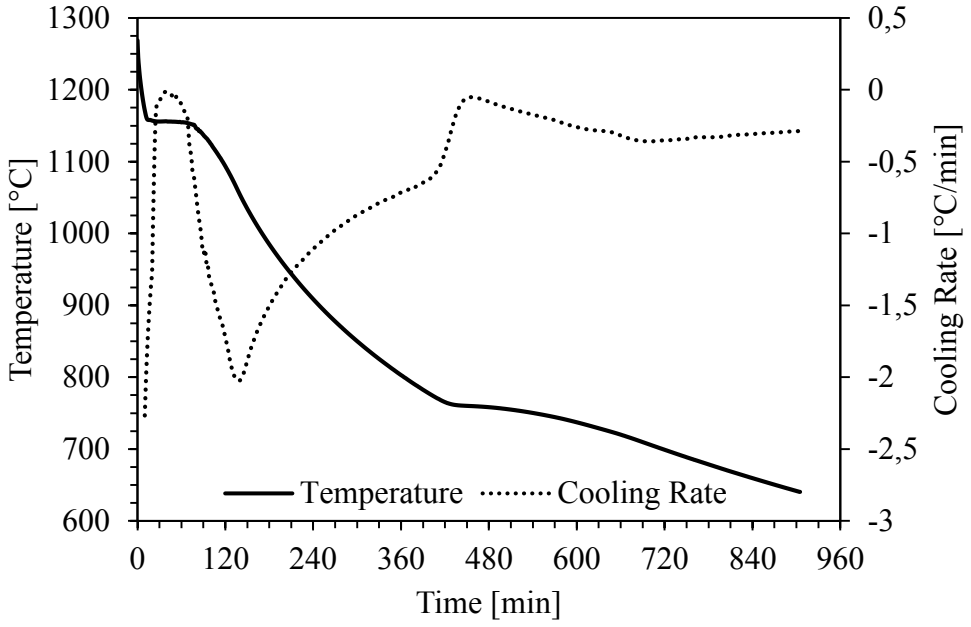

Figure 3.4. Cooling curve (solid line) and its first derivative (dotted line) of a traditional ferritic ductile iron (GJS 400-18 LT) taken from the centre of a 300x250x300 mm^3 casting.

3.3 Tensile, Brinell hardness and Charpy impact tests

Tensile tests have been performed using specimens cut from the inside of the castings, from areas characterized by solidification times of more than 2.5 hours, as shown in Figure 3.5.

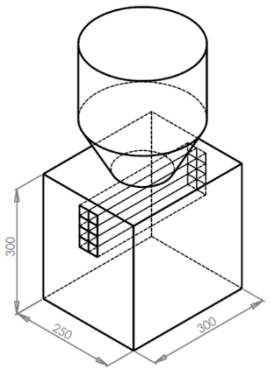

Figure 3.5. Schematic showing casting positions where specimens were taken.

Eight cylindrical smooth specimens with net diameter of 14 mm have been used for the tensile tests. The results are summarised in Table 3.2 in terms of mean value and standard deviation, together with the data obtained from standard Y shaped type IV cast sample, according to UNI EN 1563:2012.

It is important to note that mechanical properties of the casting, characterized by long solidification time, were found to be not much lower than typical values obtained from the standard samples.

Moreover, it is worth noticing that standard deviations are limited, deducting that mechanical properties are homogenous in the considered zones.

Brinell hardness tests have been performed according to UNI EN ISO 6506:2006 using a test machine with an indenter diameter of 5 mm and force-diameter ratio $0.102 \cdot F/D^2$ equal to 30 N/mm^2. Tests have been made on 15 samples taken from different areas in the casting varying the distance from the top surface. Also in this case, homogeneous Brinell hardness distribution has been found in the whole casting, with a mean value of 150 ± 4.6 HB.

In the case of traditional ferritic ductile iron GJS 400-18 LT Charpy impact test is quite often required. For this reason, V-notched specimens, taken from the castings, have been tested at room temperature (23°C) and at -20°C, according to ISO 148-1. In Table 3.3, the values of impact energy and specific energy are shown for the

two temperature investigated, together with standard deviations. It can be observed that the values of impact energy are higher than the typical minimum value of 10 J, often used for this type of material under normal solidification conditions.

Table 3.2. Tensile test results, mean value and standard deviations.

	σ_{UTS}[MPa]	$\sigma_{y\ 0.2\%}$ [MPa]	ε_R %
Y shaped type IV cast sample	400	262	23.4
specimens from casting	383 ± 7.4	250 ± 4.2	19.9 ± 2.3

Table 3.3. Charpy V-notch impact test results (striker KV_2).

Temperature	Energy [J]	Specific energy [J cm^{-2}]
Room Temperature	16.1 ± 2.1	20.1 ± 2.6
-20°C	13.5 ± 2.1	16.8 ± 2.6

3.4 Fatigue test

The results of the fatigue tests conducted with nominal load ratio R = 0 have been statistically elaborated assuming a log-normal distribution and plotted in a double log scale. The stress amplitude is referred to the net area of the specimens. Figure 3.6 shows the experimental fatigue data, the mean Wöhler curve at survival probability of 50%, and the Haibach scatter band referred to 10% and 90% of probabilities of survival, for a confidence level equal to 95%. The run out specimens, over two million cycles, and the samples failed before $1 \cdot 10^4$ cycles were not included in the statistical analysis. A vertical line indicates the values corresponding to two million cycles. For the sake of completeness, the values of the inverse slope k and the scatter index T_σ, which provides the width of the scatter band between the curves with survival probability of 10% and 90%, are also shown. It has been found that the fatigue stress amplitude at 2 million cycles and survival probability of 50% is equal to 100 MPa, with a quite narrow scatter index equal to 1.20.

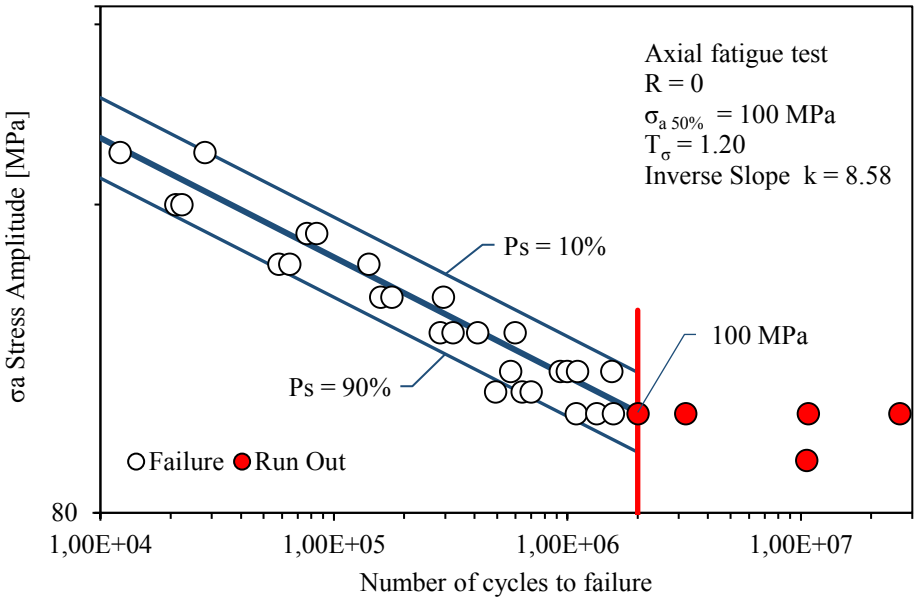

Figure 3.6. Fatigue life of traditional ferritic ductile iron (GJS 400-18 LT) characterized by solidification time of more than 2.5 hours under axial fatigue loading at nominal load ratio R = 0.

In order to evaluate the influence of load ratio, some specimens have been tested under alternate tensile pulsating loading conditions, R = -1. Fatigue data and calculated fatigue curves are shown in Figure 3.7. In this case, the fatigue strength has been found to be 140 MPa at 2 million cycles.

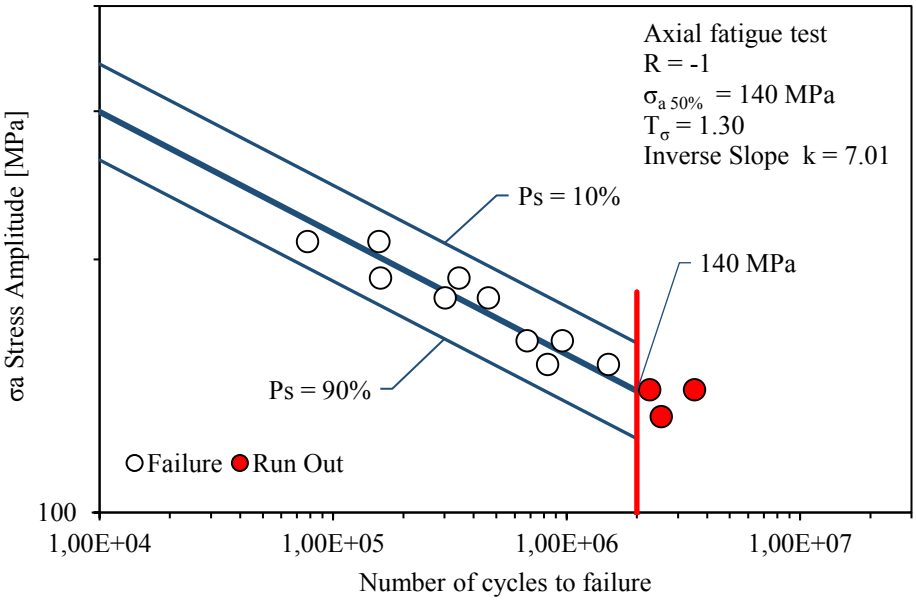

Figure 3.7. Fatigue life of traditional ferritic ductile iron (GJS 400-18 LT) characterized by solidification time of more than 2.5 hours under axial fatigue loading at nominal load ratio R = -1.

Finally, in order to evaluate also the fatigue resistance under different loading conditions, some specimens have been tested using a rotating bending machine at nominal load ratio equal to -1. Tests were carried out at room temperature with a frequency of 100 Hz by using cylindrical specimens with diameter of 6.5 mm. The tests have been carried out, by applying stress step of 10 MPa and were stopped at sample failure or after $5 \cdot 10^6$ cycles. Data have been statistical analysed by means of two statistical elaborations. Data in the finite fatigue life have been elaborated assuming a log-normal distribution as described previously, the results of which are shown in Figure 3.8, where it can be observed that the fatigue strength at 2 million cycles and 50% survival probability is equal to 175 MPa.

Moreover, data obtained from the stair-case method have been analysed according to the procedure reported in ISO 12107:2012 standard, from which the fatigue stress amplitude and the standard deviation were found to be 175 MPa and 3.4 MPa respectively.

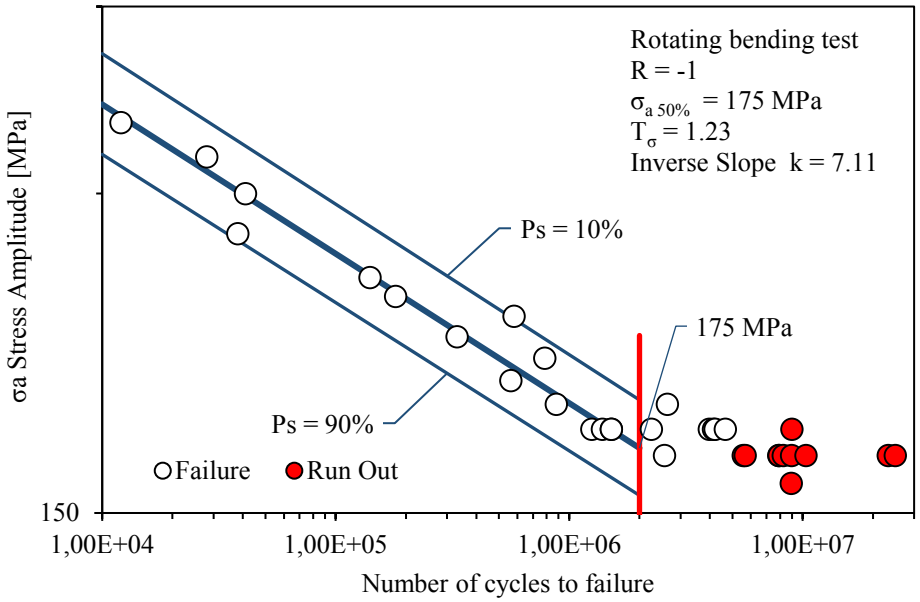

Figure 3.8. Fatigue life of traditional ferritic ductile iron (GJS 400-18 LT) characterized by solidification time of more than 2.5 hours under rotating bending loading conditions.

3.5 Microstructure and fractography

To evaluate microstructural parameters, metallographic analyses have been carried out in a section of broken and unbroken specimens, using an optical microscope connected to an image analysis software. The software allows to evaluate nodule count, nodule size, and nodularity according to ASTM E2567-11. A number of images have been taken, in order to cover an observation area of more than 150 mm^2. With the aim to identify matrix structure, samples have been etched with Nital 5%. A summary of the microstructural properties is presented in Table 3.4. Examples of micrographs are shown in Figure 3.9.

It is known that, increasing solidification times, the microstructure becomes coarser. In fact, it can be noted that the number of spheroidal graphite nodules is low and their mean dimension and standard deviation are quite large. This emphasises the fact that the microstructure is characterized by graphite particles of various sizes, some of which of big dimensions and/or deviating from the ideal spherical shape. This is not surprising considering that specimens have been taken from the zone characterized by the longest solidification time in the casting.

Considering etched samples, it was found that the ferritic matrix is predominant in the microstructure, but areas of pearlite were found, due to segregation of undesired carbide promoting or pearlitizing elements present in the alloy (Figure 3.9 a). Some microstructural defects have been also observed, such as microshrinkage porosities, degenerated graphite particles or carbides, see Figure 3.9 b.

Finally, it is confirmed that the treatment with some ppm of Antimony is effective in counteracting the formation of chunky graphite in the thermal centre of heavy section castings, characterized by long solidification times.

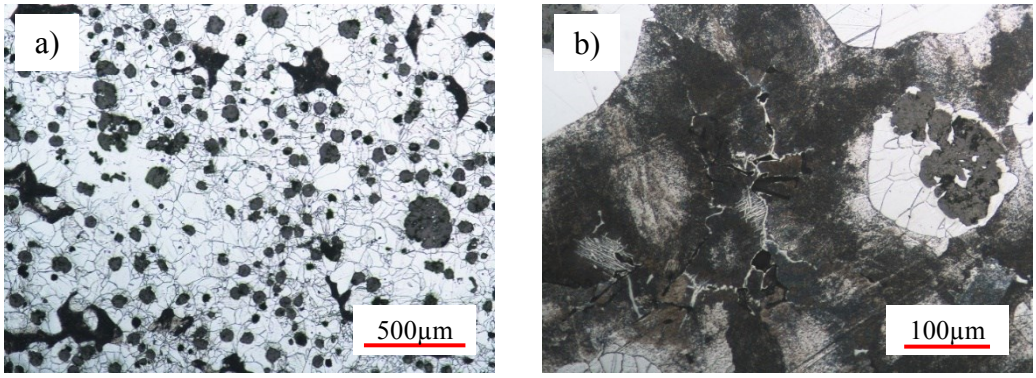

Figure 3.9. Examples of micrographs of specimens taken from the casting, showing an overview of the microstructure (a) and a particular of casting defects (b).

Table 3.4. Microstructural properties of traditional ferritic ductile iron GJS 400-18 LT inside the casting.

Nodularity [%]	Nodule Count [mm^{-2}]	Mean Nodule Diameter [µm]	Ferrite content [%]
86	31	60 ± 25	95

The fracture surfaces of some of the fatigue broken specimens have been analysed by means of SEM. It has been observed that cracks initiated at microstructural defects, which have been found to be microshrinkage cavities, even of large sizes, close to specimen surface, or degenerated graphite particles. For each analysed sample, the projected surface of crack initiators have been measured, in order to obtain the √area parameter, as shown in Figure 3.10. Using the statistical analysis of extreme values, the $\sqrt{area}_{max}$ was estimated, by considering the dimension of the defect corresponding to the upper bound of the 95% confidence interval of the √area distribution. In Figure 3.11, it is shown the defects distribution of the microshrinkage and degenerated graphite particles that acted as crack initiators. It can be observed that, notwithstanding degenerated graphite particles are at the origin of fatigue cracks in some specimens, the larger defects are microshrinkage porosities. Finally, it has been observed that crack propagated in the material along the interface between the matrix and the spheroidal graphite particles (Figure 3.12 a), while the static final failure happens in a ductile manner, with dimple fracture and microvoids coalescence, as can be seen in Figure 3.12 b.

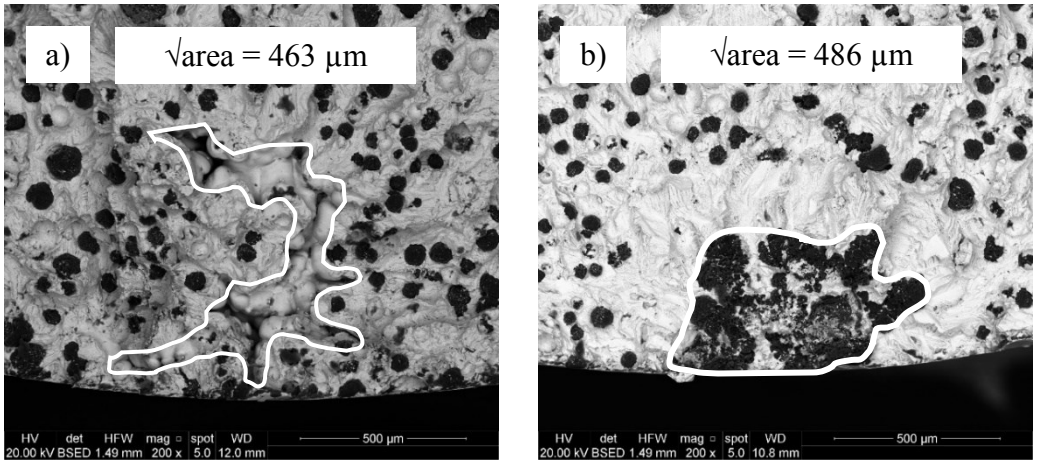

Figure 3.10. SEM images of fracture surfaces showing the dimensions (√area) of microshrinkage cavity (a) and degenerated graphite particle (b) that act as crack initiation sites.

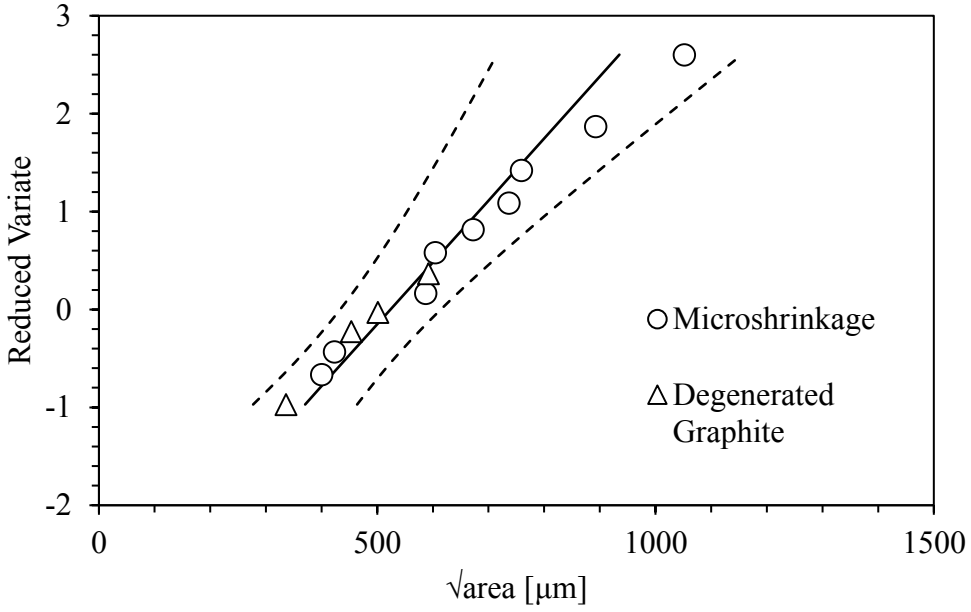

Figure 3.11. Extreme values distributions of initiating defects (microshrinkage and degenerated graphite particle) found in the casting.

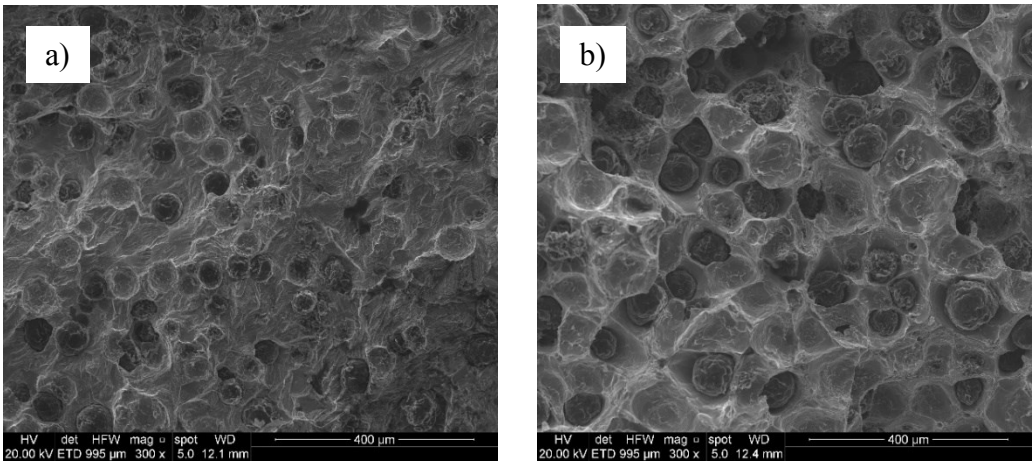

Figure 3.12. SEM images of fracture surfaces showing the crack propagation zone (a) and the static final failure (b).

3.6 Conclusions

In this chapter, the mechanical and fatigue properties traditional ferritic ductile cast iron GJS 400-18 LT, characterized by long solidification time, have been investigated.

Mechanical properties of the casting, characterized by long solidification time, were found to be not much lower than typical values obtained from the standard samples. Moreover, it is worth noticing that they are homogenous in the considered zones.

Samples failed under fatigue loading showed microshrinkage porosities or degenerated graphite particles, which have been identified as crack initiation sites. It has been observed that crack propagated in the material along the interface between the matrix and the spheroidal graphite particles, while the static final failure happens in a ductile manner, with dimple fracture and microvoids coalescence.

4. *Traditional Pearlitic ductile iron (GJS 700-2)*

Borsato, T., Ferro, P., Berto, F., Carollo, C., 2017. Fatigue strength improvement of heavy-section pearlitic ductile iron castings by in-mould inoculation treatment. Int. J. Fatigue 102, 221–227. doi:10.1016/j.ijfatigue.2017.02.012

Highlights

Casting defects like microshrinkage porosity or degenerate graphite play a major role in fatigue behaviour of ductile cast iron. This phenomenon is even more evident in heavy-section ductile iron castings where defects are more frequent and difficult to control. This chapter is aimed to investigate the fatigue behaviour of heavy-section pearlitic ductile iron castings obtained with different in-mould inoculation treatments. It has been found that the inoculation process modifies the microstructure of the alloy, dimension and morphology of defects. The higher the nodule count, the lower the microshrinkage cavities dimensions.

The fracture surface of broken samples has been investigated by means of Scanning Electron Microscopy in order to identify crack initiation points and fracture mechanisms. Metallographic analyses have been carried out to measure nodule count and nodules dimensions and to identify the matrix microstructure. Statistics of extreme values and Murakami approach have been used to analyse the influence of defects on the fatigue behaviour of the materials analysed. It was found that a synergic effect between degenerate graphite particles and microshrinkage porosities reduces the fatigue strength of pearlitic ductile iron castings.

4.1 Materials

Three different pearlitic ductile irons (named A, B, E) were analysed, nominally EN GJS 700-2, whose final chemical compositions are reported in Table 4.1. Melts were prepared in medium frequency induction furnace from pig iron, steel scrap and ductile cast iron returns. The spheroidizing treatments and the preconditioning were performed in a dedicated ladle by adding FeSiMg alloy (44–48%Si, 5.75–6.25%Mg, 0–0.80%Al,1.05–1.45%Ca, 0–0.10%RE, Fe bal.,wt%) and preconditioner (60-67%Si, 0.7–1.7%Al, 9–11%Ba, 0.4-0.7%Ca, Fe bal.,wt%). Slag was then removed and the melt was poured into the pouring ladle where a new inoculation (73-78%Si, 1.0–1.5%Al, 2.0-2.5%Ca, 1.3-1.8%Zr Fe bal.,wt%) was carried out. In order to differentiate the castings, only the in-mould inoculation treatments have been changed, using adjusted amounts of different types of commercial inoculants, based on foundry experience (Table 4.2). In particular, it can be noted that, for A and E castings, different amounts of the same inoculant (I) have been used, while a combination of two types of inoculants (II and III) containing RE and Bi has been used for B casting. The castings used in this work were blocks of dimensions 300x250x300 mm3 with feeders on top surfaces, produced in furan resin sand mould; these dimensions were chosen with the aim to enhance the thermal modulus (defined as the ratio of casting volume to the surface area for heat exchange between casting and mould). Each block was sectioned in order to obtain specimens from the areas of most interest to this work which are those characterized by the longest solidification time and lower cooling rate. To identify these zones and calculate their solidification time, a finite elements analysis was carried out by using the numerical code Novaflow&Solid®. Specimens were machined according to the geometry shown in Figure 4.1. Cylindrical smooth specimens with a net diameter of 10 mm were made with a fillet radius of 52 mm, in order to have a theoretical stress concentration factor kt near to 1. Tensile and fatigue tests were carried out at room temperature by using a universal MTS machine (250 kN). Fatigue life tests were conducted by using a sinusoidal signal in uniaxial tension with a frequency of 15 Hz and a load ratio R=0. The fracture surfaces of some samples were investigated by means Field Emission Gun – Environmental Scanning Electron Microscope, FEG-ESEM, (FEI, Quanta 250

FEG) in order to identify crack initiation zones and fracture mechanisms. With the aim to evaluate the influence of microstructure on fatigue strength, metallographic analyses were carried out in a section near the fracture surface of fatigue specimens. In particular, following the ASTM E2567 standard, nodule count and nodule size were evaluated using an optical microscope interfaced with an image analysis software.

With the purpose to predict the maximum size of microshrinkage cavities and to estimate the lower bound of fatigue strength, analysis of statistics of extreme values was performed according to ASTM E2283-08 on metallographic samples taken from the fatigue specimens of each casting.

Specimens were taken from that zone characterized by a thermal modulus between 5.6 and 5.8 cm, corresponding to solidification times of about 160 ÷ 170 minutes. From each block, eight specimens were obtained (Figure 4.2).

Table 4.1. Final chemical composition of the castings (wt%).

Casting	C	Si	S	P	Mn	Cr	Cu	Mg
A	3.65	1.95	0.009	0.018	0.3	0.03	1.25	0.059
B	3.75	2.25	0.009	0.017	0.3	0.025	1.20	0.063
E	3.58	2.4	0.007	0.021	0.36	0.033	1.12	0.054

Table 4.2. Chemical compositions of the in-mould inoculants (wt%).

Casting	Inoculant code	wt%	Si	Al	Ca	RE	Bi
A	I	0.1	70 - 78	3.2 - 4.5	0.3 - 1.5		
B	II	0.075	70 - 75	0.8 - 1.2	0.8 - 1.2	0.8 - 1.2	0.8 - 1.2
B	III	0.075	70 - 75	3.5 - 4.5	<1.5	0.5 - 0.8	0.5 - 0.8
E	I	0.15	70 - 78	3.2 - 4.5	0.3 - 1.5		

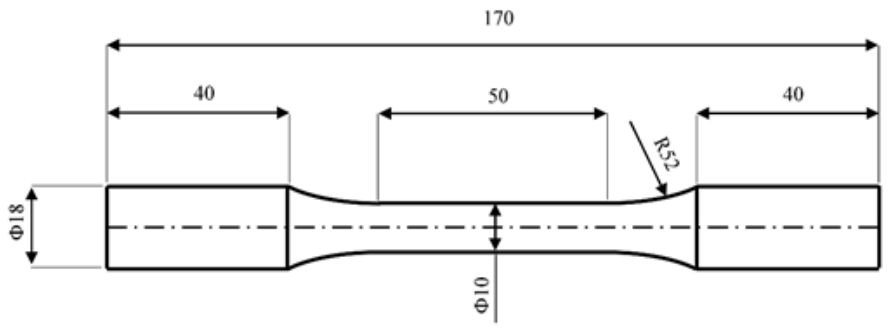

Figure 4.1. Geometry of the specimens for fatigue tests. Dimensions in mm.

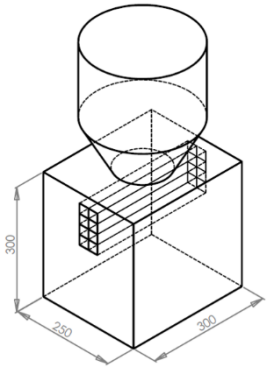

Figure 4.2. Schematic showing casting positions where specimens were taken. Dimensions in mm.

4.2 Numerical simulation

A numerical analysis was carried out by using the code Novaflow&Solid®. In particular, the model containing the block, the feeder and the gating system was meshed using a cell dimension equal to 7 mm (see Figure 4.3). The temperature dependent material properties (for cast iron and sand) have been taken from the database of the numerical code. The simulation has been carried out considering both the pouring and the solidification stages. Materials chemical compositions (Table 4.1), type of sand (furan resin sand with 300 mm in thickness) and pouring temperatures (1330 °C) were inserted as input data into the model. In order to extract the temperature profile during cooling and solidification, virtual thermocouples have been defined in different points of the FE model. In particular, starting from the upper surface of the block, the thermocouples have been created every 50 mm, until reached the lower surface.

Both mould filling and melt solidification have been simulated. Specimens were taken from that zone characterized by a thermal modulus between 5.6 and 5.8 cm, corresponding to solidification times of about 160 ÷ 170 minutes. From each block, eight specimens were obtained. Figure 4.4 shows the temperatures profiles corresponding to the zones characterized by the longest solidification time from where the specimens were taken.

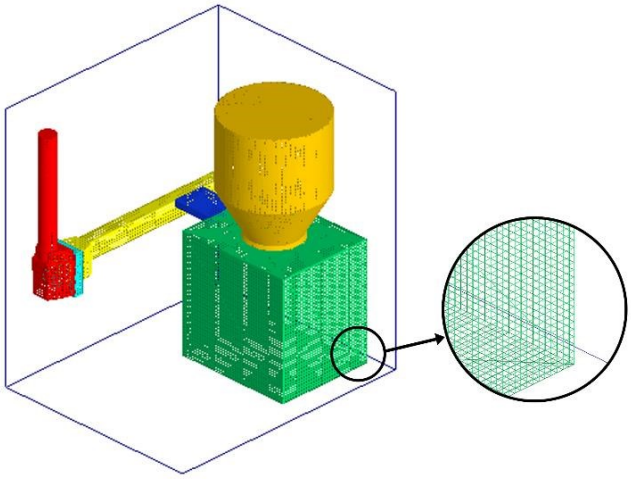

Figure 4.3. Geometry of the model used in Novaflow&Solid® and a particular of the mesh (cell dimension equal to 7 mm).

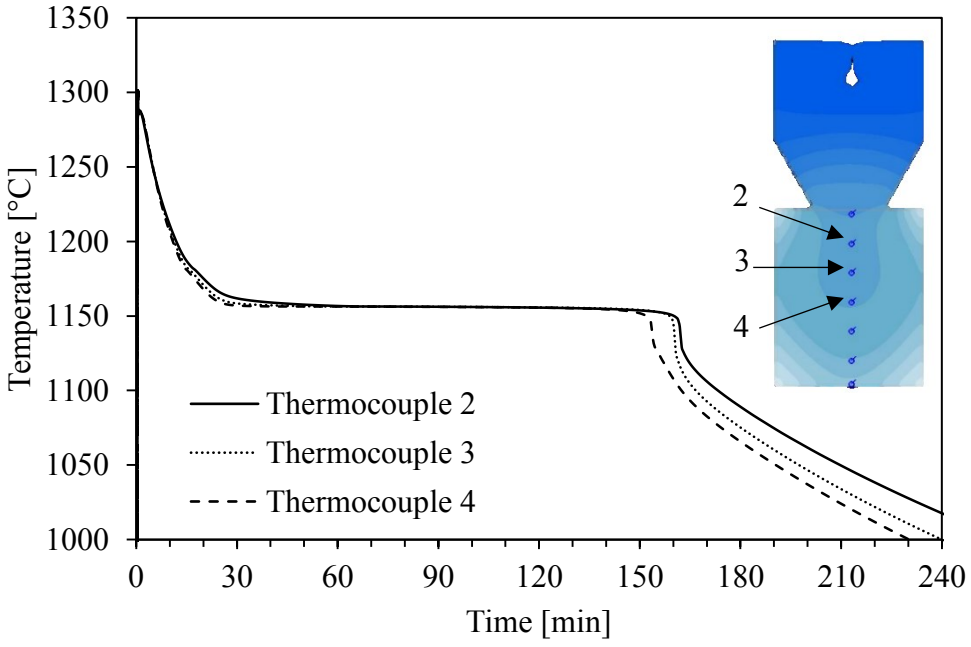

Figure 4.4. Simulated temperature profiles recorded by the virtual thermocouples.

4.3 Tensile and Brinell Hardness tests

Data obtained from tensile tests are reported in Table 4.3. It can be observed that, although the materials were classified as EN GJS 700-2 ductile iron, the real values of ultimate tensile strength and yield strength are much lower than the nominal ones. This can be explained by the fact that specimens were taken from the areas characterized by the longest solidification times (about 3 hours) and lowest cooling rate, where it is difficult to control the microstructure. In particular, these zones are characterized by a coarse microstructure, low nodule count and graphite particles that deviate from the ideal spherical shape, segregation of alloying elements and microshrinkage porosities that have detrimental effects on the mechanical properties of the material. It can be observed that A casting was characterized by the higher ultimate tensile strength (579 MPa), but by the lower yield strength (364 MPa). E Casting showed the lower ultimate tensile strength (511 MPa), similar to that of B casting, but the higher yield strength (410 MPa). It can be deduced that inoculation treatments influence the mechanical properties of castings.

Brinell hardness tests have been performed according to UNI EN ISO 6506:2006 using a test machine with an indenter diameter of 5 mm and force-diameter ratio $0.102 \cdot F/D^2$ equal to 30 N/mm^2. Tests have been made on 15 samples taken from different areas from each casting varying the distance from the top surface. Mean value of Brinell hardness was found to be equal to 220 HB for all the castings.

Table 4.3. Mechanical properties of specimens taken from the castings.

Casting	σ_{UTS} [MPa]	$\sigma_{y\ 0.2\%}$ [MPa]	ε_R %
A	579 ± 5.1	364 ± 3.4	2.6 ± 0.3
B	513 ± 10.3	368 ± 4	1.9 ± 0.2
E	511 ± 6.2	410 ± 0.9	2 ± 0.4

4.4 Fatigue test

Results obtained from the statistical elaboration of fatigue tests data for A, B and E castings are reported in Figures 4.5, 4.6 and 4.7 respectively. Values of stress amplitude related to a survival probability of 50%, the slope of the Wöhler curve and the scatter index T_σ (the ratio between the stress amplitudes corresponding to 10% and 90% of survival probability) are reported in the above cited figures. Specimens survived over 2 million cycles are considered as run out and marked up with an arrow. It can be noted that the difference between the Wöhler curves are related both to the mean value of the stress amplitude at $2 \cdot 10^6$ cycles, and to the scatter index T_σ. In particular, A casting showed the lower value of the fatigue limit (120 MPa) and the higher scatter index, resulting in the worst fatigue behaviour. This can be explained by the fact that in some specimens, large and diffused shrinkage porosities were found on the fracture surfaces. On the contrary, B and E castings showed increased fatigue limits (134 and 140 MPa respectively) with narrowed scatter bands.

It is worth noting that, when the three kind of specimens are considered all together in the statistical analysis, the fatigue curve (Figure 4.8) is characterized by a mean stress amplitude of 135 MPa at $2 \cdot 10^6$ cycles and a low scatter index equal to 1.22. It is also important to highline that "E" specimens are always above the others. Moreover, specimens that did not fall inside the band were those characterized by large and diffused shrinkage porosities probably due to a non-optimal inoculation treatment.

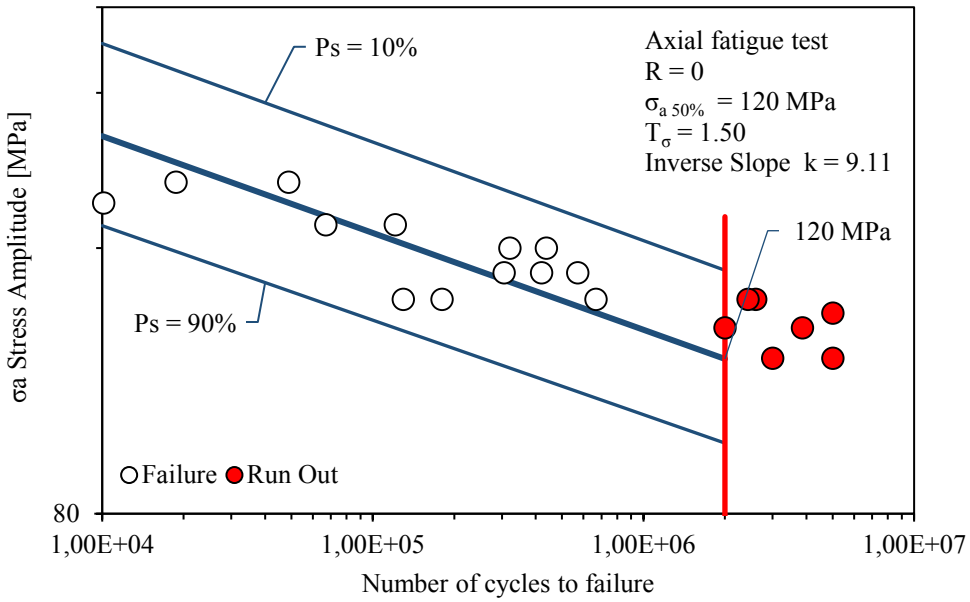

Figure 4.5. Fatigue life of specimens taken from casting A.

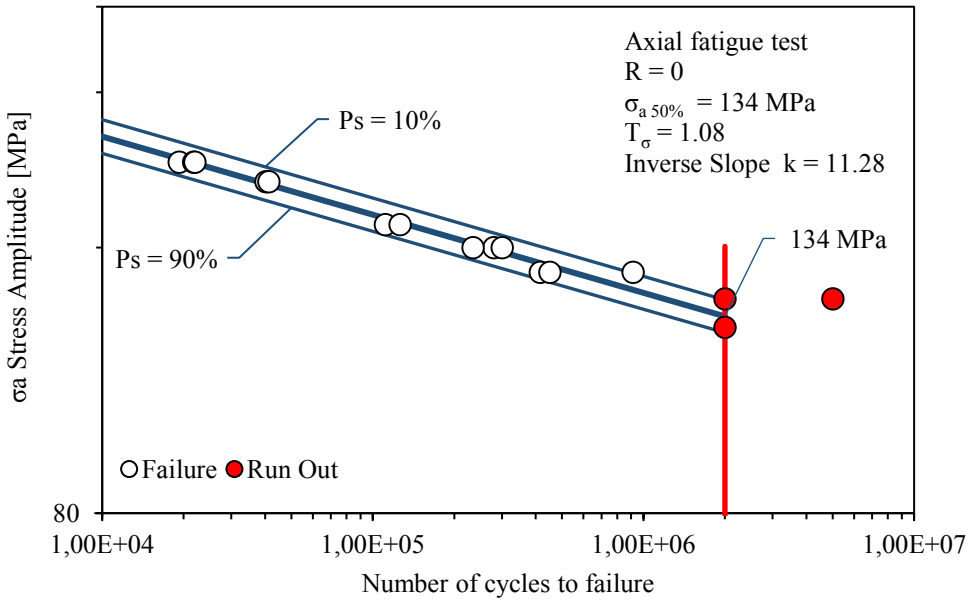

Figure 4.6. Fatigue life of specimens taken from casting B.

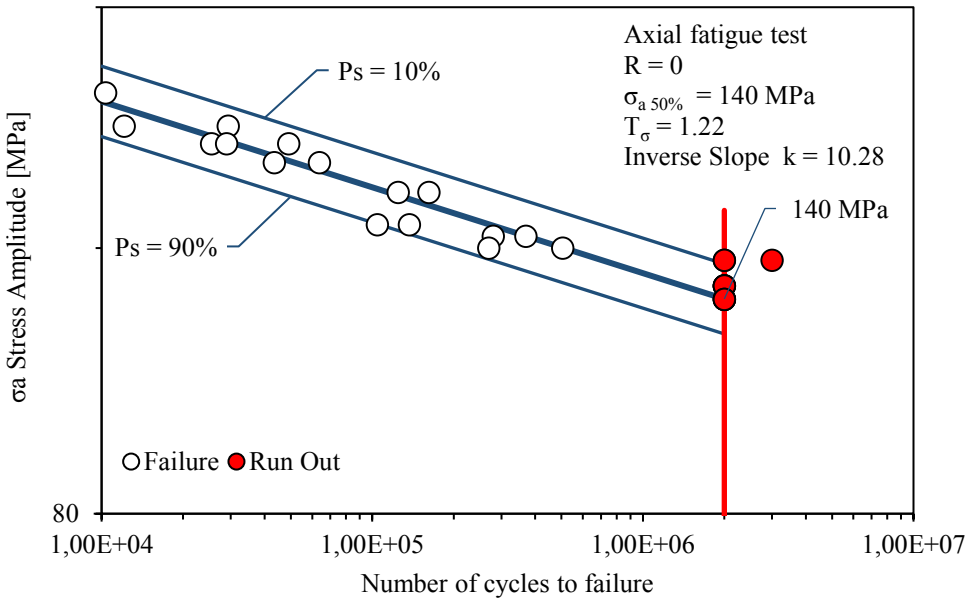

Figure 4.7. Fatigue life of specimens taken from casting E.

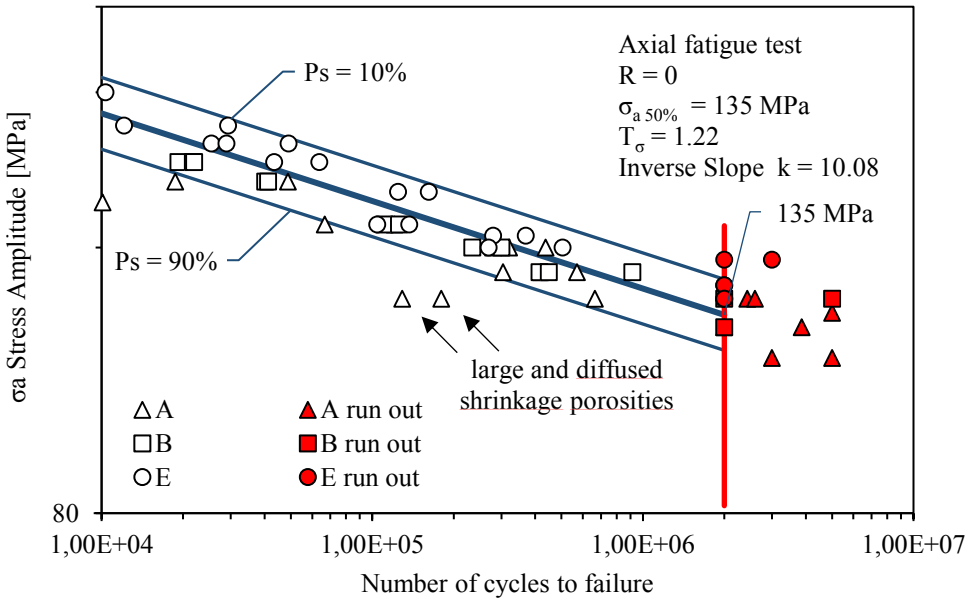

Figure 4.8. Fatigue life of specimens taken from castings A, B and E.

4.5 Microstructure and fractography

The microstructure close to the fracture surface of fatigue test specimens was investigated by optical microscope (OM). An image analysis system, interfaced with the OM, was used to measure the nodule count and nodule size of the graphite particles according to ASTM E2567. Only those particles with Type I or Type II shape were considered as graphite nodules. The results of image analysis are summarized in Table 4.4. Micrographs of specimens taken from the castings are shown in Figure 4.9. It can be noted a better microstructure on B and E castings, characterized by higher nodule count, compared to A, which presents the higher value of mean nodule diameter. Considering the same type of in-mould inoculant, it can be inferred that the treatment, performed with an amount of 0.15 wt% (E casting), has a better effect on the final microstructure of the large casting analysed, than 0.1 wt% used in A (Table 4.2). It is worth noticing that in some specimens taken from B casting, characterized by the higher nodule count and lower mean nodule diameter, small amount of degenerated spiky graphite has been found. A micrograph of such a defect is shown in Figure 4.10. After etching with 5% Nital, micrographs of all the samples show a pearlitic matrix with some percentage of ferrite at the grain boundaries that surrounds the graphite nodules (Figure 4.9).

The formation of such degenerated graphite shape is attributed, in literature, to the presence in the melt of detrimental elements such as lead, antimony, bismuth. This last, present in inoculants used for B casting (Table 4.2), can help to give high number of rounder and smaller graphite nodules (as shown in the Table 4.4), but can cause the formation of spiky graphite structures. The use of nodulariser containing rare earths may prevent this type of defect. However, the effect of changes in the spheroidizing treatments was not considered in this work.

Table 4.4. Microstructural properties of samples.

Casting	Nodule Count (mm^{-2})	Mean Nodule Diameter (μm)
A	26 ± 15	66 ± 15
B	52 ± 17	45 ± 6
E	46 ± 7	55 ± 17

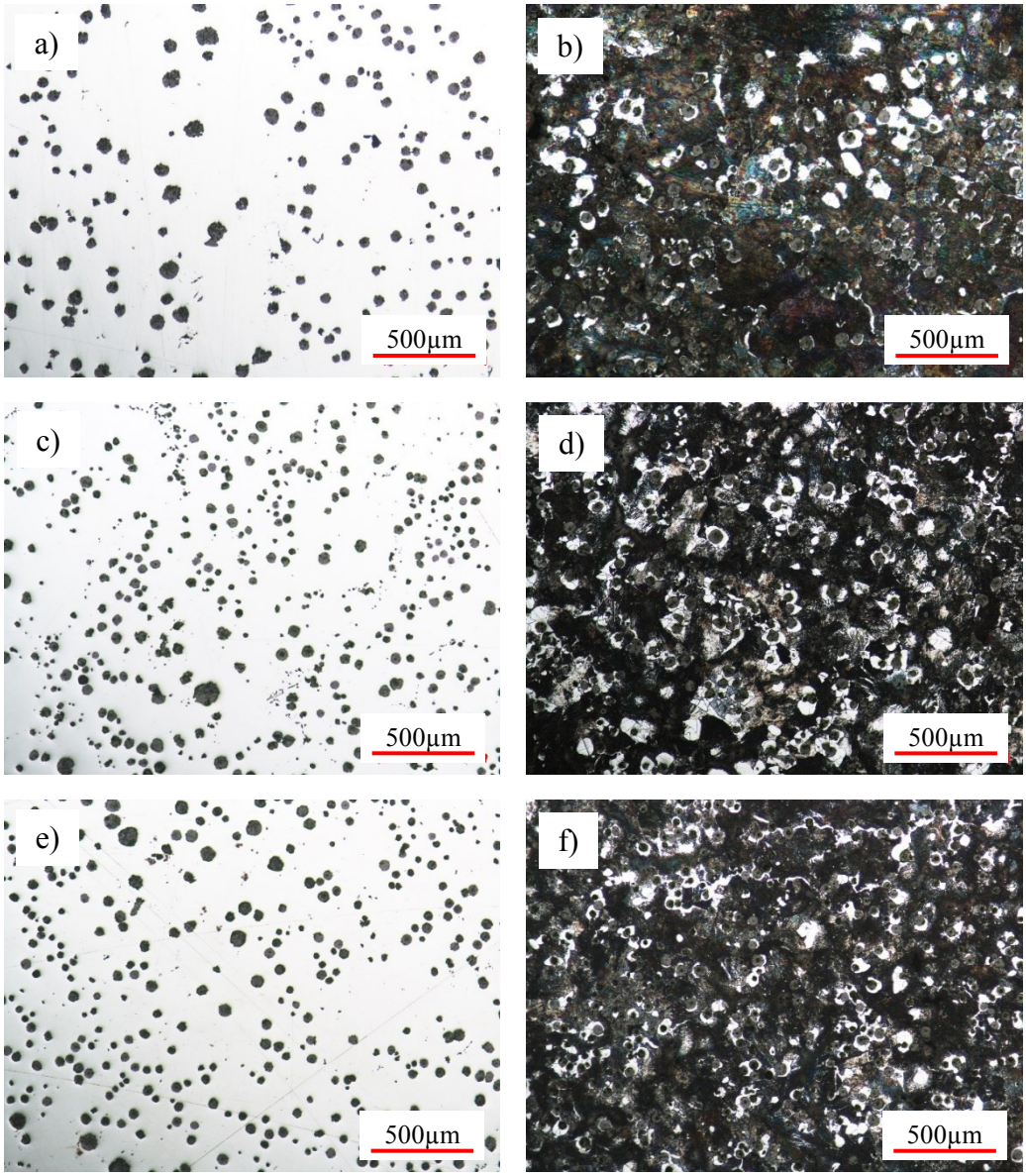

Figure 4.9. Micrographs of specimens taken from A (a,b), B (c,d) and E (e,f) castings, unetched (left column) and etched (right column) with 5% Nital.

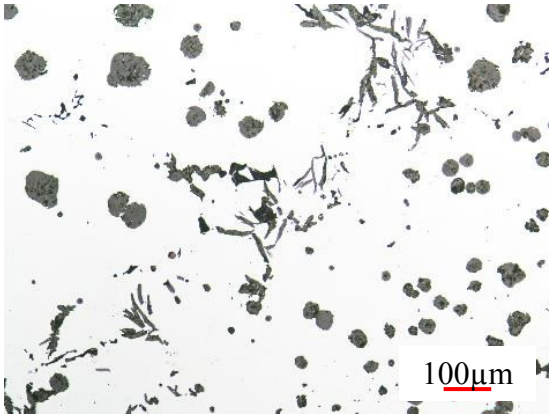

Figure 4.10. Micrograph of degenerated graphite from B casting.

Fracture surfaces of broken specimens under fatigue loading have been investigated. A panoramic overview of a fracture surface is shown in Figure 4.11, where crack initiation, propagation and static failure zones can be identified.

Figure 4.12a, b and c, shows shrinkage porosities near the surface of the samples that have been identified as cracks initiation sites. It can also be observed the presence of degenerated graphite particles (spiky graphite) near the porosity of B casting (Figure 4.12b). It has also been found that the fatigue cracks propagate passing around the graphite nodules, along the metal matrix/graphite interface (Figure 4.12d), while final failure happens in a brittle manner by cleavage that occurs along crystallographic planes in each fractured pearlite colony (Figure 4.12e). An image of degenerated graphite particles, found in B casting, is also shown in Figure 4.12f.

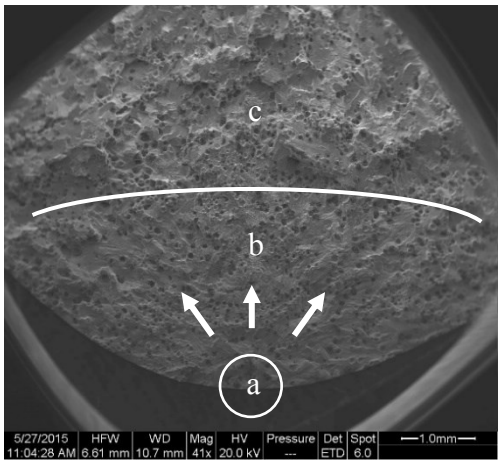

Figure 4.11. Example of a panoramic SEM micrograph of fracture surface showing crack initiation (a), propagation (b) and static failure (c) zones

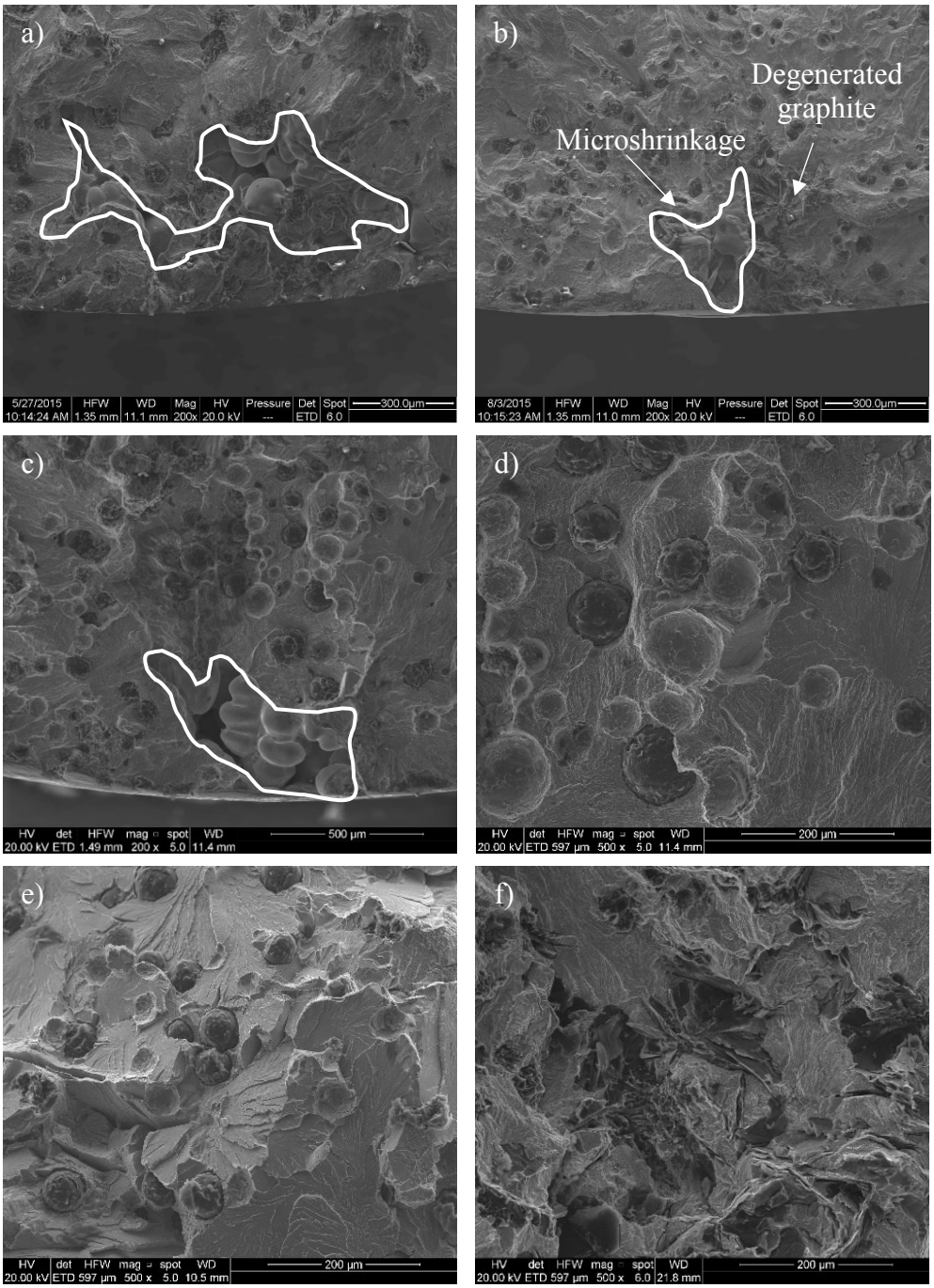

Figure 4.12. SEM micrographs of fatigue broken specimens showing examples of crack initiation zones corresponding to specimens taken from A (a), B(b) and E (c) castings, crack propagation zone (d), final static failure (e) and degenerated graphite (f) found in B casting.

4.6 Statistical analysis of extreme values

In table 4.5, the measurements of the initial microshrinkages (√area), performed on the fracture surfaces of fatigue specimens, are reported for the three castings. It can be observed that these cavities are on average greater in A casting than in B and E castings. This could be attributed to a better inoculation treatment that induces higher nodule count and graphite expansion effect that reduces shrinkage porosities dimensions. As shown in Figure 4.13, where the nodule count and the mean nodule diameter of the three castings are plotted versus the average size of initiating defects, it can be inferred that an increase in the number of graphite particles and a decrease in their dimensions reduce the size of microshrinkage porosities. This confirms the higher mean value of the stress amplitude $\sigma_{a,\,Ps\,50\%}$ at $2 \cdot 10^6$ cycles and the narrower scatter band observed in the fatigue life of cast iron B and E compared to that of cast iron A.

Table 4.5. Dimensions of the initiating microshrinkage cavities measured on fracture surface.

A casting		B casting		E casting	
Specimen	√area [μm]	Specimen	√area [μm]	Specimen	√area [μm]
A35	323	B34	262	E27	317
A31	514	B33	285	E13	389
A43	541	B48	311	E22	446
A26	553	B16	336	E9	454
A25	594	B44	396	E1	495
A32	618	B42	403	E7	499
A21	661	B37	445	E8	531
A13	739	B24	448	E18	533
A15	792	B12	495	E20	557
A41	829	B18	513	E21	563
A12	962	B22	578	E4	581
A45	967	B13	579	E3	583
A36	1267	B14	598	E5	607
				E19	621
Average	720 ± 246	Average	435 ± 115	Average	504 ± 84

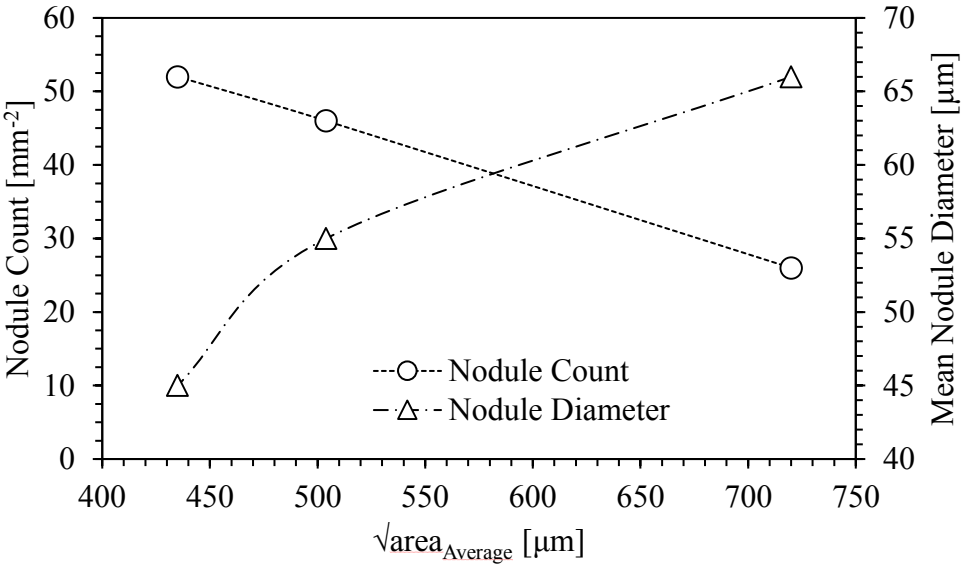

Figure 4.13. Nodule count and mean nodule diameter vs. average size of initiating microshrinkages for the three castings analysed.

In order to evaluate the effect of microshrinkage porosities and degenerated graphite particles on the fatigue resistance of the castings, extreme value analysis has been performed according to ASTM E2283-08.

For this reason, only the microshrinkage cavities dimension √area, for A, B and E castings, have been measured on metallographic sections and plotted on the extreme value cumulative probability paper (Figure 4.14), where the scale (δ) and local (λ) parameters of the distributions, calculated using the Maximum Likelihood (ML) method, are also reported for each casting, together with the best fit lines.

The expected maximum defect size $\sqrt{area}_{max}$ are shown in Table 4.6. It can be noted that, in agreement with fractographic investigation, the largest dimension has been predicted for A casting, while lower values have been estimated for B casting. It is also important to highlight that the expected maximum dimensions of defects are smaller than those measured on the fracture surface of the specimens, as the statistical analysis has been conducted on polished 2D sections.

To estimate the influence of microshrinkage cavities, the predicted $\sqrt{area}_{max}$, was used in the Murakami equation:

$$\sigma_w = F_{loc}\frac{(HV + 120)}{\sqrt{area}^{1/6}}\left(\frac{1-R}{2}\right)^{\alpha}$$

Where F_{loc} is the location factor being 1.43 for a surface defect and 1.41 for a defect just below the surface; HV is the Vickers hardness; α depends on the material and is given as $0.371+ HV \cdot 10^{-4}$ for ductile irons, R is the load ratio. Since the hardness, measured for the three castings, showed similar values, the variations on the predicted fatigue limits are only dependent on the size of the defects. The calculated fatigue limit of A casting, in agreement with the experimental results, is the lower of all castings, see Table 4.6. It can also be observed that, considering only the effect of microshrinkage porosities, the predicted fatigue strength of B casting is slightly higher than E. It could be inferred that, in view of the experimental results, a combined effect between the microshrinkages and the degenerated graphite particles (spiky graphite) gives an increased notch effect for the nucleation of the crack, reducing the fatigue strength.

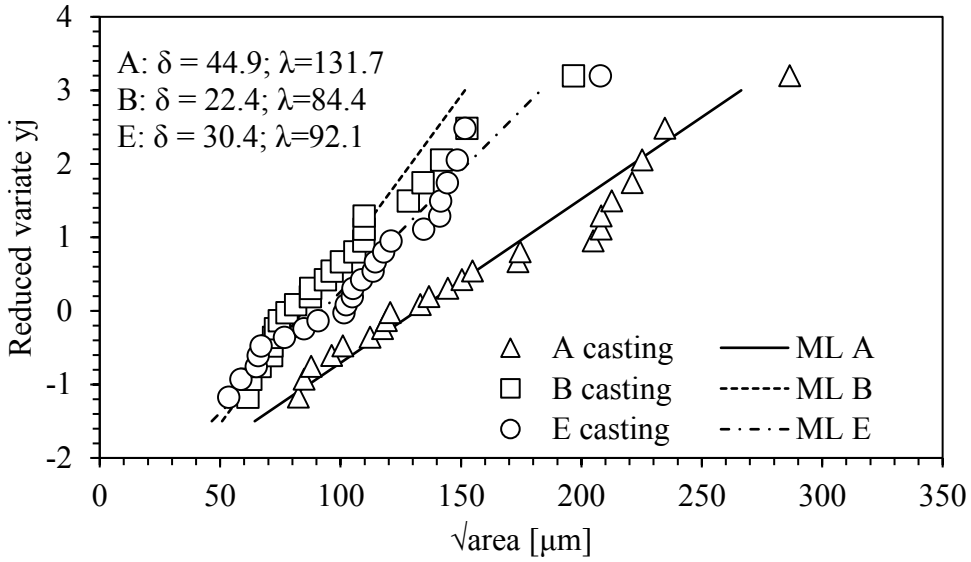

Figure 4.14. Cumulative probability distributions of microshrinkage dimension for the castings analysed.

Table 4.6. Expected values of and lower bound of the fatigue limit for A, B and E castings.

	Expected $\sqrt{area}_{max}$ [μm]	Expected lower bound of fatigue limit σ_w [MPa]
A casting	669	123
B casting	353	137
E casting	455	132

4.7 Conclusions

Tensile and fatigue tests, metallographic and fractographic analysis have been carried out on specimens taken from heavy section pearlitic ductile iron (EN-GJS 700-2) castings characterized by solidification times of about 3 hours. In particular, the influence of in-mould inoculation treatments (see Table 4.2) on microstructure, mechanical properties and fatigue behaviour of the material have been investigated. Finally, microstructural parameters and defects have been correlated to mechanical properties of the alloy.

It has been found that the in-mould inoculation treatment affects the metallurgical parameters of the casting with nodularity and mean nodule count of casting B and E higher than those measured on casting A. However, in casting B, small amount of degenerated graphite, classified as spiky graphite, has been found in the zones that take longer to solidify. This was attributed to the presence of Bismuth in the chemical composition of inoculants used. Mechanical properties of specimens taken from the castings are much lower than the nominal values of an EN GJS 700-2, due to the long solidification times. In particular, ultimate tensile strength has been found to be higher for casting A, while the yield stress was higher for casting E, highlighting that inoculation treatments had an influence on mechanical properties of heavy section castings. A casting showed the lower value of the fatigue limit (120 MPa) and the higher scatter index, resulting in the worst fatigue behaviour, due to the presence of large shrinkage porosities. On the other hand, castings B and E showed increased fatigue limits (134 and 140 MPa respectively) with narrowed scatter bands. Fractography of specimens showed that microshrinkage porosities close to the surface of the specimens act as crack initiation points from which the fatigue crack propagates around the graphite nodules. In B casting, however, a combination of microshrinkage porosities and degenerated graphite particles has been found to be at the origin of crack initiation. The measurement of the initial microshrinkage cavities dimensions showed that A casting is characterized by the larger defects compared to B and E castings. It was also found a good correlation between nodule count and mean nodule diameter and the √area of microporosity, highlighting the fact that higher nodule count reduces shrinkage porosities dimensions. The statistical analysis of extreme values has been

used to evaluate the size-distribution of defects for the three castings, and its effect on the lower bound of fatigue limit was evaluated using the Murakami approach. It was found that the calculated fatigue limit of A casting, in agreement with the experimental results, is the lowest among all the castings. From the results obtained for B and E castings, it can be also inferred that exists a combined effect between microshrinkage porosities and degenerated graphite particles (spiky graphite) that gives an increased notch effect for the crack nucleation and thus a reduction of the fatigue strength of the material.

5. *Solution strengthened ferritic ductile iron. Influence of long solidification times.*

Borsato, T., Ferro, P., Berto, F., Carollo, C., 2018. Influence of solidification defects on the fatigue behaviour of heavy section silicon solution strengthened ferritic ductile cast irons. Fatigue Fract. Eng. Mater. Struct. 41, 2231-2238.

Highlights

Mechanical and fatigue properties of heavy section solution strengthened ferritic ductile iron (SSF-DI) castings have been examined in this chapter. Amounts of Silicon varying from 3.2 to 3.55 wt% have been used. The effect of Antimony on counteracting the formation of chunky graphite (CHG) has been evaluated. In order to estimate the influence of solidification defects (microshrinkage porosities or degenerated graphite particles) on the fatigue strength of the investigated materials, SEM observations of the fracture surfaces and extreme value analysis of the crack initiating defect dimension, √area, have been performed. The propagation of the fatigue crack through the material has been observed by means of microstructural analysis of the cross sections of the fracture surfaces.

It has been found that the treatment with Sb is useful to avoid the formation of degenerated graphite particles. Moreover, it has been observed that the most of the fatigue life is spent in the crack initiation stage, where the microshrinkage porosities play a major role. The presence of chunky graphite affects mostly the propagation stage.

Finally, mechanical and fatigue properties of SSF-DI have been compared with those obtained from traditional ductile cast iron specimens taken from the same casting geometry.

5.1 Materials

The materials under investigation were three different solution strengthened ferritic ductile cast irons, named 3.2Si-Sb, 3.5Si-Sb and 3.55Si, the final chemical compositions of which are reported in Table 1. In particular, an increasing amount of Silicon varying from 3.2 to 3.55 wt% was used and, as suggested in UNI EN 1563:2012 standard, the carbon content has been decreased correspondingly in order to maintain a near-eutectic composition. Carbon equivalent has been evaluated according to the well-known equation: C_{eq}=C%+0.33(Si%+P%). Moreover, for 3.2Si-Sb and 3.5Si-Sb castings, 15 ppm of Sb were added in order to evaluate the effect of this element on counteracting the formation of chunky graphite in the thermal centre of heavy section castings. In the case of 3.55Si casting, Sb was not used. The castings geometry were blocks of dimensions 300x250x300 mm^3 with feeders on top surfaces, characterized by a solidification time of about 3 hours. Moreover, using the same alloy of 3.2Si-Sb, also a cylindrical casting with diameter equal to 300 mm and height 520 mm was produced (identify as 3.2Si-Sb ø300), characterized by solidification time, in the thermal centre, similar to the other geometry. Specimens were taken from the areas that take longer to solidify inside the castings; in particular pieces of about 25x25x300 mm^3 were cut using a bench saw and then machined using a CNC machining centre.

Moreover, Y-shaped type IV cast samples (according to UNI EN 1563:2012 standard) have been produced in separated sand moulds. In this case, the samples were cut according to the sectioning procedure shown in the standard and then specimens, with a net diameter of 14 mm, were obtained.

Tensile tests have been carried out at room temperature according to UNI EN 1563:2012 standard both on separately cast samples (75 mm in thickness) and on specimens taken from the castings.

Table 5.1. Final chemical composition of the castings.

Casting	C	Si	S	P	Mn	Sb	Mg	Ceq
3.2Si-Sb	3.18	3.22	0.007	0.022	0.19	0.0015	0.043	4.26
3.5Si-Sb	3.14	3.50	0.007	0.026	0.19	0.0015	0.058	4.31
3.55Si	3.10	3.55	0.007	0.025	0.19	-	0.060	4.30

5.2 Microstructure

Micrographs taken from 3.2Si-Sb and 3.5Si-Sb (Figure 5.1a and b) showed a homogeneous structure with spheroidal graphite nodules within a ferritic matrix, with very few traces of pearlitic areas, due to segregation of carbide forming elements in the last to solidify zone (Figure 5.1d). Some microstructural defects have been found, such as microshrinkage porosity and a small amount of branched and interconnected degenerated graphite, classified as chunky graphite (CHG), slightly higher in the case of casting 3.5Si-Sb. This seems to confirm that the increase of the Silicon content could promote the formation of this type of defect. However, due to the limited amount of CHG in the two castings, the treatment with Antimony seems to be effective in preventing the formation of such degenerated graphite. Conversely, in the centre of casting 3.55Si, that was not treated with Sb, a large amount of chunky graphite was found (Figure 5.1c).

Nodule count and nodule size have been evaluated according to ASTM E2567-11 on a number of images in order to cover an observation area of more than 150 mm^2. In the case of casting with 3.55 wt% Silicon, it was not possible to evaluate nodule count due to the presence of chunky graphite particles. A summary of the microstructural properties is presented in Table 5.2. It can be noted that mean nodule count was found to be not very high and consequently, mean nodule diameter was found to be quite large for both the castings. In the case of 3.2Si-Sb, the microstructural parameters are similar considering the two different casting geometries, highlighting the fact that the cooling conditions are almost the same.

Table 5.2. Microstructural properties of samples

Casting	Nodule Count (mm^{-2})	Mean Nodule Diameter (μm)
3.2Si-Sb	38	49 ± 16
3.2Si-Sb ø300	40	49 ± 16
3.5Si-Sb	48	46 ± 17
3.55Si	-	-

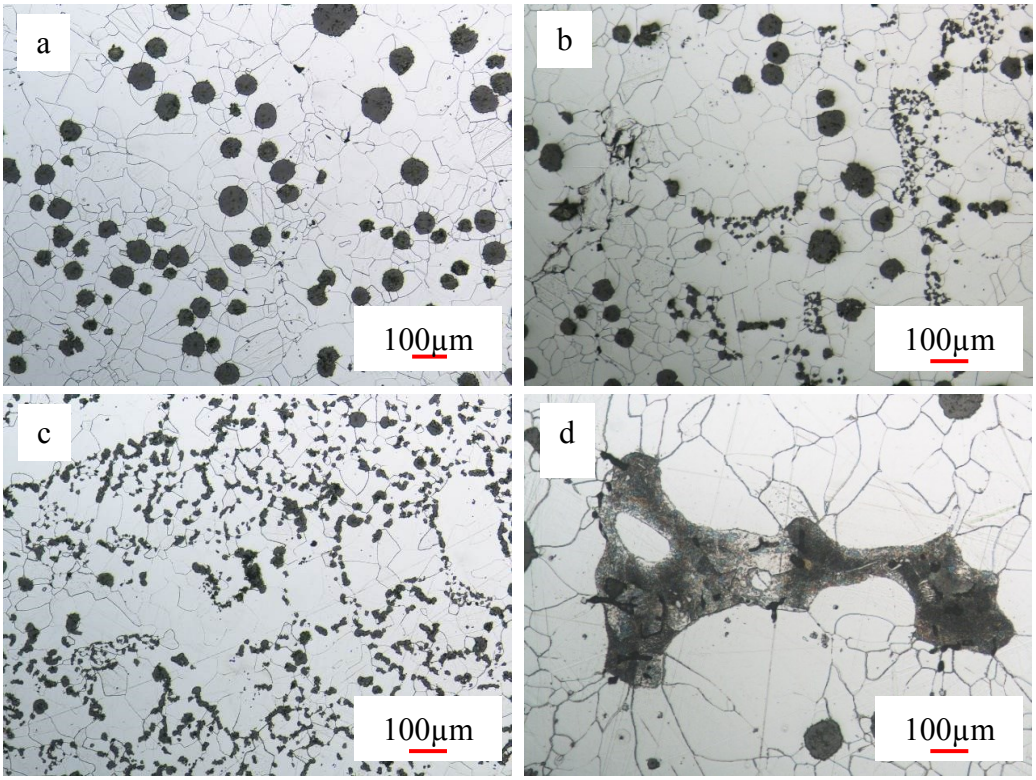

Figure 5.1. Micrographs of specimens taken from casting 3.2Si-Sb (a), 3.5Si-Sb (b) and 3.55Si (c), etched with Nital 5% and example of pearlite found in the last to solidify zone due to segregation.

5.3 Static mechanical properties

The results of tensile tests performed on specimens cut from 75 mm separately cast samples are shown in Table 5.3. The materials are characterized by high strength and ductility, high ratio between yield and ultimate tensile stress and high values of elongation at failure. It can also be observed that, as reported in the introduction, by increasing the amount of Silicon (from 3.2 to 3.55 wt%), both the ultimate tensile strength and yield stress increase, while elongation to failure decreases.

With the purpose of evaluating the influence of solidification times on mechanical properties, ten tensile specimens for each casting have been taken from the zone with the longest solidification times. In Table 5.3, the tensile test results of specimens taken from the castings are also listed. It is worth noticing that standard deviation values are very limited, deducting that mechanical properties are very homogeneous in the whole casting. It can also be noted that the different castings produced with an amount of Silicon of 3.2wt% are characterized by the same mechanical properties, confirming once again that the solidification conditions are almost the same. Moreover, in the case of long solidification times, considering castings 3.2Si-Sb and 3.5Si-Sb, the increased amount of Silicon increases the strength and decreases the ductility. In the case of casting 3.55Si, characterized by the highest Silicon content, one would expect the highest strength, but, due to the presence of chunky graphite, the ultimate tensile stress and, more markedly, the elongation at failure showed a considerable reduction with respect to 3.5Si-Sb casting. Moreover, it is important to note that, despite the presence of degenerated graphite, the yield strength increases as the Silicon content increases.

Finally, it is confirmed that, considering the properties inside the casting, SSF DIs show ultimate tensile strengths and yield stresses comparable with those found for the pearlitic grades GJS 700-2, while maintaining high ductility, close to the values of a traditional ferritic grade GJS 400-18 LT.

Brinell hardness tests have been performed according to UNI EN ISO 6506:2006 using a test machine with an indenter diameter of 5 mm and force-diameter ratio $0.102 \cdot F/D^2$ equal to 30 N/mm^2. Tests have been made on 15 samples taken from different areas from each casting varying the distance from the top surface. Mean

value of Brinell hardness was found to be equal to 190 HB for 3.2Si-Sb, while it was 195 HB for the other two materials.

From the core of 3.2Si-Sb casting, samples according to ISO 148-1 have been machined to evaluate the Charpy V-notch impact energy at room temperature and at -20°C. In Table 5.4 the values of impact energy [J] and specific energy [J cm-2] are shown for the two temperatures investigated. It can be noted that, as reported in literature, high Si level reduces the impact energy of spheroidal graphite cast iron. These values are, however, comparable with those of pearlitic ductile irons.

Table 5.3. Tensile test results of specimens taken from separated cast samples and from the castings for solution strengthened ferritic, pearlitic and ferritic ductile cast irons.

Material	75 mm samples			Specimens from castings		
	σ_{UTS} [MPa]	$\sigma_{y0.2\%}$ [MPa]	ε_R %	σ_{UTS} [MPa]	$\sigma_{y0.2\%}$ [MPa]	ε_R %
3.2Si-Sb	565	424	17.8	485.3 ± 1.8	381.2 ± 2.7	17.8 ± 1.0
3.2Si-Sb ø300				489 ± 2.1	384.0 ± 1.1	17.8 ± 1.4
3.5Si-Sb	601	450	15.4	511.1 ± 3.0	412.3 ± 2.9	15.4 ± 1.7
3.55Si	614	458	15.1	488.6 ± 7.9	430.4 ± 1.8	5.2 ± 1.1
GJS 700-2	735	425	4.1	513.8 ± 10.1	368.6 ± 4.0	2.0 ± 0.2
GJS400-18LT	400	262	23.4	383.1 ± 7.4	250.3 ± 4.2	19.9 ± 2.3

Table 5.4. Charpy V-notch impact test results (striker KV_2).

Temperature	Energy [J]	Specific energy [J cm^{-2}]
Room Temperature	5 ± 0.5	6.2 ± 0.6
-20°C	3.8 ± 0.6	4.7 ± 0.8

5.4 Fatigue tests

The results of fatigue tests have been statistically analysed and the curves relative to survival probability of 10%, 50% and 90% were calculated using a log-normal distribution; the run out specimens that exceeded two million cycles were not included in the statistical re-analysis. In Figures 5.2, 5.3 and 5.4, the fatigue curves of the castings are shown. It can be noted that, although the differences in the mechanical properties and microstructures, the fatigue behaviours of the three castings were found to be very similar in terms of fatigue strength, slope and scatter index T_σ. This is quite surprising, as one would expect a higher fatigue strength with increasing the mechanical properties.

It was observed that during the fatigue tests, a large part of the fatigue life was spent in the crack initiation stage, while the final failure happened with a very short propagation This can be proved by considering the resonant frequency of the tests; the Rumul machine performs loading cycles at a resonance frequency that depends on the elastic modulus of the material and specimen geometry, among other variables. Crack propagation will reduce the specimen cross-sectional area, and thus its stiffness and resonance frequency. It is well visible in Figure 5.5 that the normalized resonant frequency measured during the tests decreases when the specimens exceed 90% of the total life. This happens both for degenerated and good graphite containing specimens considering a stress amplitude equal to σ_a = 140 MPa, stress level close to the calculated fatigue resistance. Since the fatigue strength between the specimens was found only slightly different, it can be deduced that the mechanisms tied to crack-initiation stage are here more important than those tied to the propagation.

Finally, in order to evaluate the influence of the load conditions, specimens taken from the cylindrical casting (3.2Si-Sb ø300) have been tested under alternate pulsating loading conditions (R=-1). Fatigue data and calculated fatigue curves are shown in Figure 5.6, where it can be observed that the fatigue strength, at 2 million cycles and survival probability equal to 50%, has been found to be 184 MPa.

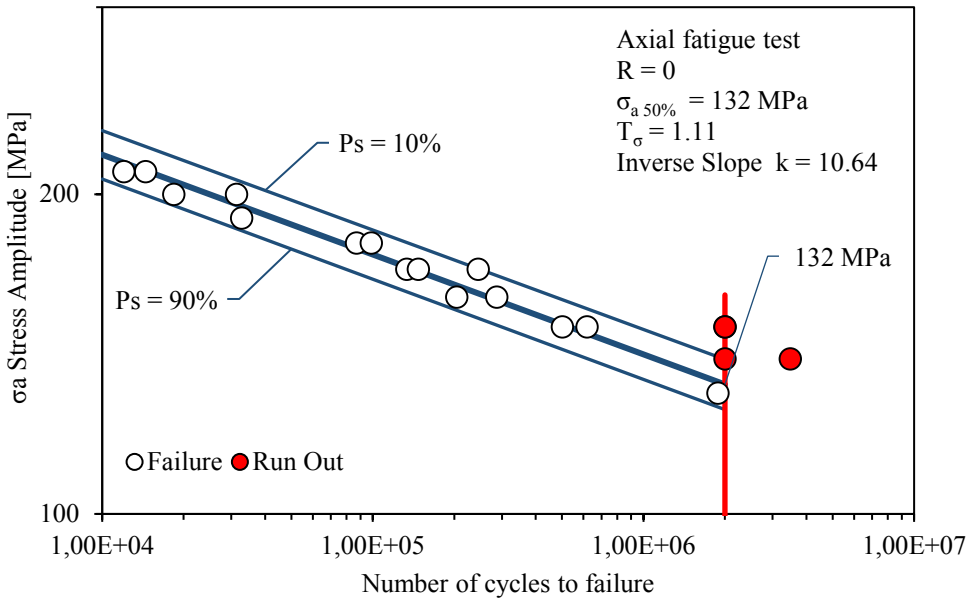

Figure 5.2. Fatigue life of specimens taken from 3.2Si-Sb casting.

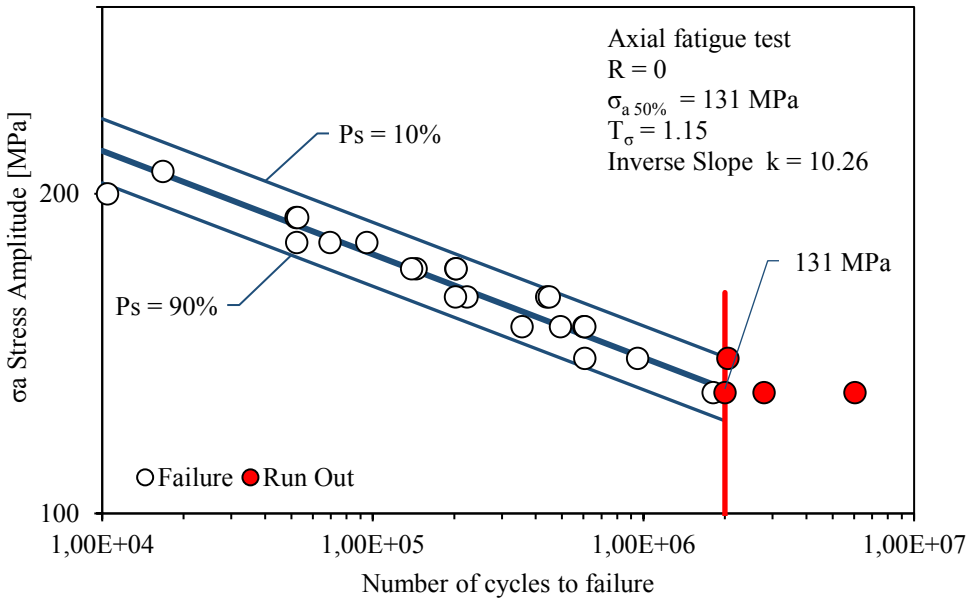

Figure 5.3. Fatigue life of specimens taken from 3.5Si-Sb casting.

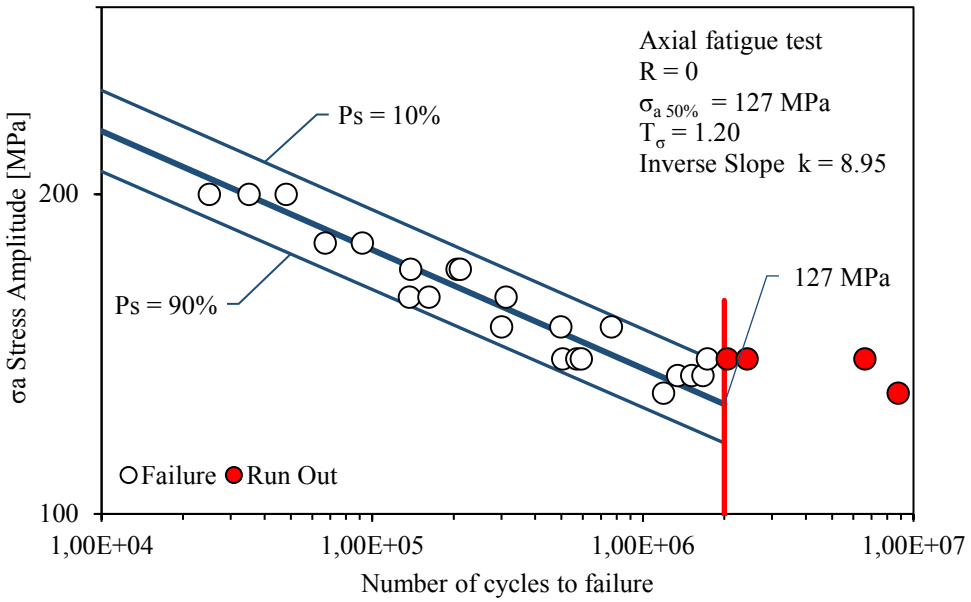

Figure 5.4. Fatigue life of specimens taken from 3.55Si casting.

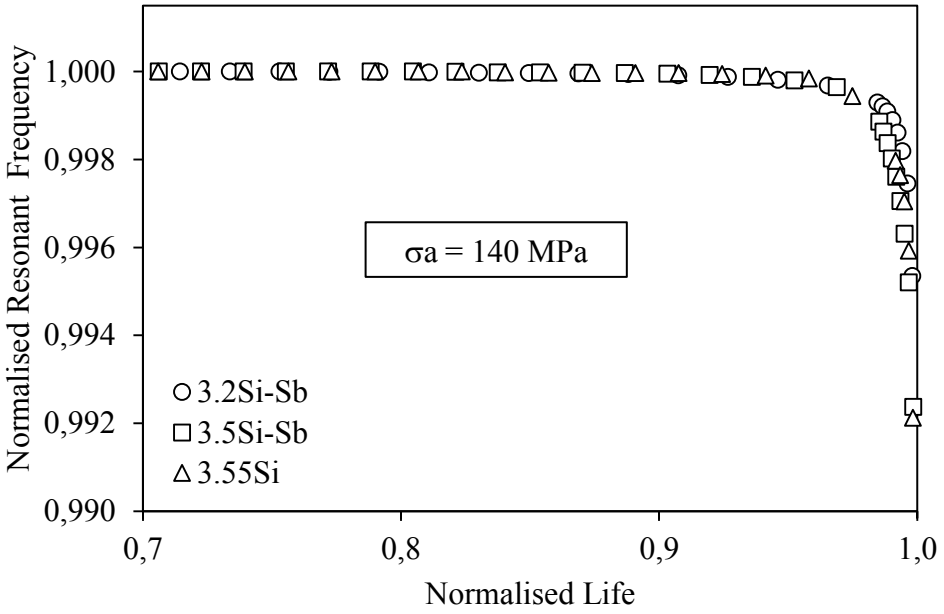

Figure 5.5. Normalised resonant frequency as a function of normalised fatigue life for the three analysed castings.

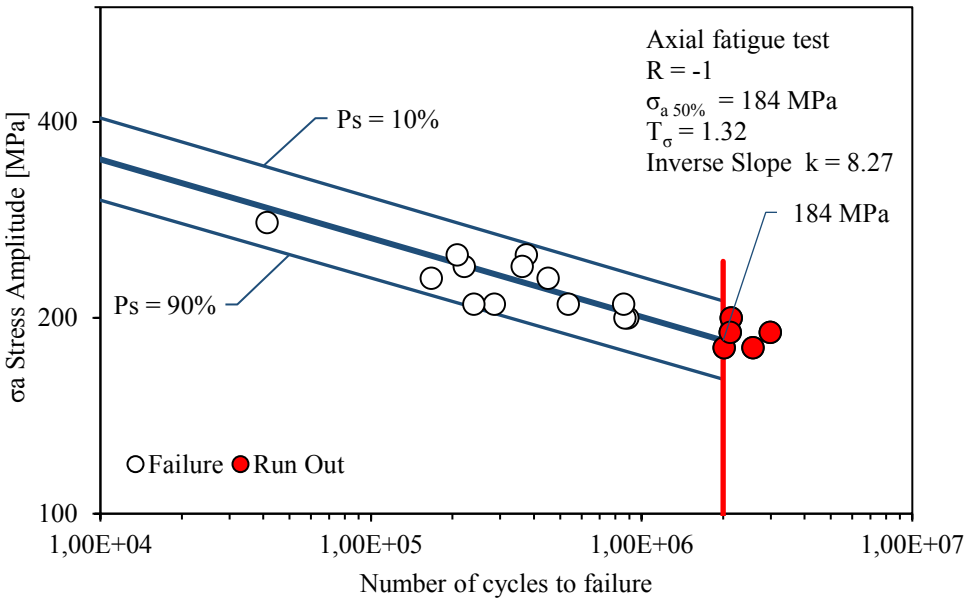

Figure 5.6. Fatigue life of specimens taken from 3.5Si-Sb ø300 casting under alternating axial pulsating loading conditions (R=-1).

5.5 Fractography

The fracture surfaces of broken specimens have been examined using a Scanning Electron Microscope in order to identify crack initiation (Figure 5.7a and b) and propagation zones (Figure 5.7c and d). All the samples showed shrinkage porosities, some of them of large dimensions, near the surface which have been identified as crack initiation points.

In order to estimate the maximum dimensions of the crack initiating defects, the projected surface, √area, of microshrinkage porosities that acted as crack initiators has been measured using an image analysis software, as shown in Figure 5.8.

Using the statistical analysis of extreme values, the $\sqrt{area}_{max}$ was estimated, for each casting, by considering the dimension of the defect corresponding to the upper bound of the 95% confidence interval of the √area distribution (Figure 5.9).

In Figure 5.10, the comparison of the distributions of initiating defects found in castings 3.2Si-Sb, 3.5Si-Sb and 3.55Si is shown.

The dimensions of the maximum initiating defect, $\sqrt{area}_{max}$, were found to be similar in size for all the three materials, with values of 1188, 1082 and 1212 μm, for 3.2Si-Sb, 3.5Si-Sb and 3.55Si, respectively.

The main differences have been found in the crack propagation stage. While, in the case of casting 3.2Si-Sb, the fatigue cracks propagate along the interface between the graphite nodules and the metal matrix, in the 3.5Si-Sb and 3.55Si specimens, the crack propagates easily through the areas with branched and interconnected degenerated graphite particles, slightly lowering the fatigue resistance. This phenomenon is also shown in Figures 5.11 and 5.12, where cross sectional views of the fracture surfaces show that fatigue crack passes around the graphite nodule while it propagates through the degenerated chunky graphite (CHG).

It can be observed that on the macro-scale the crack propagates in a direction perpendicular to the load axis, while, considering micro-scale, crack propagates changing its direction, due to the presence of graphite particles randomly distributed in the structure.

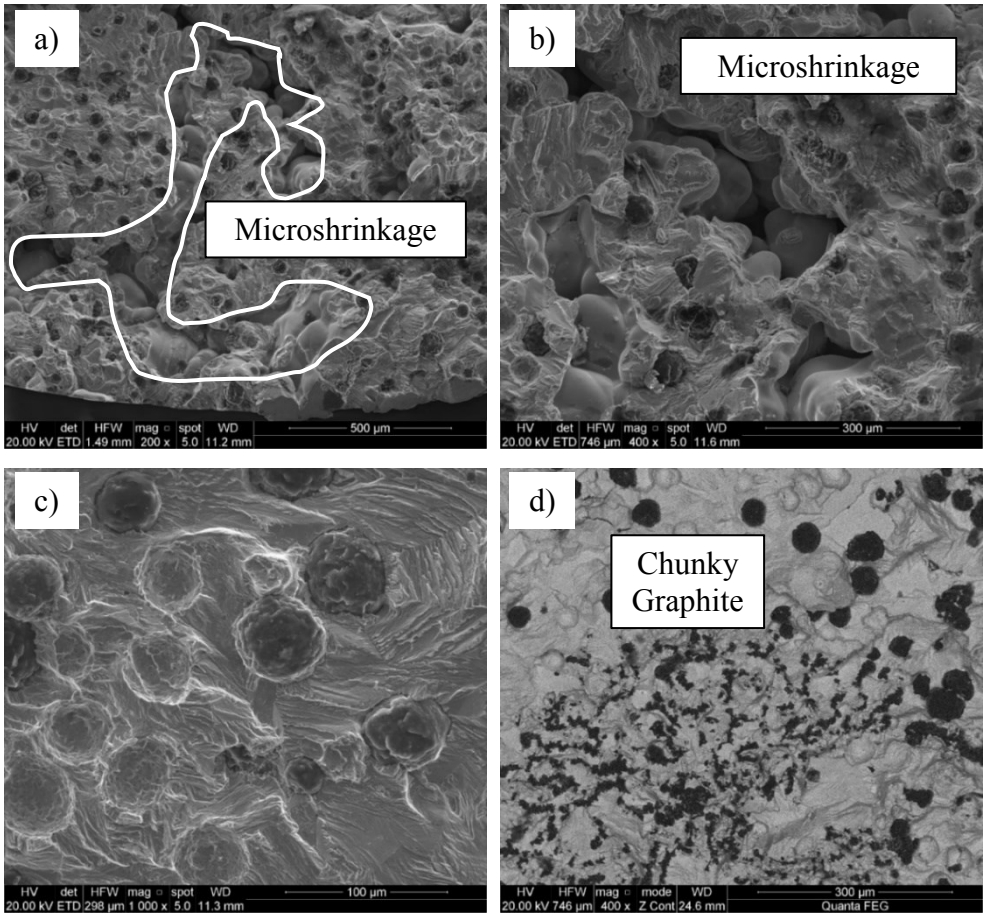

Figure 5.7. SEM micrographs of crack initiation, showing microshrinkage porosity (a,b), propagation zones in the presence of spheroidal graphite (c) and chunky graphite (d).

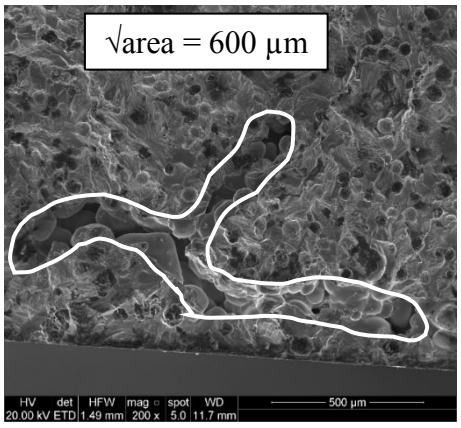

Figure 5.8. SEM image of fracture surfaces showing the dimensions (√area) of a microshrinkage porosity.

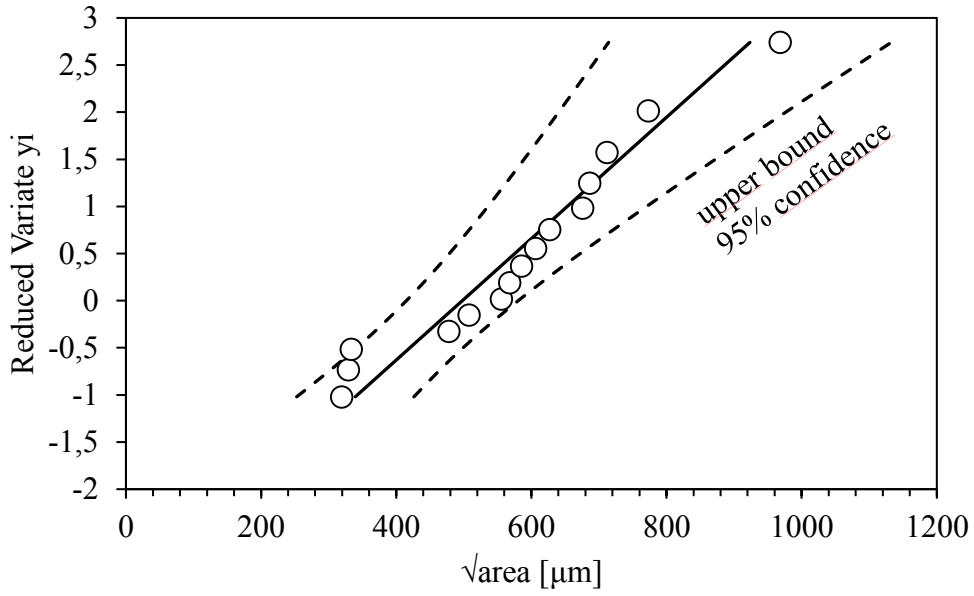

Figure 5.9. Extreme value distribution of initiating defects found in casting 3.2Si-Sb with 95% confidence interval.

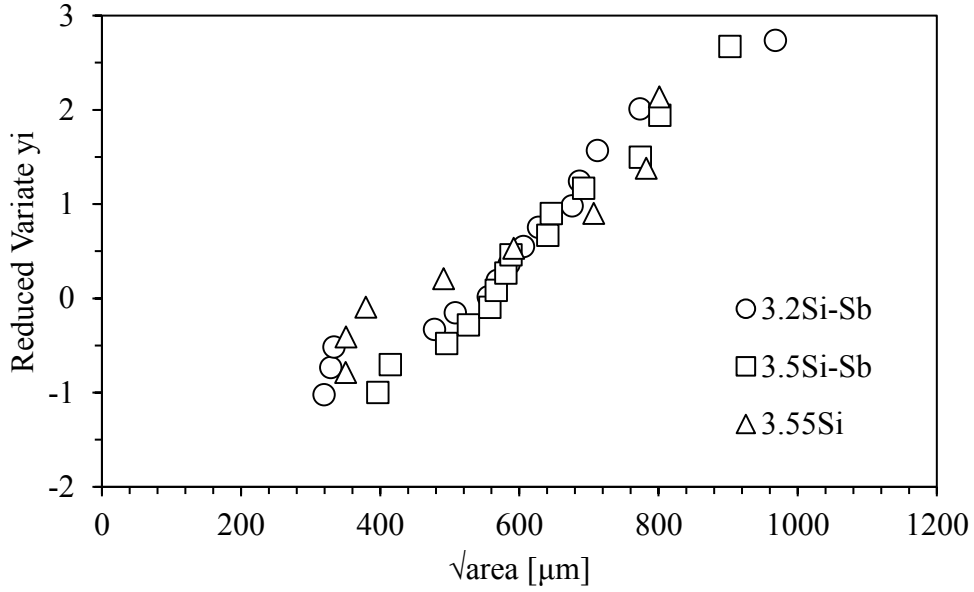

Figure 5.10. Comparison of the distribution of initiating defects found in casting 3.2Si-Sb, 3.5Si-Sb and 3.55Si.

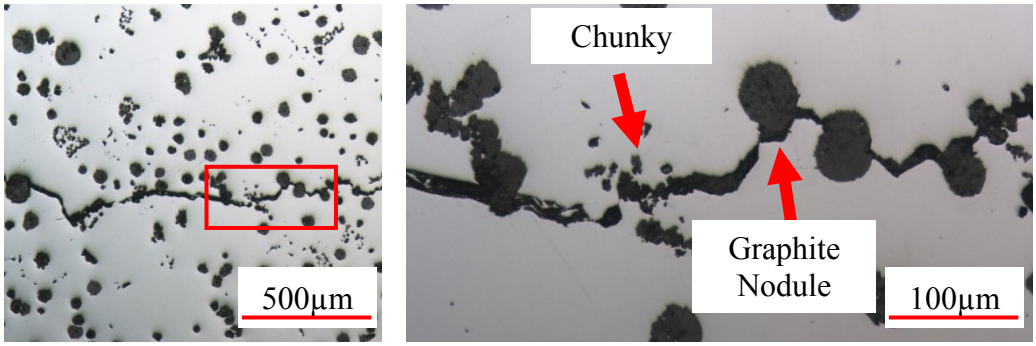

Figure 5.11. Cross sectional view of the fracture surface showing that fatigue crack passes around the graphite nodule along the graphite/matrix interface, while propagates through the chunky graphite (CHG), 3.5Si-Sb casting.

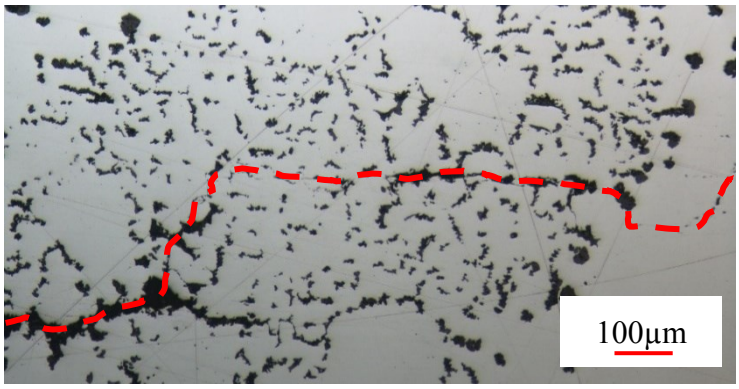

Figure 5.12. Micrograph showing that fatigue crack propagates through the chunky graphite particles (CHG), 3.55Si casting.

5.6 Comparison of fatigue strength with traditional ductile cast irons

Finally, the fatigue strength of solution strengthened ferritic ductile cast irons was compared with those of traditional ferritic and pearlitic grades with the same solidification conditions. As shown in Figure 5.13, the fatigue behaviours of pearlitic and SSF ductile irons were found to be very similar. For this reason, the data were considered all together in statistical analysis in order to evaluate the fatigue endurance and the scatter band index, which were found to be equal to 127 MPa and 1.2, respectively. It can be noted that all the results are located within a narrow scatter band, highlighting the fact that, when considering long solidification times and slow cooling rates, despite the difference in the microstructure, the SSF and the pearlitic DIs behave in a similar way, not only under static (Table 5.3), but also under dynamic loading conditions. In order to have a graphical comparison between the materials, the data of GJS 400-18 LT, due to the lower fatigue resistance, have been only superimposed to the Wöhler diagram.

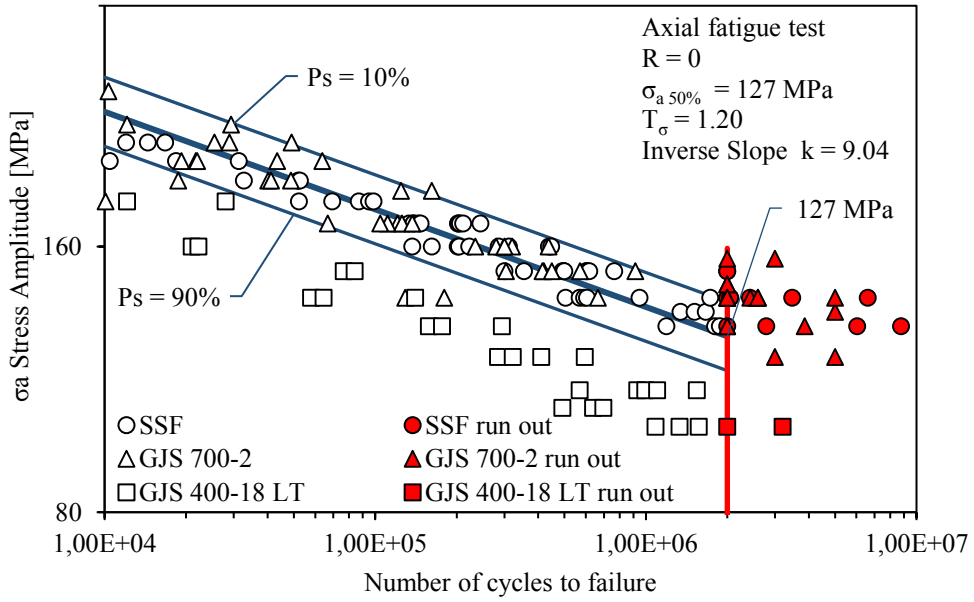

Figure 5.13. Fatigue life of specimens taken from pearlitic, ferritic and solution strengthened ferritic heavy section ductile cast iron castings.

5.7 Conclusions

In this chapter, the mechanical and fatigue properties of solution strengthened ferritic ductile cast irons characterized by long solidification times have been investigated. It has been confirmed that, increasing the Silicon content, the ultimate tensile strength and the yield stress increase, while the elongation at failure decreases. It has been also observed that the increased amount of Silicon could promote the formation of degenerated graphite particles (chunky graphite) in the thermal centre of the casings, with deleterious effect on the ultimate tensile strength and ductility. However, it was observed that the treatment with some ppm of Antimony is effective in counteracting the formation of such microstructural defect. It has been also found that, considering these long solidification times, SSF DIs are characterized by strength and fatigue resistance similar to those of pearlitic grades, while the ductility is comparable to the typical values of traditional ferritic grades. All the samples showed shrinkage porosities, which have been identified as crack initiation sites. Using analysis of extreme values, it was observed that the dimensions of the maximum initiating defect were similar in size for all the three materials. In the presence of chunky graphite, the crack propagates easily through the areas with branched and interconnected degenerated graphite particles, while propagates along the interface between the graphite nodules and the metal matrix in the case of spheroidal graphite.

6. *Solution strengthened ferritic ductile iron. Influence of different section thicknesses and solidification times.*

Highlights

Microstructural, mechanical and fatigue properties of solution strengthened ferritic ductile iron have been evaluated as a function of different section thicknesses and solidification times. Three types of cast samples with increasing thickness were produced in a green sand automatic moulding line. Microstructural analyses have been performed in order to evaluate the graphite nodules parameter and matrix structure. Tensile and fatigue tests have been carried out using specimens taken from specific zones, with increasing solidification time, inside each cast sample. Finally, the fatigue fracture surfaces have been observed using a scanning electron microscope.

The results showed that the wall thickness and, more importantly, the corresponding solidification time have a significant effect on the microstructure and mechanical properties of solution strengthened ferritic ductile iron.

6.1 Materials

In this chapter, a solid solution strengthened ferritic ductile iron with 3.25 wt% Si was investigated. The final chemical composition of the material is shown in Table 6.1. The carbon content has been chosen to be 3.3 wt%, in order to maintain a near eutectic composition, with the Equivalent Carbon calculated using the equation: $C_{eq} = C\% + 0.33(Si\% + P\%)$. With the aim to evaluate the effect of increasing solidification times on microstructural and mechanical properties, three different geometries, with increasing section thickness were produced in a green sand automatic moulding line. 15 moulds were produced, each of them containing cast samples with geometries taken from the UNI EN 1563:2012 standard. In particular, the round bar-shaped (type b), the Y-shaped type III and the Y-shaped type IV were used, the relevant wall thicknesses of which were 25, 50 and 75 mm respectively. In order to compute the solidification time within each cast sample, numerical analyses were carried out by using the code Novaflow & Solid®. The temperature dependent material properties for ductile iron and green sand have been taken from the database of the numerical code.

After the spheroidizing and inoculation process, and just before pouring the iron into the moulds, a metal sample was analysed by optical emission spectrometry to determine the chemical composition. At the same time, a standard cup for the thermal analysis, containing the same weight percentage of inoculant of the castings, was filled.

Table 6.1. Final chemical composition. (wt%).

C	Si	S	P	Mn	Mg	Ceq
3.31	3.25	0.008	0.025	0.13	0.050	4.40

6.2 Thermal analysis

By means of the thermal analysis technique, it is possible to determine some characteristic solidification temperatures, such as the liquidus temperature, the minimum and maximum eutectic temperature, the temperature at the end of solidification. Moreover, the solid-state transformation can be studied using this technique.

The cooling curve of the SSF-DI obtained from the standard cup and the first time derivative are shown in Figure 6.1. From a global point of view, two plateaus during the eutectic and the solid-state transformation can be observed.

The typical cooling curves of traditional ferritic (GJS 400-18) and pearlitic (GJS 700-2) ductile irons (about 2.6 wt% Si) are also reported in Figures 6.2 and 6.3.

From the comparison between the curves of the three different materials during the eutectic and the eutectoid transformation (Figures 6.4 and 6.5, respectively), it is visible that there are little variations in the solidification behaviour, while the main difference is related to the solid-state transformation.

As reported in literature the different chemical compositions of the alloys promote the formation of pearlitic and/or ferritic matrix, with differences on the eutectoid temperature and on the cooling rate. In particular, the cooling curve of the GJS 700-2 showed an arrest and a recalescence that is associated to the pearlite formation, while in the case of GJS 400-18, the ferritic matrix leads to a higher eutectoid temperature. Moreover, because of the low released latent heat, a thermal arrest does not occur during the ferrite formation.

Finally, due to the higher silicon content, the eutectoid temperature of the solution strengthened ductile iron is increased with respect to the traditional ferritic grade.

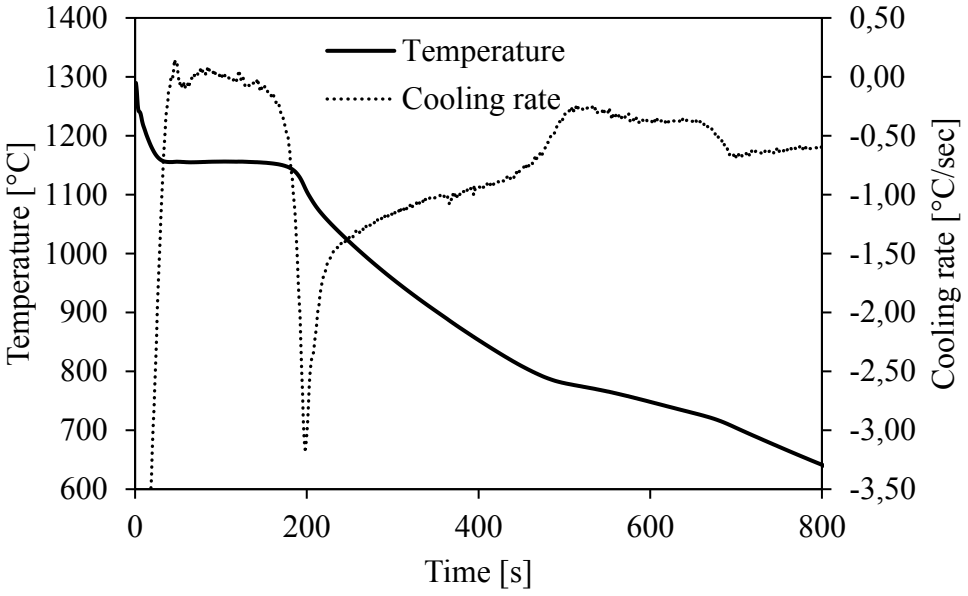

Figure 6.1. Cooling curve (solid line) and its first derivative (dotted line) of the solution strengthened ferritic ductile iron of the present work.

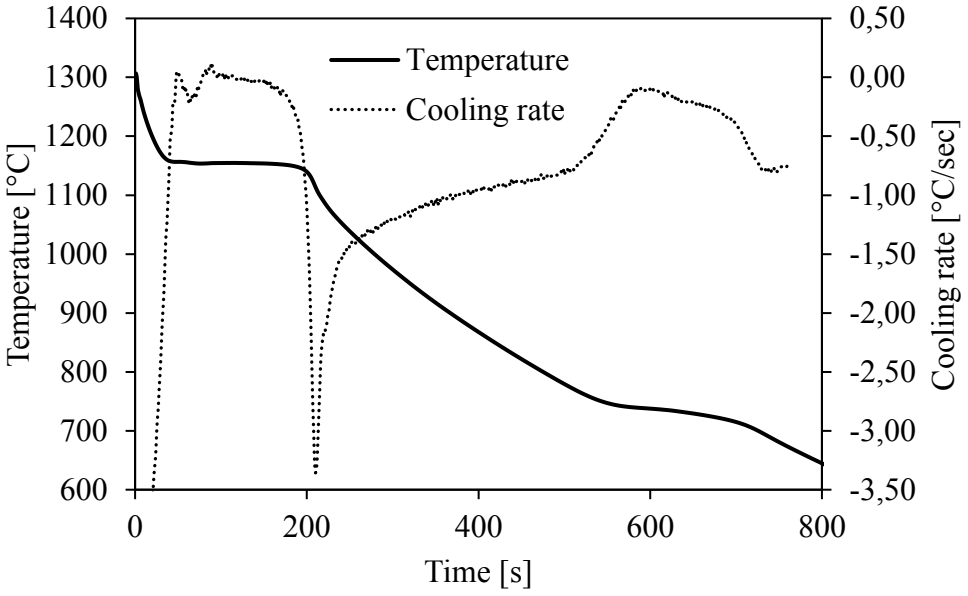

Figure 6.2. Cooling curve (solid line) and its first derivative (dotted line) of a traditional ferritic ductile iron (GJS 400-18).

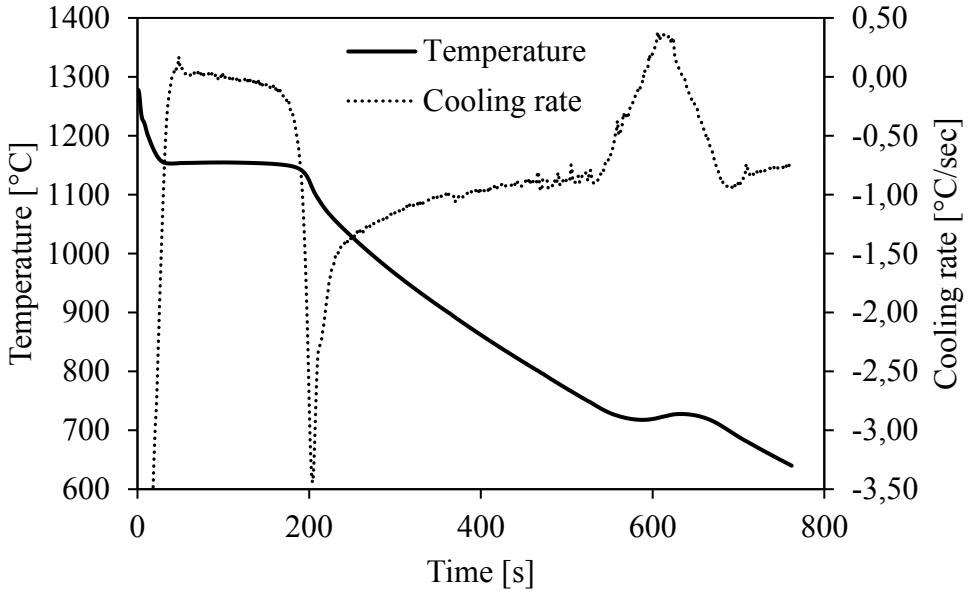

Figure 6.3. Cooling curve (solid line) and its first derivative (dotted line) of a traditional pearlitic ductile iron (GJS 700-2).

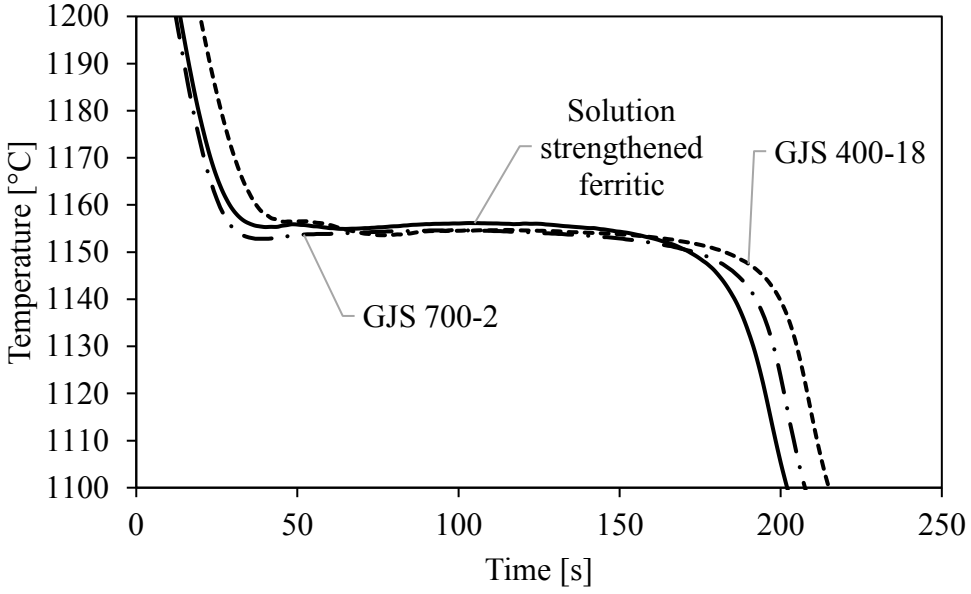

Figure 6.4. Comparison of temperature profile during the eutectic transformation between traditional and solution strengthened ferritic ductile iron.

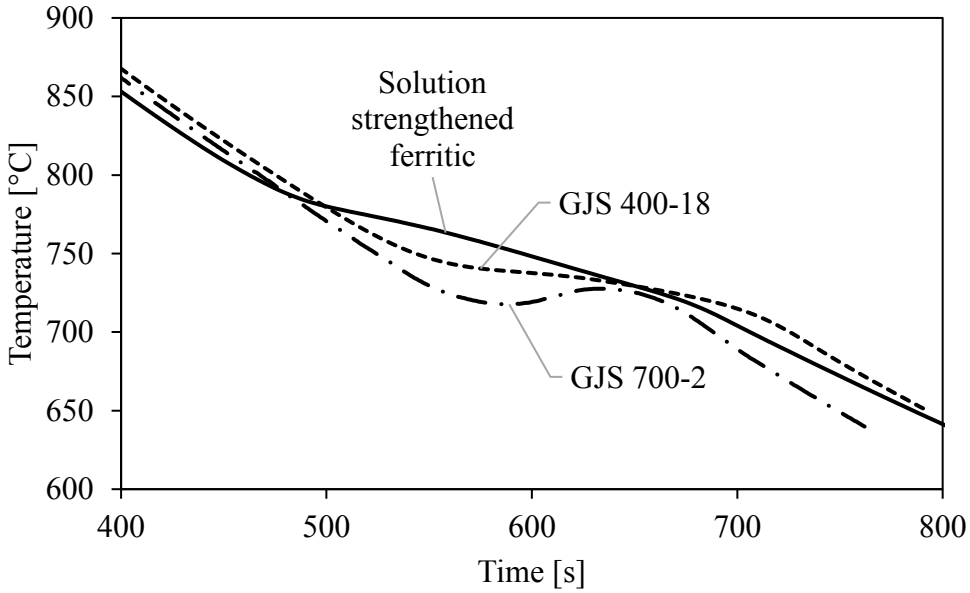

Figure 6.5. Comparison of temperature profile during the solid-state transformation between traditional and solution strengthened ferritic ductile iron.

6.3 Tensile test

In order to evaluate the influence of increasing solidification time on the mechanical properties, specimens were taken from the three different cast samples (Figure 2.3). In particular, in the case of round bar shaped samples with a diameter of 25 mm, the tensile specimens were directly machined. Differently, in the case of Y-shaped samples, a block of about 25x25x175 mm^3 was cut before the final machining. The positions where the specimens were taken from are shown in Figure 6.6; it can be noted that from each type IV sample, two specimens were obtained. Five specimens for each condition have been tested. Table 6.2, summarises the results obtained as a function of section thickness and corresponding solidification time, obtained from the numerical analysis. First of all, it is important to highlight the fact that, through the solid solution strengthening made by Silicon, it is possible to reach both high strength and ductility. As expected, increasing the section thickness and the solidification time, the mechanical properties decrease. This is visible not only between specimens taken from the three different kind of cast samples, but also from different positions within the same sample. It is also important to note that, thanks to the solution strengthening mechanisms, the mechanical properties are less influenced by the wall thickness than the traditional ferritic/pearlitic ductile irons.

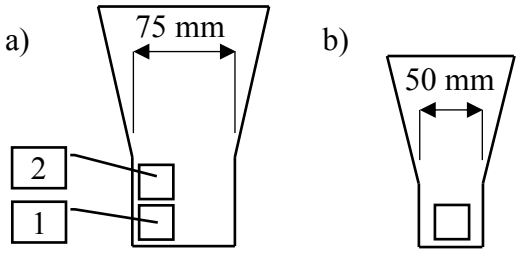

Figure 6.6. Position of tensile specimens taken from the Y-shaped type IV (a) and type III (b).

Table 6.2. Tensile test results of specimens taken from cast samples as a function of section thickness and corresponding solidification time.

Cast sample	Thickness [mm]	Solidification time [min]	σ_{UTS} [MPa]	$\sigma_{y\ 0.2\%}$ [MPa]	ε_R %
Round bar shaped type b	25	2.5	507	395	19.8
Y-shaped type III	50	9.8	492	389	17.1
Y-shaped type IV (1)	75	16.2	487	386	17.2
Y-shaped type IV (2)	75	22.1	468	375	13.0

6.4 Fatigue test

Fatigue tests have been performed using a resonant testing machine (Rumul Testronic 150kN), by applying a sinusoidal tensile pulsating load at the frequency of about 130 Hz and nominal load ratio R=0. Tests have been stopped at the total separation of the two parts of the specimens, or after reaching $1 \cdot 10^7$ cycles. The staircase method was carried out with an applied stress increment of 10 MPa in order to evaluate the fatigue strength corresponding to a fatigue life of 10 million cycles. Plain specimens were taken from Y-shaped type III and IV cast samples. In particular for each sample, specimens were taken from three levels, numbered consecutively from 1 to 3 going towards the thermal centre of the casting, as shown in Figure 6.7. In the case of type IV sample, six specimens have been obtained, while, due to the smaller dimension, it was possible to take only three specimens from each type III sample. The relationship between position within the cast sample and the calculated solidification time is shown in Table 6.3.

The results of fatigue tests have been statistically analysed by using a method that allows to estimate the full S-N curve by considering both the finite life and the run out specimens according to ISO 12107:2012 standard. It is assumed that the finite fatigue life regime consists of an inclined straight line in a logarithm scale with data following a log-normal distribution, while the fatigue endurance region is represented by a horizontal line. In order to have a graphical comparison of the fatigue behaviour, the specimens taken from the different zones within the cast samples are represented with different symbols in Figure 6.8. Firstly, the statistical analysis of fatigue data has been performed considering all together the specimens taken from the same cast sample geometry. In particular it can be observed in Table 6.4 that, by increasing the section thickness of the casting (going from 50 mm to 75 mm) the fatigue strength corresponding to 50% survival probability is lowered of about 7 MPa while the scatter index T_σ, defined as the ratio between the stress amplitude at 10% and 90% survival probability, increases. Moreover, it can be observed from the graph in Figure 6.8 that the specimens taken from the position number 1 of the type IV cast samples, behave in a similar manner to those obtained from the Y III samples.

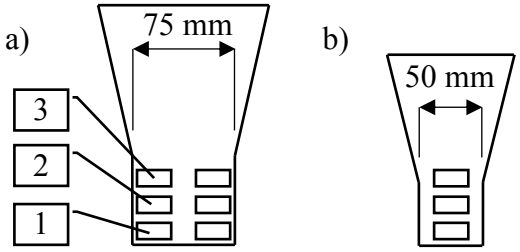

Figure 6.7. Position of fatigue specimens taken from the Y-shaped type IV (a) and type III (b).

Table 6.3. Solidification times in the positions shown in Figure 6.7 obtained from the numerical analysis.

Position	Y-shaped type III	Y-shaped type IV
1	8.5 min	14.5 min
2	11.3 min	18.1 min
3	14.5 min	22.1 min

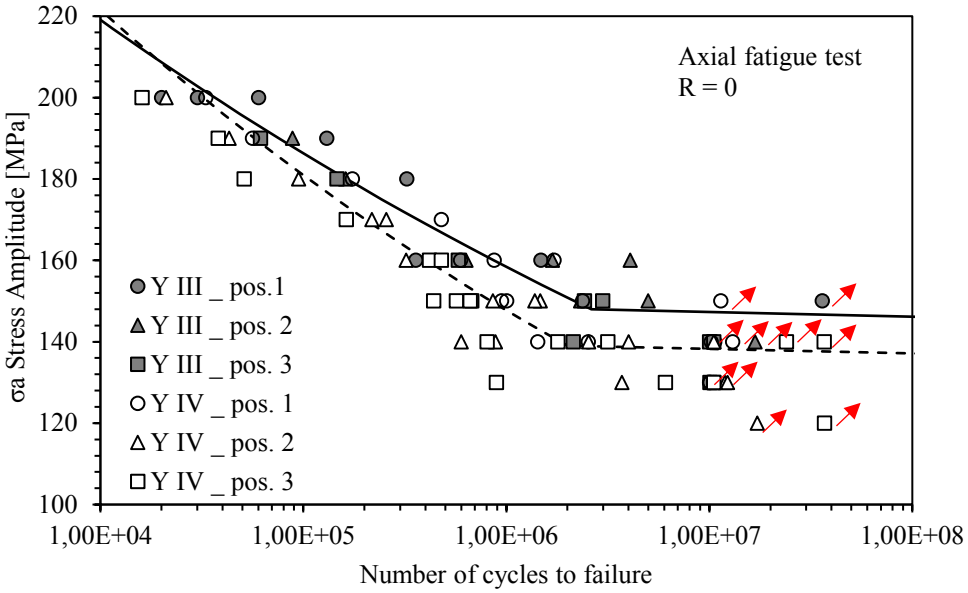

Figure 6.8. Fatigue life of specimens taken from different position within the cast samples. Solid line and dotted line represent the estimated fatigue curves at 50% survival probability for Y-shaped type III and type IV cast samples respectively. Run out specimens marked with an arrow.

Table 6.4. Fatigue strength at 50% survival probability and scatter index at $1 \cdot 10^7$ cycles considering cast samples thickness.

Cast sample	Thickness [mm]	σ_a [MPa]	T_σ
Y-shaped type III	50	145	1.13
Y-shaped type IV	75	138	1.30

In order to better understand the fatigue behaviour of the castings, data have been re-analysed considering no more the thickness, but the solidification time. In particular, three time ranges have been defined based on the numerical simulation results shown in Table 6.3. Under these conditions, samples taken from position number 3 of the type III sample and from position 1 of the type IV sample, which fell within the same solidification time range, have been analysed together.

The obtained fatigue curves at 50% survival probability are shown in Figure 6.9, while the estimated fatigue strength and the scatter index are reported in Table 6.5 for each range.

It is important to note that, taking into account the solidification times, it is possible to obtain a more accurate fatigue life estimation in the different positions within the castings, with reduced scatter index compared to the results achieved by considering only the section thickness. This is because the statistical analyses were carried out by taking into account specimens with similar cooling conditions, which lead to reduced variability in the mechanical properties.

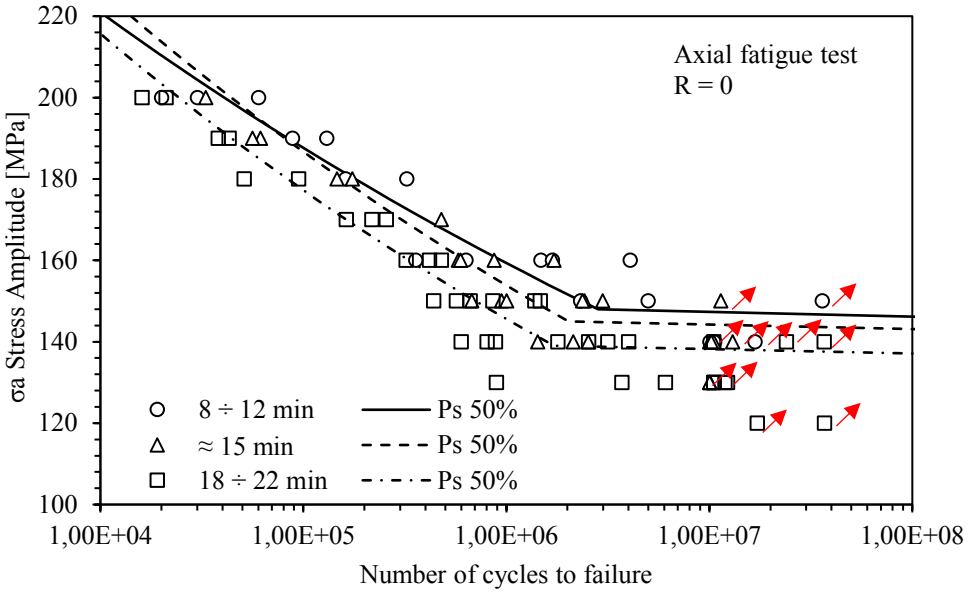

Figure 6.9. Fatigue life of specimens as a function of solidification time. Lines represent the estimated 50% survival probability curve in the defined solidification time ranges. Run out specimens marked with an arrow.

Table 6.5. Fatigue strength at 50% survival probability and scatter index at $1 \cdot 10^7$ cycles considering solidification time range.

Solidification time	σ_a [MPa]	T_σ
8 ÷ 12 min	147	1.10
≈ 15 min	143	1.23
18 ÷ 22 min	136	1.25

6.5 Microstructure and Fractography

Microstructural parameters have been evaluated in a section of broken and unbroken fatigue specimens, using an optical microscope connected to an image analysis software. Nodule count, nodule size and nodularity have been calculated according to ASTM E2567-11 using unetched polished samples and a 100x magnification. Subsequently, samples have been etched with Nital 5% in order to reveal the fully ferritic matrix structure. A summary of the microstructural properties is presented in Table 6.6. It can be observed that the solidification time influences the microstructure of the alloys; in particular, it was confirmed that decreasing the cooling rate, fewer nodules are formed with gradually increasing dimensions and lower nodularity. Specimens taken from different cast samples but with the same cooling conditions are characterized by similar microstructural parameters, such as nodule count and nodule diameter. Examples of micrographs are shown in Figures 6.10 and 6.11.

The increasing in the solidification time could promote also the formation of microstructural defects such as microshrinkage porosities, segregation or degenerated graphite particles. In fact, going toward the centre of the cast samples, it has been found an increasing amount of areas containing branched and interconnected graphite particles, classified as chunky graphite (Figures 6.11b-f). The treatment of the alloy with Antimony would have avoided the formation of degenerated graphite, but it could have led to the formation of pearlite on the thinner sections, with associated lower ductility and higher hardness. Moreover, in the longer to solidify zones, microshrinkage cavities and small area of pearlite, due to segregation of carbide promoter or pearlitizing elements, have been found (Figure 6.11f).

The microstructural properties confirmed what observed during the mechanical tests. Higher nodule count and nodularity implies greater resistance and ductility. The presence of microstructural defects could be related to the lower mechanical properties and higher fatigue scatter index of specimens taken from longer to solidify zones.

The analyses of fracture surfaces of some fatigue broken specimens revealed that the failure initiated at microshrinkage porosities located near the free surface of the specimens (Figures 6.12a and b). It has been also observed that the chunky graphite is a preferential path for the crack propagation, compared to areas containing spheroidal nodules. In fact, the amount of chunky graphite on the fracture surface is higher than the content found on polished sections. It was also found that the failure seems to happen in different ways. Most of the fracture surface showed a ductile dimple fracture with microvoids coalescence (Figures 6.12c and d), however, some areas with brittle transgranular cleavage and intergranular fracture have been even detected (Figure 6.12e).

Table 6.6. Microstructural properties of samples. Mean values and standard deviation (in brackets).

Cast sample	Position	Nodule Count [Nodules/mm^2]	Mean Nodule diameter [μm]	Nodularity
Round bar	-	304	19 (5.5)	93%
Y III	1	115	29 (9)	85%
	2	98	30 (11)	80%
	3	90	28 (10)	77%
Y IV	1	95	29 (9.5)	82%
	2	84	31 (11)	76%
	3	63	33 (13)	70%

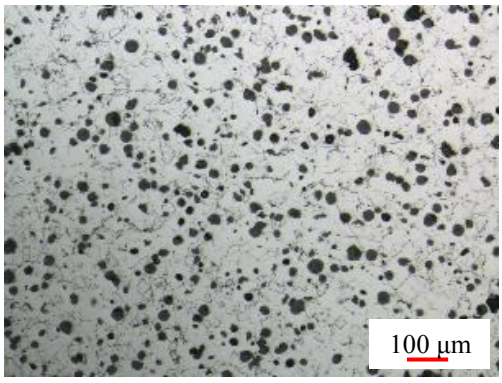

Figure 6.10. Micrograph of specimen taken from round bar shaped cast sample, etched with Nital 5%.

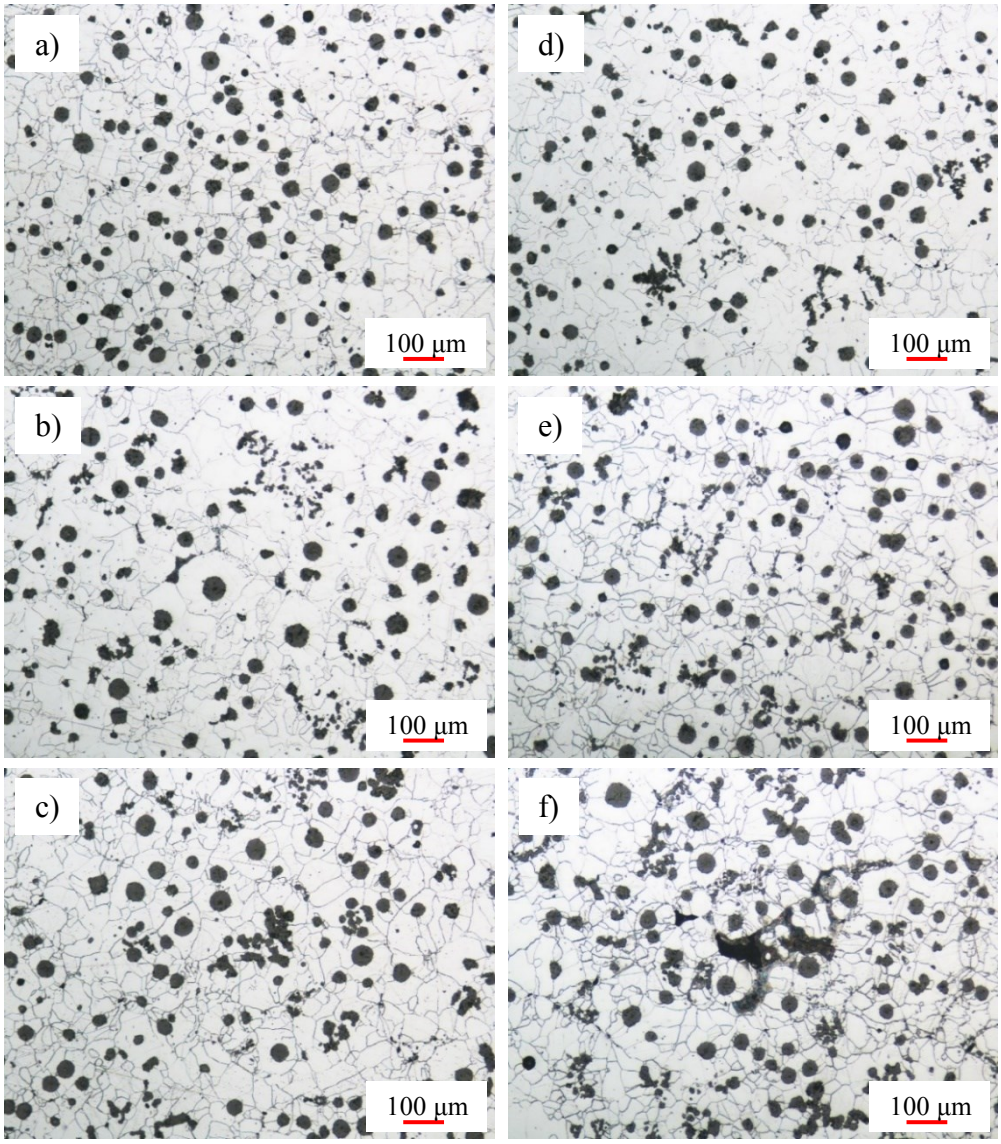

Figure 6.11. Micrographs of specimens taken from type III cast sample, position 1 (a), 2 (b) and 3 (c) and type IV cast sample, position 1 (d), 2 (e) and 3 (f).

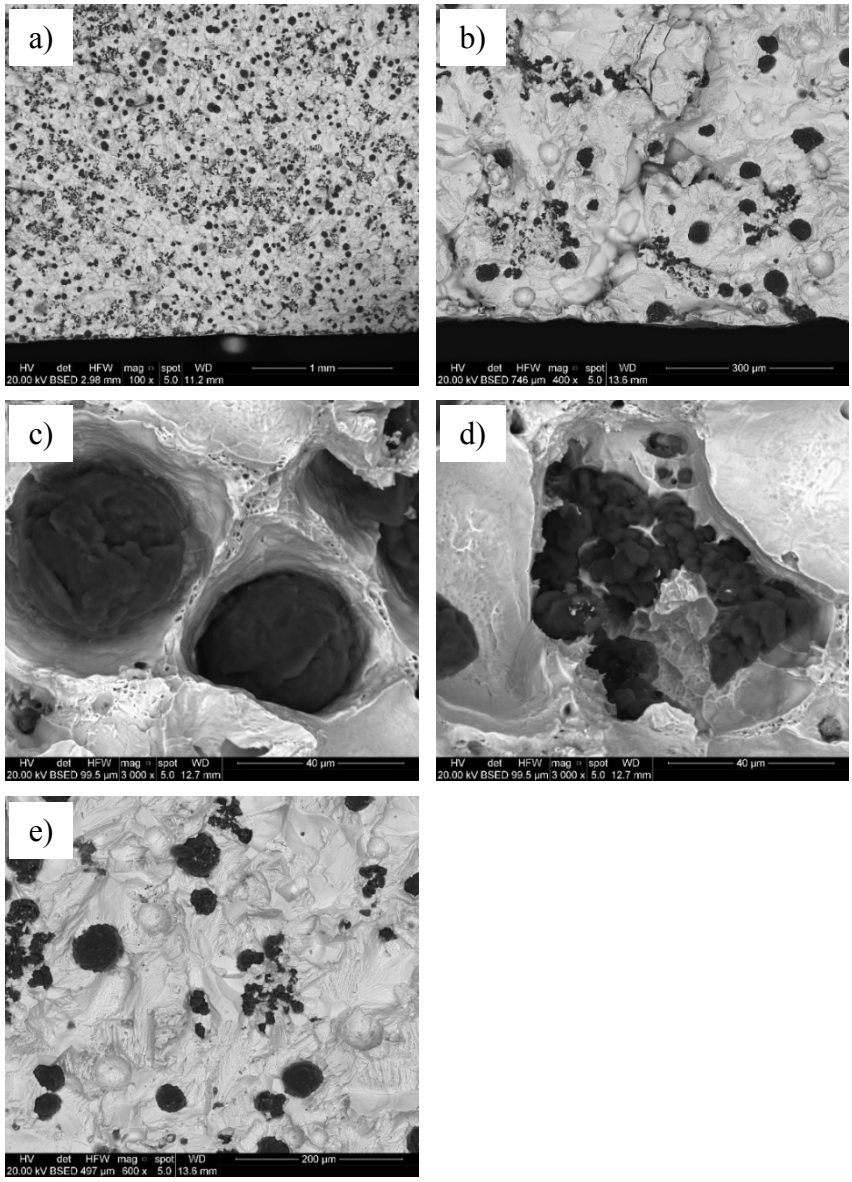

Figure 6.12. SEM images of fracture surfaces showing a panoramic overview of the crack initiation and propagation zone (a) and a particular of the crack initiating defect (microshrinkage porosity) (b); dimple fracture with microvoids coalescence in the presence of spheroidal graphite nodules (c) and degenerated graphite particles (d); image of the coexistence of brittle transgranular cleavage and intergranular fracture (e).

6.6 Comparison of fatigue strength of SSF ductile irons obtained from different cooling conditions

Finally, the current fatigue results have been compared to those obtained considering solution strengthened ductile irons characterized by solidification time of more than 2.5 hours (see previous chapter).

As shown in Figure 6.13, it can be observed that the cooling conditions play an important role in influencing the fatigue behaviour of the alloys. In particular, it is confirmed that, increasing the solidification times, going from about 10 minutes to several hours, the fatigue endurance decreases, with values of the fatigue stress amplitude at a survival probability of 50%, which goes from approximately 150 MPa to values close to 125 MPa.

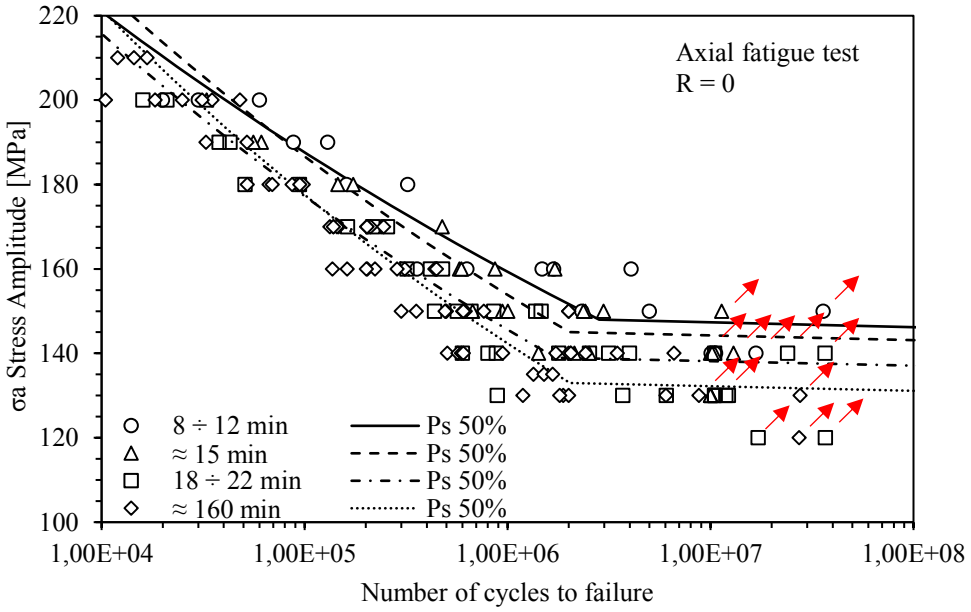

Figure 6.13. Comparison of fatigue life of solution strengthened ferritic ductile irons characterized by increasing solidification times.

6.7 Conclusions

In this chapter, the microstructural, mechanical and fatigue properties of a solution strengthened ferritic ductile cast iron characterized by different solidification times have been investigated. It has been confirmed that low cooling rates affect the strength and the ductility of the castings. Due to the high amount of silicon, the microstructure exhibits a fully ferritic matrix, with only small areas of pearlite, due to segregation of undesired elements, in the thicker sections. Moving toward the zone that takes longer to solidify, the number of graphite nodules decreases and an increasing amount of degenerated chunky graphite is found. The fatigue behaviour has been evaluated using specimens taken from different zones inside the castings within defined solidification time ranges. It was confirmed that a better estimation of the fatigue life is achievable by considering the solidification times rather than the section thickness. A decrease of the fatigue strength and an increase of the scatter index were observed with increasing the solidification times.

All the samples showed shrinkage porosities, which have been identified as crack initiation sites. The fracture surface revealed that the crack propagates easier through the areas with chunky graphite compared to areas with spheroidal graphite nodules. Most of the fracture surface showed a ductile dimple fracture with microvoids coalescence, but some areas with brittle transgranular cleavage and intergranular fracture were also detected.

7. *Novel method for the fatigue strength assessment of heavy sections made by ductile cast iron in presence of solidification defects.*

Borsato, T., Ferro, P., Berto, F., 2018. Novel method for the fatigue strength assessment of heavy sections made by ductile cast iron in presence of solidification defects. Fatigue Fract. Eng. Mater. Struct. 41, 1746-1757.

Highlights

The fatigue strength of ferritic, pearlitic and solution strengthened ferritic ductile irons taken from heavy sections and characterized by long solidification times has been assessed. Starting from the idea of Murakami and co-workers, a new model for the prediction of the fatigue strength is proposed. It allows a sound fatigue assessment of the fatigue strength of as-cast ductile irons containing solidification defects, such as low nodule count, exploded, chunky and spiky graphite or microshrinkage porosities. The new developed equation validated by means of an extensive benchmarking with data taken from the literature has shown a very high potential for applications to thick walled components.

7.1 Introduction

Over the last years, the production of heavy section ductile cast iron components with structural functions increased thanks to the relatively low manufacturing cost, excellent castability and good combination of mechanical properties. Examples of the use of these materials are windmill parts, automotive and agricultural parts, big engine blocks, parts of hydraulic presses.

The typical microstructure of ductile cast irons is characterized by spheroidal graphite particles dispersed within a metal matrix that can be, depending on the chemical composition of the alloy, ferritic, pearlitic or ferritic/pearlitic. It is well known that the ferritic matrix gives higher ductility and toughness, while the pearlitic one is characterized by a higher strength. Recently, ductile irons with ferritic matrix strengthened by solid solution through the addition of balanced amount of silicon have been introduced in the standard UNI EN 1563[1]. The new types of materials are characterized by a good combination of strength and ductility and a high ratio between yield stress and ultimate tensile stress.

By increasing the thickness of the components, the solidification times will increase with the increased risk of finding coarse grains and anomalous structures [2]. In particular, the nodularity and the nodule count will decrease, while the dimensions of graphite particles will increase. Furthermore, the greater the casting dimensions, the greater the probability of finding degenerated graphite (exploded, chunky or spiky), large microshrinkage porosities, non-metallic inclusions or undesired segregations [3,4]. These defects, which negatively affect the mechanical properties of the materials, can be avoided only partially through the optimization of the production process (casting temperature, spheroidization or inoculation process, addition of balanced amount of elements (Sb, Bi, Ce, etc.)) [5–7]. Consequently, in thick walled components, some defects are unavoidable.

In many works found in literature [8–12], various types of solidification defects have been studied, in order to evaluate their influence on the static and fatigue resistance of the components. The ultimate tensile strength and the elongation at failure are lowered by solidification defects, while hardness and yield stress are less affected. Moreover, it was found that the more the graphite deviates from the spheroidal shape, the lower is the strength and the ductility. Finally, it was

demonstrated that defects are preferential crack initiation sites during fatigue loadings.

Canzar [13] showed experimentally that size, shape and distribution of the graphite nodules play a major role in the crack initiation and propagation process. It was also shown that the largest irregularly shaped nodules reduce the fracture toughness and the fatigue strength.

Iacoviello et al. [14–20] studied the influence of microstructure on the fatigue crack propagation resistance of different types of ductile cast iron with various matrix structure. They found that graphite particles do not only act as crack arresters but, depending on matrix microstructure, they can also increase the fatigue crack propagation resistance by means of an increase of the crack closure effect.

Nadot et al. [21,22] observed that crack initiation point is a single microporosity in proximity of the specimen surface. They also found that in uniaxial fatigue tests, the fatigue limit is much more sensitive to surface defects than internal defects. These results were confirmed in other works [23,24] where it was observed that microshrinkage cavities strongly influence the fatigue behaviour of ductile cast irons.

In the literature [25–30] several fatigue tests have been performed on specimens taken from different zones within a wind turbine component. It has been found that crack initiation is influenced above all by microshrinkage porosities while crack propagation is influenced by the microstructure.

Some researchers investigated the effect of chunky graphite on the mechanical and fatigue properties of heavy section ferritic ductile cast irons [31–33]. They found that this type of degenerated graphite morphology negatively affects the mechanical properties of the material; in particular it reduces the ultimate tensile strength and mostly the elongation to failure, without affecting the yield strength and the hardness. Moreover, it was found that also the fatigue strength is lowered by the presence of chunky graphite; while the graphite spheroids act as crack arresters, in the presence of chunky graphite, the cracks passes easily through the branched and interconnected graphite particles, lowering the fatigue strength of the material. Similar conclusions have been achieved when solution strengthened ferritic ductile cast irons have been investigated [34].

In other works [35,36], it was observed that microshrinkage cavities, near the surface of the specimens, were the cause of the fatigue failure of heavy section pearlitic ductile iron castings. It was also shown that a combined effect between microshrinkage and degenerated graphite (spiky) could exist when they are both present in the alloy.

One of the most used method for the estimation of the fatigue strength of specimens containing defects is the criterion proposed by Murakami and Endo [37,38]. According to this model, the fatigue limit of materials containing small defects can be evaluated by using an equation that takes into account a material parameter and a defect parameter.

Starting from the relationship $\Delta K_{th} \propto \sqrt{area}^{1/3}$, the fatigue resistance (σ_a) was proposed to have the following expression:

$$\sigma_a = F_{loc} \frac{(HV + 120)}{\sqrt{area}^{1/6}} \left(\frac{1-R}{2}\right)^{\alpha} \quad (1)$$

In Eq. (1) HV is the Vickers Hardness of the matrix and √area is a parameter representative of the material defects and cracks. √area is defined as the square root of the area obtained by projecting small defect or crack onto a plane perpendicular to the maximum principal stress. F_{loc} is a parameter that takes into account the position of the defects in the specimens. It is equal to 1.43 for a surface defect, 1.41 for a defect just below the surface and 1.56 for an interior defect. R is the load ratio, and α is a material parameter that can be calculated by using the following equation [38] (for steels): $\alpha = 0.226 + HV \cdot 10^{-4}$. In the case of ductile cast irons [39], α has been defined as $\alpha = 0.371 + HV \cdot 10^{-4}$.

It was found that the largest defect, such as the maximum size of graphite particle, artificial notches, or casting defect (e.g., micro-shrinkage cavity) play a dominant role in determining fatigue strength of ductile cast irons [39–43]. It was also found that the fatigue limit is not a limit stress for nucleation but rather the threshold stress for non-propagation of a small crack emanating from a graphite particle or defect. For this reason, small defects are similar to cracks.

Deguchi et al. [44,45] investigated the effects of artificial small defects on the ferritic/pearlitic ductile cast irons. They observed that, in the case of two phases matrix, the measurement of the correct Vickers hardness of the matrix is quite

difficult. It follows that the previous equation (Eq. 1) could not be used in order to evaluate the fatigue resistance of ferritic/pearlitic ductile irons. In this case, the following new expression has been proposed:

$$\sigma_a = F_{loc} \frac{(0.34\ \sigma_{UTS} + 170)}{\sqrt{area}^{1/6}} \left(\frac{1-R}{2}\right)^{\alpha} \qquad (2)$$

Where the ultimate tensile strength σ_{UTS} is used as material parameter. √area is the dimension of the artificial defect, which is not related to the solidification conditions, microstructure and mechanical properties of the material. Two values of α parameter were found: 0.557 (by using circumferential notched specimens [46]) and 0.476 (by using specimens with drilled holes [47]). Moreover, the fatigue strength of smooth specimens was described by using the following expression:

$$\sigma_a = 0.25\ \sigma_{UTS} + 110 \qquad (3)$$

It was also observed that exists a minimum critical size of the defect below which the fatigue strength is not affected. The concept of a minimum critical size of defect, below which the fatigue strength is not affected, has been extensively discussed by Atzori and Lazzarin [48].

It is important to observe that the proposed methods consider as-cast ductile irons with artificial defects (notches or holes) that have been intentionally machined on the specimens; really, they are not intrinsic material defects. As described above, with increasing the dimensions of the castings, the solidification time increases with a much higher probability of finding solidification defects of larger dimensions. Consequently, the casting defects are intrinsically linked with the matrix microstructure arising from the solidification.

In this study, the fatigue resistance of ferritic, pearlitic and solution strengthened ferritic ductile irons, characterized by long solidification times has been assessed. It is proposed a new model, based on the √area parameter, for the prediction of the fatigue resistance of as-cast ductile irons containing solidification defects, such as low nodule count, exploded, chunky and spiky graphite or microshrinkage porosities. It takes into account the strong linking between solidification microstructure and fatigue resistance lowering defects.

7.2 Materials

Different grades of ductile irons have been considered in the analysis; traditional ferritic (GJS 400-18), pearlitic (GJS 700-2) and new generation solution strengthened ferritic ductile irons (SSF DI) with silicon contents greater than 3.2wt%. Castings with various solidification times have been analysed (Table 7.1).

Table 7.1. Dimensions and chemical composition of the analysed castings.

Material	Casting code	Dimensions [mm]	C	Si	Mn	Cu	Mg
GJS 700-2 Pearlitic	P-A	300x300x250	3.65	1.95	0.30	1.25	0.059
	P-B	300x300x250	3.75	2.25	0.30	1.20	0.063
	P-E	300x300x250	3.58	2.50	0.36	1.12	0.054
	P-C	600x600x600	3.70	1.94	0.31	1.18	0.068
GJS 400-18 LT Ferritic	F-F	300x300x250	3.79	2.06	0.22	0.07	0.064
GJS 400-18 Ferritic [32]	F-Chunky	cast ø650	3.50	2.45	0.12	0.13	0.055
	F-Good	cast ø650	3.50	2.45	0.12	0.13	0.055
SSF DI Solution strengthened ferritic	S-D	300x300x250	3.18	3.22	0.19	0.25	0.043
	S-G	300x300x250	3.14	3.50	0.19	0.10	0.058
	S-H	300x300x250	3.10	3.55	0.19	0.10	0.060
	S-I	ø 300 H520	3.30	3.19	0.20	0.16	0.047
	S-Y III	Y-shape (50)	3.31	3.25	0.13	0.16	0.050
	S-Y IV	Y-shape (75)	3.31	3.25	0.13	0.16	0.050

7.3 Summary of Results

The mechanical properties of specimens taken from the castings are collected in Table 7.2. It can be observed that, considering pearlitic GJS 700-2 ductile irons, the actual values of ultimate tensile strength and yield strength are much lower than the nominal ones. In the case of ferritic matrix, the reduction of mechanical properties is lower. It is also important to note that, due to the presence of chunky graphite, the ultimate tensile strength and more markedly, the elongation at failure, showed a considerable reduction compared to chunky-free castings. Tensile test results confirmed, that ferritic ductile irons are less affected by the wall thickness and cooling rate, compared to pearlitic ductile irons. Brinell hardness (HBW 5/750) tests according to UNI EN ISO 6506:2006 [49] have been also performed on samples. Details and results of fatigue tests are shown in Table 7.3.

Table 7.2. Mechanical properties of the castings.

Material	Casting code	σ_{UTS} [MPa]	$\sigma_{y\ 0.2\%}$ [MPa]	ε_R %	Hardness HB
GJS 700-2 Pearlitic	P-A	579	364	2.6	220
	P-B	513	368	1.9	220
	P-E	511	410	2.0	220
	P-C	472	320	3.1	200
GJS 400-18 LT Ferritic	F-F	383	250	19.9	150
GJS 400-18 Ferritic	F-Chunky	321	265	3.4	145
	F-Good	378	267	11.5	145
SSF DI Solution strengthened ferritic	S-D	485	381	17.8	190
	S-G	511	412	15.4	195
	S-H	488	430	5.2	195
	S-I	489	384	17.8	190
	S-Y III	492	389	17.2	190
	S-Y IV	487	384	17.1	190

Table 7.3. Fatigue properties of the castings.

Material	Casting code	Number of tests	Load Ratio	$\sigma_{a\ exp\ 50\%}$ $2 \cdot 10^6$ cycles [MPa]	Scatter Index $T\sigma$
GJS 700-2 Pearlitic	P-A	22	0	120	1.50
	P-B	16	0	134	1.08
	P-E	24	0	140	1.22
	P-C	17	0	95	1.50
GJS 400-18 LT Ferritic	F-F	20	0	100	1.20
		20	-1	140	1.30
		25	-1 (RB)	175	1.23
GJS 400-18 Ferritic	F-Chunky	10	0	79	1.24
	F-Good	16	0	91	1.27
Solution strengthened ferritic	S-D	21	0	132	1.11
	S-G	26	0	131	1.15
	S-H	23	0	127	1.20
	S-I	20	0	135	1.15
		21	-1	184	1.30
	S-Y III	27	0	151	1.21
	S-Y IV	27	0	142	1.25

The analysis of the fracture surfaces of some of the broken specimens revealed that the fatigue crack initiated at solidification defects that could be microshrinkage porosities, exploded or spiky graphite particles or a combination of multiple defects (Figure 7.1). In order to estimate the maximum dimensions of the initiating defects, the projected surface of microshrinkage porosities, degenerated graphite particles or inclusions that acted as crack initiators has been measured, as shown in Figure 7.2. Using the statistical analysis of extreme values, the $\sqrt{area}_{max}$ was estimated, for each casting, by considering the dimension of the defect corresponding to the upper bound of the 95% confidence interval of the $\sqrt{area}$ distribution [38,50,51]. In Figure 7.3 it is shown an example of defect distribution, where both the microshrinkage and degenerated graphite particles acted as crack initiators. The maximum values of the estimated defects dimensions ($\sqrt{area}_{max}$) are reported in Table 7.4 together with the mean nodule count evaluated on polished samples. It can be observed in Figure 7.4 a good correlation between the nodule count and the maximum defect dimension.

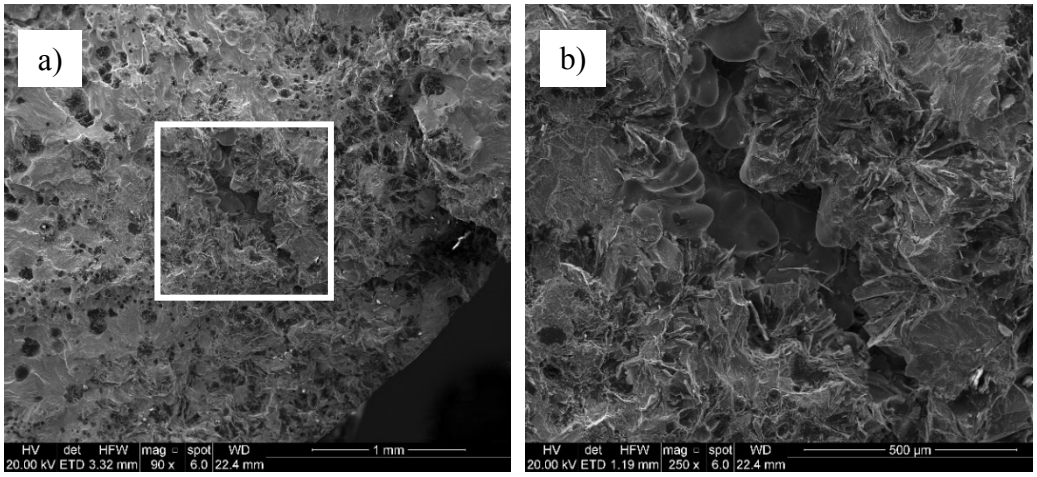

Figure 7.1. SEM macrograph of a fatigue crack initiation site (a) and particular of the simultaneous presence of microshrinkage porosity and spiky graphite (b).

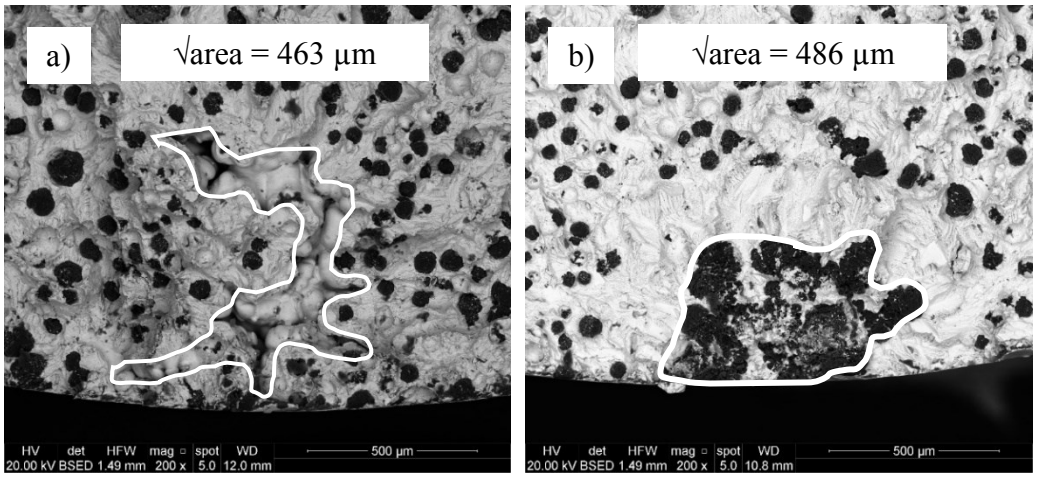

Figure 7.2. SEM images of fracture surfaces showing the dimensions (√area) of microshrinkage cavity (a) and degenerated graphite particle (b) that act as crack initiation sites.

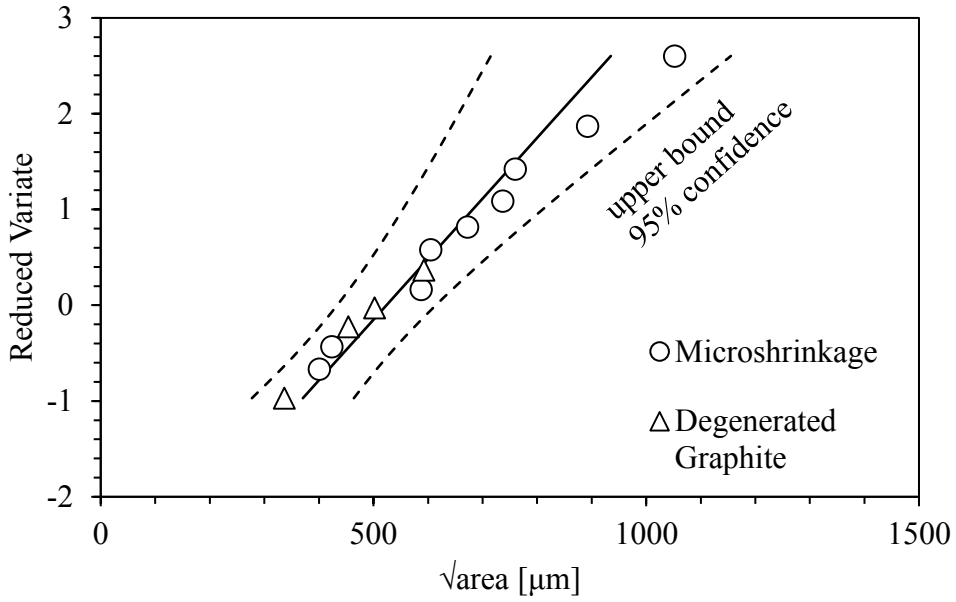

Figure 7.3. Extreme values distributions of initiating defects (microshrinkage and degenerated graphite particle) found in casting F-F.

Table 7.4. Microstructural properties of the castings.

Material	Casting code	Nodule count [mm^{-2}]	$\sqrt{area}_{max}$ [μm] 95% confidence band
GJS 700-2 Pearlitic	P-A	26	1959
	P-B	52	946
	P-E	46	806
	P-C	15	3051
GJS 400-18 LT Ferritic	F-F	31	1243
GJS 400-18 Ferritic	F-Chunky		1350
	F-Good	31	1350
SSF DI Solution strengthened ferritic	S-D	38	1188
	S-G	48	1082
	S-H	40	1212
	S-I	40	1150
	S-Y III	105	300
	S-Y IV	85	430

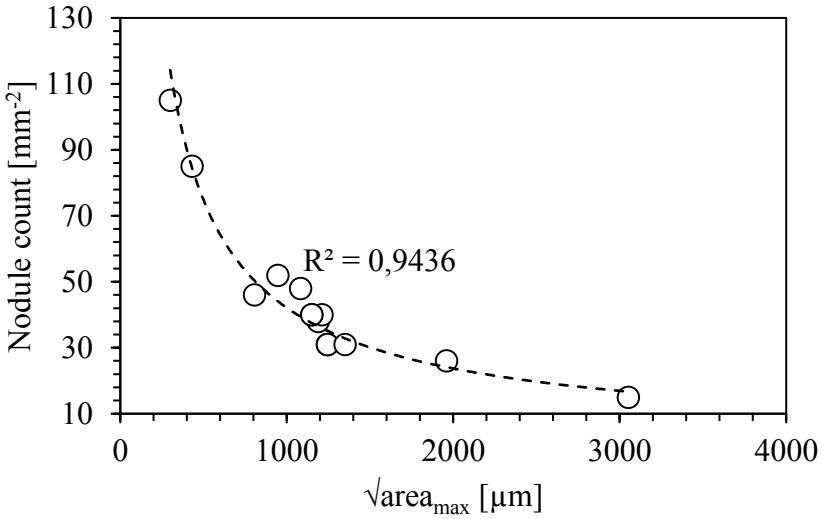

Figure 7.4. Correlation of graphite nodule count and maximum initiating defect dimensions.

As shown in Figure 7.5, it is important to note that, also in the case of heavy section castings with large solidification defects, the relationship between the experimental fatigue resistance (stress amplitude σ_a at $2 \cdot 10^6$ cycles) and the maximum defect size $\sqrt{area}_{max}$ can be still expressed, as reported in Murakami [37,38], according to the following equation:

$$\sigma_a \propto \sqrt{area}_{max}^{-1/6} \quad (4)$$

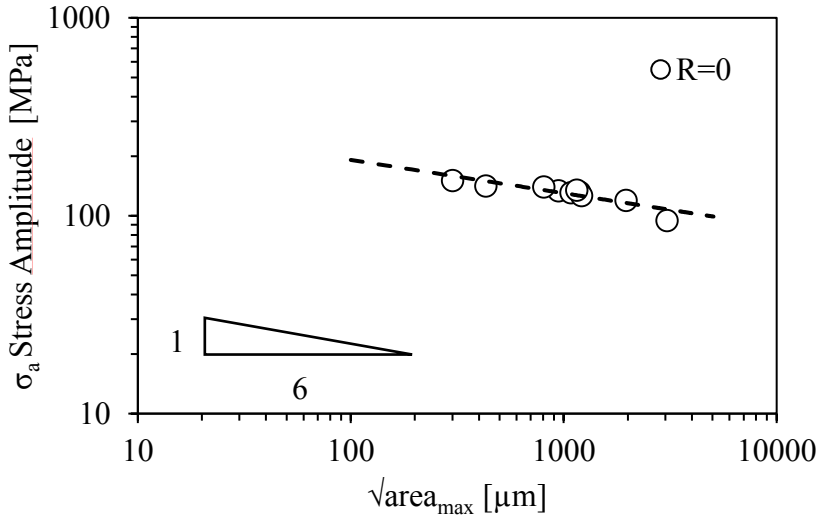

Figure 7.5. Relationship between the experimental fatigue resistance and the maximum dimension of the fatigue crack initiation defects.

7.4 Fatigue resistance prediction of as-cast heavy section ductile irons with solidification defects

The methods proposed in Murakami [38] and Deguchi [46] have been applied to the new experimental data in order to evaluate their applicability on heavy section castings with solidification defects. In order to use Murakami's equation, the measured Brinell hardness has been converted according to ASTM A370:2015 [52] standard into the Vickers hardness.

The results obtained using the two models are shown in Figure 7.6, where the comparison of the predicted and experimental fatigue resistance is plotted for each casting. It can be observed that both the methods underestimate the experimental fatigue resistance. It could be explained by considering that the two models have been developed by analysing specimens with small intrinsic defects, fine structures and high nodule count or artificial defects. It is shown in Fig. 7.4 that $\sqrt{area}_{max}$ and solidification microstructure are strictly coupled each other. The dimensions of the machined notches or holes are instead not related to (or coupled with) the real or intrinsic microstructure and thus mechanical properties of the material. In heavy section castings, the microstructure is not homogeneous and various type of detrimental defects can be present into the material (microshrinkage, degenerated, chunky or spiky graphite). These intrinsic defects, which are directly related to the production process and solidification conditions, affect the material behaviour.

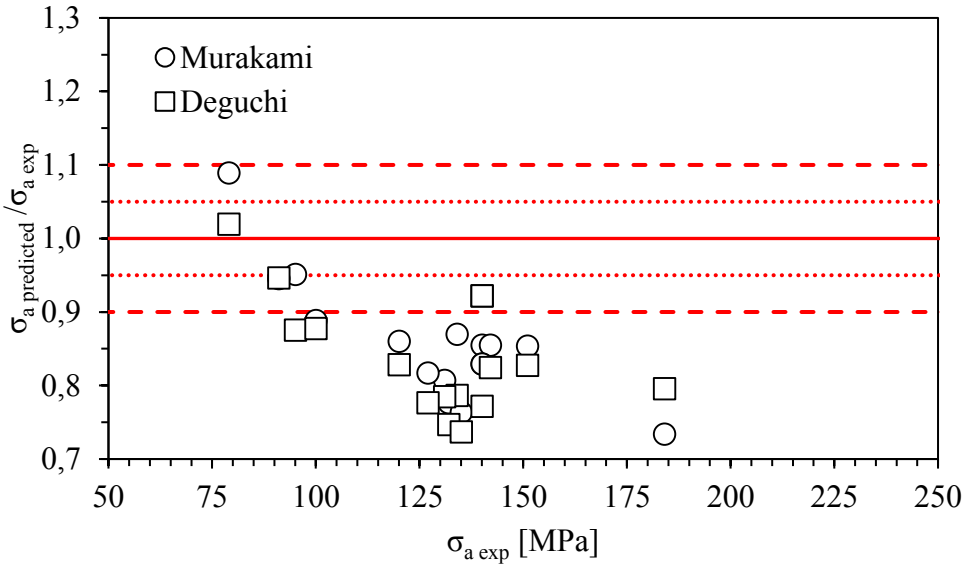

Figure 7.6. Comparison between experimental and predicted fatigue resistance according to the equations proposed by Murakami [38] and Deguchi [46].

In order to estimate the fatigue resistance of different types of as-cast ductile cast irons, characterized by solidification defects, the following expression, based on the √area is proposed herein:

$$\sigma_a = F_{loc}\frac{\left(\mathrm{A}\,\sigma_{UTS} + B\,\sigma_{y\,0.2\%}\right)}{\sqrt{area}_{max}^{\,1/6}}\left(\frac{1-R}{2}\right)^{\alpha} \qquad (5)$$

Compared to Deguchi's model (2) where only σ_{UTS} was considered as representative of the material properties, the new equation takes into account the actual mechanical properties in terms of both the ultimate strength σ_{UTS} and yield strength $\sigma_{y\,0.2\%}$ combined with the maximum value of the square root of the area of the initiating defect. The reason behind the choice of considering both the ultimate tensile strength and the yield strength in the fatigue assessment is to include in the fatigue strength evaluation the influence of the microstructural degeneration existing in the material.

As shown in some works [31–34], when degenerated chunky graphite is present, the yield stress is not much affected, while ultimate tensile strength and fatigue resistance are strongly influenced and characterized by a detrimental effect. Moreover, it has been demonstrated that, when chunky graphite is present in the

microstructure, it has a limited influence on the fatigue crack initiation compared with the effects due to microshrinkage porosities or spiky graphite, but it strongly affects the crack propagation stage.

It is not uncommon that two different materials, with different matrices and microstructures, one with and the other without degenerated graphite, may have the same ultimate tensile strength and the same size of defects (√area) but different yield and fatigue strength, due to the different nature of the matrices.

Consequently, the yield strength ($\sigma_{y\ 0.2\%}$) is more representative of the mechanical properties of the base material microstructure without any solidification defect while the ultimate strength (σ_{UTS}) is more connected with the mechanical properties of the real material fully including the solidification defects. Finally, the $\sqrt{area}_{max}$ considers only the dimensions of the fatigue crack initiating defect.

In order to estimate the parameters A, B and α (Eq. 5), the least square method was applied to the data shown in Tables 7.2 – 7.4. Eq. 5 can therefore be rewritten as follows:

$$\sigma_a = F_{loc}\frac{\left(0.62\ \sigma_{UTS} + 0.32\ \sigma_{y\ 0.2\%}\right)}{\sqrt{area}_{max}^{\ 1/6}}\left(\frac{1-R}{2}\right)^{0.576} \qquad (6)$$

In order to validate the proposed model, further experimental data were taken from the literature [9,11,25,26,28,29,33] where mechanical and fatigue properties (load ratio equal to 0 or -1) of as-cast ferritic ductile cast irons with long solidification times have been investigated. These works reported the actual mechanical properties of the materials and the dimension of the intrinsic initiating defects. In Table 7.5, the mechanical and fatigue properties are shown. It is also important to highlight that the analysed materials are characterized not only by microshrinkage porosities but also by different types of microstructural defects, such as low nodularity and nodule count, chunky or spiky graphite.

In those cases [10,11,33] were rotating bending fatigue tests were carried out, a conversion factor has been used in order to obtain an equivalent axial tension-compression stress at load ratio R = -1. In particular, as shown in Table 7.3, in the case of casting F-F, axial tension-compression tests and rotating bending tests have been carried out using specimens taken from the same position inside the blocks. The obtained fatigue resistances were 140 MPa and 175 MPa for axial tension-

compression and rotating bending respectively. The factor was defined as $\frac{\sigma_{a\ \text{Tension-Compression}}}{\sigma_{a\ \text{Rotating Bending}}} = 0.8$.

It can be observed in Figure 7.7 that also in the case of data taken from the literature, the fatigue resistance decreases following a power law with the maximum initiating defect index of about -1/6.

The fatigue resistance estimation of the analysed castings is shown in Figure 7.8, where the predicted fatigue resistance ($\sigma_{a\ predicted}$) is normalised with respect to the experimental value $\sigma_{a\ exp}$. It can be observed that the estimation is in very good agreement with the experimental data, with about 80% of the data within a ±5% scatter band, and almost all the points in ±10%.

Table 7.5. Mechanical and fatigue properties of castings taken from the literature.

Reference number	σ_{UTS} [MPa]	$\sigma_{y0,2\%}$ [MPa]	Load Ratio	$\sigma_{a\ exp\ 50\%}$ (Tension)	$\sigma_{a\ exp\ 50\%}$ (RB)
10	295	275	-1		138
33	412	275	-1		198
33	355	276	-1		163
25-26	410	250	-1	160	
25-26	410	250	-1	175	
25-26	410	250	-1	190	
25-26	410	250	-1	215	
28-29	375	250	-1	110	
28-29	400	230	0	130	
28-29	400	230	-1	180	
9	341	240	-1		160
9	375	242	-1		200
9	370	236	-1		170
9	371	235	-1		200
11	329	286	-1		145
11	353	298	-1		167
11	295	275	-1		138
11	249	249	-1		130

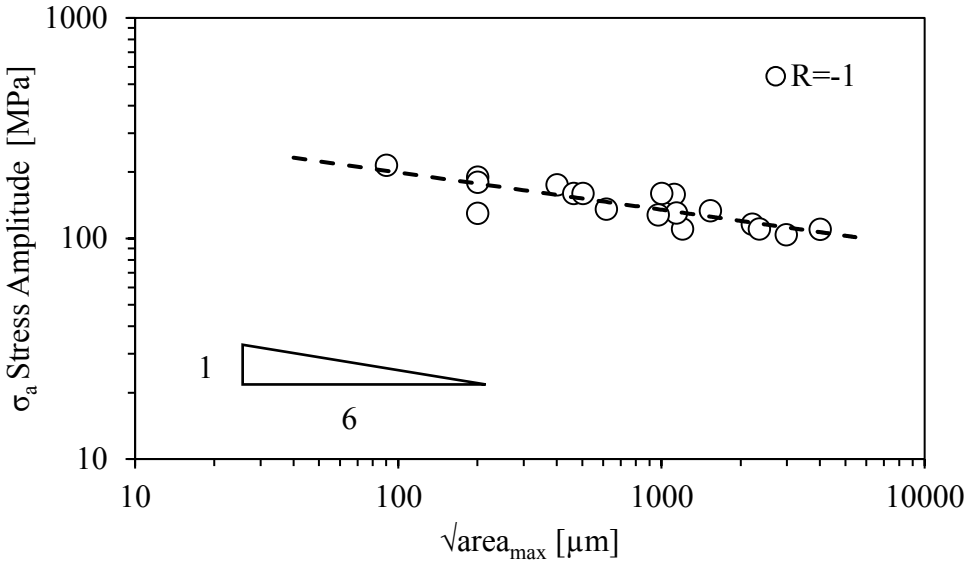

Figure 7.7. Relationship between fatigue resistance of data taken from literature and the maximum dimension of the fatigue crack initiation defects.

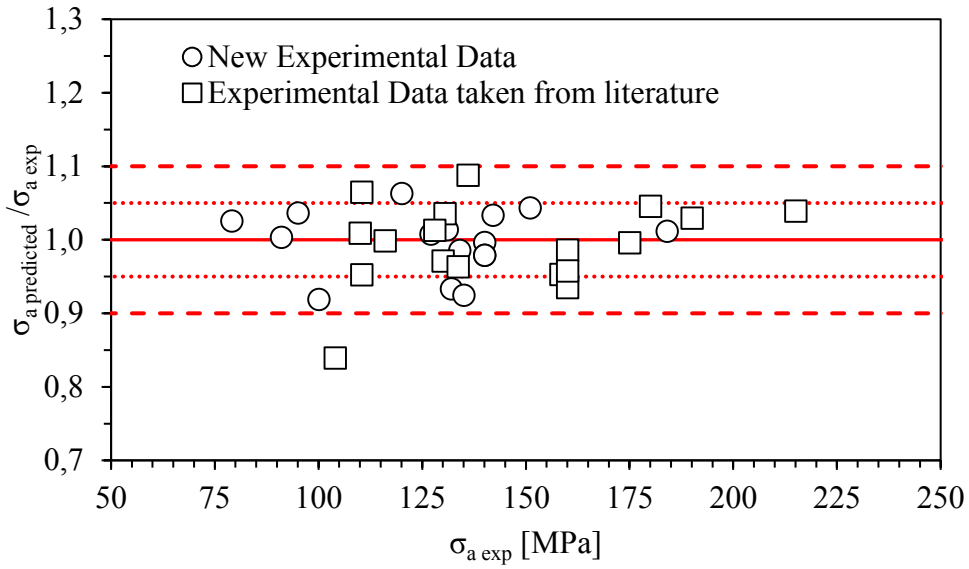

Figure 7.8. Comparison of experimental and predicted fatigue resistance according to equation (6), with ±5% and ±10% scatter band.

7.5 Conclusions

In this chapter, a model able to predict the fatigue resistance of different as-cast ductile irons containing different kinds of solidification defects has been proposed. The model takes into account the effect of the initiating defects through the $\sqrt{area}_{max}$ dimension that has been evaluated by means of an accurate analysis of the fatigue crack initiation defects. It is important to note that microshrinkage porosities and degenerated graphite particles have been considered all together in the study.

The proposed equation takes also into account the actual mechanical properties of the materials (σ_{UTS} and $\sigma_{y\ 0.2\%}$). In particular, the yield strength ($\sigma_{y\ 0.2\%}$) is representative of the mechanical properties of the base material without microshrinkage porosities or degenerated graphite particles while σ_{UTS} takes into account the mechanical properties of the real material fully including the solidification defects due to the long time of solidification.

The method has been validated by using both data taken from the literature and a new set of experimental measurements.

Compared to the models previously proposed in the literature, the present equation allows a more reliable estimation of the fatigue strength of different types of as-cast heavy section ductile irons containing various types of solidification defects.

References

[1] UNI EN 1563:2012, Founding - Spheroidal graphite cast irons.

[2] Minnebo P, Nilsson K-F, Blagoeva D. Tensile, Compression and Fracture Properties of Thick-Walled Ductile Cast Iron Components. J Mater Eng Perform 2007;16:35–45. doi:10.1007/s11665-006-9005-z.

[3] Ecob CM. A review of common metallurgical defects in ductile cast iron 2005.

[4] Kallbom R, Hamberg K, Wessén M, Bjorkegren LE. On the solidification sequence of ductile iron castings containing chunky graphite. Mater Sci Eng A 2005;414:346–51.

[5] Pan EN, Chen CY. Effect of Bi and Sb on graphite structure of heavy-section ductile cast iron. Trans Am Foundrymen's Soc 1996;104:845–58.

[6] Ferro P, Fabrizi A, Cervo R, Carollo C. Effect of inoculant containing rare earth metals and bismuth on microstructure and mechanical properties of heavy-section near-eutectic ductile iron castings. J Mater Process Technol 2013;213:1601–8. doi:10.1016/j.jmatprotec.2013.03.012.

[7] Borsato T, Berto F, Ferro P, Carollo C. Effect of in-mould inoculant composition on microstructure and fatigue behaviour of heavy section ductile iron castings. Procedia Struct Integr 2016;2:3150–7. doi:10.1016/j.prostr.2016.06.393.

[8] Christoph Bleicher, Rainer Wagener, Heinz Kaufmann, Tobias Melz. Fatigue strength of nodular cast iron with regard to heavy-wall applications. Mater Test 2015;57:723–31.

[9] Shiraki N, Usui Y, Kanno T. Effects of Number of Graphite Nodules on Fatigue Limit and Fracture Origins in Heavy Section Spheroidal Graphite Cast Iron. Mater Trans 2016;57:379–84. doi:10.2320/matertrans.F-M2015841.

[10] Benedetti M, Torresani E, Fontanari V, Lusuardi D. Fatigue and Fracture Resistance of Heavy-Section Ferritic Ductile Cast Iron. Metals (Basel) 2017;7:88. doi:10.3390/met7030088.

[11] Foglio E, Gelfi M, Pola A, Lusuardi D. Effect of Shrinkage Porosity and Degenerated Graphite on Fatigue Crack Initiation in Ductile Cast Iron. Key Eng Mater 2017;754:95–8. doi:10.4028/www.scientific.net/KEM.754.95.

[12] Borsato T, Ferro P, Berto F, Carollo C. Mechanical and Fatigue Properties of Heavy Section Solution Strengthened Ferritic Ductile Iron Castings. Adv Eng Mater 2016;18:2070–5. doi:10.1002/adem.201600256.

[13] Čanžar P, Tonković Z, Kodvanj J. Microstructure influence on fatigue behaviour of nodular cast iron. Mater Sci Eng A 2012;556:88–99. doi:10.1016/j.msea.2012.06.062.

[14] Iacoviello F, Di Bartolomeo O, Di Cocco V, Piacente V. Damaging micromechanisms in ferritic–pearlitic ductile cast irons. Mater Sci Eng A 2008;478:181–6. doi:10.1016/j.msea.2007.05.110.

[15] Cavallini M, Di Bartolomeo O, Iacoviello F. Fatigue crack propagation damaging micromechanisms in ductile cast irons. Eng Fract Mech 2008;75:694–704. doi:10.1016/j.engfracmech.2007.02.002.

[16] Di Cocco V, Iacoviello F, Cavallini M. Damaging micromechanisms characterization of a ferritic ductile cast iron. Eng Fract Mech 2010;77:2016–23. doi:10.1016/j.engfracmech.2010.03.037.

[17] Iacoviello F, Cocco V Di. Ductile Cast irons: microstructure influence on fatigue crack propagation resistance. Frat Ed Integrità Strutt 2010;13:3–16. doi:10.3221/IGF-ESIS.13.01.

[18] Di Cocco V, Iacoviello F, Rossi A, Iacoviello D. Macro and microscopical approach to the damaging micromechanisms analysis in a ferritic ductile cast iron. Theor Appl Fract Mech 2014;69:26–33. doi:10.1016/j.tafmec.2013.11.003.

[19] Di Cocco V, Iacoviello F, Rossi A, Cavallini M, Natali S. Graphite nodules and fatigue crack propagation micromechanisms in a ferritic ductile cast iron. Fatigue Fract Eng Mater Struct 2013;36:893–902. doi:10.1111/ffe.12056.

[20] Iacoviello F, Cocco V Di. Degenerated graphite nodules influence on fatigue crack paths in a ferritic ductile cast iron. Frat Ed Integrita Strutt 2015;9:406–14. doi:10.3221/IGF-ESIS.34.45.

[21] Nadot, Mendez, Ranganathan, Beranger. Fatigue life assessment of nodular cast iron containing casting defects. Fatigue Fract Eng Mater Struct 1999;22:289–300. doi:10.1046/j.1460-2695.1999.00162.x.

[22] Nadot Y. Influence of casting defects on the fatigue limit of nodular cast iron. Int J Fatigue 2004;26:311–9. doi:10.1016/S0142-1123(03)00141-5.

[23] Collini L, Pirondi A, Bianchi R, Cova M, Milella PP. Influence of casting defects on fatigue crack initiation and fatigue limit of ductile cast iron. Procedia Eng 2011.

[24] Collini L, Pirondi A. Fatigue crack growth analysis in porous ductile cast iron microstructure. Int J Fatigue 2014;62:258–65. doi:10.1016/j.ijfatigue.2013.06.020.

[25] Kainzinger P, Guster C, Severing M, Wolf A. Influence of micro-shrinkage on the fatigue behavior of ductile iron. 13 Int. Conf. Fract., 2013, p. 1–9.

[26] Kainzinger P, Wohlfahrt M, Grün F. Einfluss der lokalen Gefügeausbildung auf die Schwingfestigkeit von Gusseisen mit Kugelgraphit. BHM Berg- Und Hüttenmännische Monatshefte 2015;160:2–8. doi:10.1007/s00501-014-0328-z.

[27] Shirani M, Härkegård G. A review on fatigue design of heavy section EN-GJS-400- 18-LT ductile iron wind turbine castings. Energy Equip Syst 2014;2:5–24.

[28] Shirani M, Härkegård G. Damage tolerant design of cast components based on defects detected by 3D X-ray computed tomography. Int J Fatigue 2012;41:188–98. doi:10.1016/j.ijfatigue.2011.09.011.

[29] Shirani M, Härkegård G. Fatigue life distribution and size effect in ductile cast iron for wind turbine components. Eng Fail Anal 2011;18:12–24. doi:10.1016/j.engfailanal.2010.07.001.

[30] Shirani M, Härkegård G. Large scale axial fatigue testing of ductile cast iron for heavy section wind turbine components. Eng Fail Anal 2011;18:1496–510.

[31] Mourujärvi A, Widell K, Saukkonen T, Hänninen H. Influence of chunky graphite on mechanical and fatigue properties of heavy-section cast iron. Fatigue Fract Eng Mater Struct 2009;32:379–90. doi:10.1111/j.1460-2695.2009.01337.x.

[32] Ferro P, Lazzarin P, Berto F. Fatigue properties of ductile cast iron containing chunky graphite. Mater Sci Eng A 2012;554:122–8.

[33] Foglio E, Lusuardi D, Pola A, La Vecchia GM, Gelfi M. Fatigue design of heavy section ductile irons: Influence of chunky graphite. Mater Des 2016;111:353–61. doi:10.1016/j.matdes.2016.09.002.

[34] Borsato T, Ferro P, Berto F, Carollo C. Fatigue properties of solution strengthened ferritic ductile cast irons in heavy section castings. Metall Ital 2017;109:25–32.

[35] Borsato T, Ferro P, Berto F, Carollo C. Mechanical and fatigue properties of pearlitic ductile iron castings characterized by long solidification times. Eng Fail Anal 2017;79:902–12. doi:10.1016/j.engfailanal.2017.06.007.

[36] Borsato T, Ferro P, Berto F, Carollo C. Fatigue strength improvement of heavy-section pearlitic ductile iron castings by in-mould inoculation treatment. Int J Fatigue 2016. doi:10.1016/j.ijfatigue.2017.02.012.

[37] Murakami Y, Endo M. Effects of Hardness and Crack Geometries on DeltaKth of Small Cracks Emanating from Small Defects. Proceedings, Behav. short fatigue cracks, Mech. Eng. Publ., 1986, p. 275–94.

[38] Murakami Y. Metal fatigue: effects of small defects and nonmetallic inclusions. 2002.

[39] Endo M, Iseda K. Prediction of the Fatigue Strength of Nodular Cast Irons under combined loadings. Int J Mod Phys B 2006;20:3817–23.

[40] Endo M. Effects of graphite shape, size and distribution on the fatigue strength of spheroidal graphite cast irons. J Soc Mater Sci Japan 1989;38:1139–44. doi:10.2472/jsms.38.1139.

[41] Endo M, Wang X-B. Effects of graphite and artificial small defect on the fatigue strength of current ductile cast irons. J Soc Mater Sci Japan 1994;43:1245–50. doi:10.2472/jsms.43.1245.

[42] Endo M. Fatigue Strength Prediction of Ductile Irons Subjected To Combined Loading. ECF13, San Sebastian, vol. 43, 2000.

[43] Endo M, Yanase K. Effects of small defects, matrix structures and loading conditions on the fatigue strength of ductile cast irons. Theor Appl Fract Mech 2014;69:34–43. doi:10.1016/j.tafmec.2013.12.005.

[44] Deguchi T, Matsuo T, Takemoto S, Ikeda T, Endo M. Effects of graphite and artificial defects on the fatigue stregnth of ferritic pearlitic ductile cast iron. Proc. 5th Int. Conf. Fract. Fatigue Wear, 2016, p. 93–8.

[45] Deguchi T, Matsuo T, Kim H, Ikeda T, Endo M. Fatigue Strength Evaluation of Ferritic-Pearlitic Ductile Cast Iron with Notches and Holes of Various Sizes. Adv Exp Mech 2017;2:87–91.

[46] Deguchi T, Kim HJ, Ikeda T. Fatigue limit prediction of ferritic-pearlitic ductile cast iron considering stress ratio and notch size. J Phys Conf Ser 2017;842:012067. doi:10.1088/1742-6596/842/1/012067.

[47] Deguchi T, Kim HJ, Ikeda T, Yanase K. Influence of mean stress on fatigue strength of ferritic-pearlite ductile cast iron with small defects. J Phys Conf Ser 2017;843:012049. doi:10.1088/1742-6596/843/1/012049.

[48] Atzori B, Lazzarin P. Notch sensitivity and defect sensitivity under fatigue loading. Int J Fract 2000;107:3–8. doi:10.1023/A:1007686727207.

[49] UNI EN ISO 6506-1:2006, Metallic materials - Brinell hardness test - Part 1: Test method.

[50] Murakami Y. Inclusion rating by statistics of extreme values and its application to fatigue strength prediction and quality control of materials. J Res Natl Inst Stand Technol 1994;99:345. doi:10.6028/jres.099.032.

[51] Beretta S, Murakami Y. Statistical Analysis of Defects for Fatigue Strength Prediction and Quality Control of Materials. Fatigue Fract Eng Mater Struct 1998;21:1049–65. doi:10.1046/j.1460-2695.1998.00104.x.

[52] ASTM A370-15, Standard Test Methods and Definitions for Mechanical Testing of Steel Products, ASTM International, West Conshohocken, PA, 2015.

8. *Concluding remarks*

This Ph.D. thesis derives form an intense research activity on topics that, in the recent years, have met the interest of many international experts of both academic and industrial world.

The main purposes of the study are briefly summarized:

- Obtainment of a new set of experimental data on different grades of traditional ductile irons characterized by long solidification conditions, in order to improve the knowledge on this type of materials.
- Characterization of microstructural and mechanical properties of new generation ductile irons subjected to different cooling conditions, due to the lack in literature of experimental data.
- Evaluation of the effect of microstructural solidification defects on the mechanical behaviour of ductile cast irons.
- Development of a method that allows estimating, with good accuracy, the mechanical behaviour of components under fatigue cycling loading conditions

An extensive experimental activity has been carried out considering different ductile irons in order to characterize microstructural and mechanical properties as a function of different conditions of cooling and solidification. For this reason, specific casting geometries have been used, from which specimens for the mechanical tests have been taken.

Firstly, tensile tests at room temperature have been conducted.

In the case of traditional ferritic ductile cast iron GJS 400-18 LT it was found that mechanical properties were very homogeneous inside the whole casting and were not much lower than typical values obtained from the standard samples.

On the other hand, mechanical properties of traditional pearlitic ductile iron GJS 700-2 were found to be much affected by long solidification times. This was

attributed to the pearlitic matrix, which is much more sensitive to cooling conditions than the ferritic one.

In the case of solution strengthened ferritic ductile irons it was confirmed that, increasing the Silicon content, the ultimate tensile strength and the yield stress increase, while the elongation at failure decreases, also in low cooling rate conditions. It has been observed that increasing section thickness and solidification time, the mechanical properties decrease, but, thanks to the solution strengthening mechanisms, they are less influenced than the traditional ferritic/pearlitic cast irons. It has been also found that, considering long solidification times, new generation ductile irons are characterized by strength similar to those of pearlitic grades, while the ductility is comparable to the typical values of traditional ferritic grades.

From fatigue test results, it was confirmed that a better estimation of the fatigue life is achievable by considering the solidification times rather than the section thickness.

Considering specimens taken from most critical zones inside each casting, characterized by long solidification times and slow cooling rates, it has been observed that, despite the difference in the microstructure, solution strengthened ferritic ductile irons behave in a similar manner than the pearlitic ones, not only under static but also under dynamic loading conditions. Traditional ferritic grade (GJS 400-18 LT) exhibits the lower fatigue resistance.

The analysis of the fracture surfaces of the fatigue broken specimens revealed that the fatigue crack initiated at microstructural defects, such as microshrinkage porosities, exploded or spiky graphite particles or a combination of multiple defects. By using statistical analysis of extreme values, their maximum dimensions have been estimated.

On the basis of the experimental findings, a model able to predict the fatigue resistance of different as-cast ductile irons containing different kinds of solidification defects has been proposed. The method has been validated by using both data taken from the literature and a new set of experimental measurements. Compared to the models previously proposed in the literature, the present equation allows a more reliable estimation of the fatigue strength of different types of as-cast heavy section ductile irons containing various types of solidification defects.

Bibliography

Alhussein, A., Risbet, M., Bastien, A., Chobaut, J.P., Balloy, D., Favergeon, J., 2014. Influence of silicon and addition elements on the mechanical behavior of ferritic ductile cast iron. Mater. Sci. Eng. A 605, 222–228.

ASTM A370-15, Standard Test Methods and Definitions for Mechanical Testing of Steel Products, ASTM International, West Conshohocken, PA, 2015.

ASTM E2283-08(2014), Standard Practice for Extreme Value Analysis of Nonmetallic Inclusions in Steel and Other Microstructural Features, ASTM International, West Conshohocken, PA, 2014.

ASTM E2567-11, Standard Test Method for Determining Nodularity And Nodule Count In Ductile Iron Using Image Analysis, ASTM International, West Conshohocken, PA, 2011.

Atzori, B., Lazzarin, P., 2000. Notch sensitivity and defect sensitivity under fatigue loading. Int. J. Fract. 107, 3–8. doi:10.1023/A:1007686727207

Benedetti, M., Torresani, E., Fontanari, V., Lusuardi, D., 2017. Fatigue and Fracture Resistance of Heavy-Section Ferritic Ductile Cast Iron. Metals (Basel). 7, 88. doi:10.3390/met7030088

Beretta, S., Murakami, Y., 1998. Statistical Analysis of Defects for Fatigue Strength Prediction and Quality Control of Materials. Fatigue Fract. Eng. Mater. Struct. 21, 1049–1065. doi:10.1046/j.1460-2695.1998.00104.x

Björkegren, L.E., Hamberg, K., 2003. Silicon alloyed ductile iron with excellent ductility and machinability, in: Proc. Keith Millis Symp.

Björkegren, L.E., Hamberg, K., Johannesson, B., 1996. Mechanical properties and machinability of Si-solution-hardened ferritic ductile iron. Trans. Am. Foundrymen's Soc. 104, 139.

Bleicher, C., Wagener, R., Kaufmann, H., Melz, T., 2017. Fatigue Assessment of Nodular Cast Iron with Material Imperfections. SAE Int. J. Engines 10, 2017-01–0344. doi:10.4271/2017-01-0344

Bleicher, C., Wagener, R., Kaufmann, H., Melz, T., 2015. Fatigue strength of nodular cast iron with regard to heavy-wall applications. Mater. Test. 57, 723–731. doi:10.3139/120.110782

Bočkus, S., Venckunas, A., Žaldarys, G., 2008. Relation between section thickness, microstructure and mechanical properties of ductile iron castings. Medziagotyra 14, 115–118.

Borsato, T., Berto, F., Ferro, P., Carollo, C., 2016. Effect of in-mould inoculant composition on microstructure and fatigue behaviour of heavy section ductile iron castings. Procedia Struct. Integr. 2, 3150–3157. doi:10.1016/j.prostr.2016.06.393

Borsato, T., Ferro, P., Berto, F., Carollo, C., 2017. Fatigue strength improvement of heavy-section pearlitic ductile iron castings by in-mould inoculation treatment. Int. J. Fatigue 102, 221–227. doi:10.1016/j.ijfatigue.2017.02.012

Borsato, T., Ferro, P., Berto, F., Carollo, C., 2017. Mechanical and fatigue properties of pearlitic ductile iron castings characterized by long solidification times. Eng. Fail. Anal. 79, 902–912. doi:10.1016/j.engfailanal.2017.06.007

Borsato, T., Ferro, P., Berto, F., Carollo, C., 2017. Fatigue properties of solution strengthened ferritic ductile cast irons in heavy section castings. Metall. Ital. 109, 25–32.

Borsato, T., Ferro, P., Berto, F., Carollo, C., 2016. Mechanical and Fatigue Properties of Heavy Section Solution Strengthened Ferritic Ductile Iron Castings. Adv. Eng. Mater. 18, 2070–2075. doi:10.1002/adem.201600256

Čanžar, P., Tonković, Z., Kodvanj, J., 2012. Microstructure influence on fatigue behaviour of nodular cast iron. Mater. Sci. Eng. A 556, 88–99. doi:10.1016/j.msea.2012.06.062

Cavallini, M., Di Bartolomeo, O., Iacoviello, F., 2008. Fatigue crack propagation damaging micromechanisms in ductile cast irons. Eng. Fract. Mech. 75, 694–704. doi:10.1016/j.engfracmech.2007.02.002

Ceschini, L., Morri, A., Morri, A., 2017. Effects of Casting Size on Microstructure and Mechanical Properties of Spheroidal and Compacted Graphite Cast Irons: Experimental Results and Comparison with International Standards. J. Mater. Eng. Perform. 26, 2583–2592. doi:10.1007/s11665-017-2714-7

Collini, L., Pirondi, A., 2014. Fatigue crack growth analysis in porous ductile cast iron microstructure. Int. J. Fatigue 62, 258–265. doi:10.1016/j.ijfatigue.2013.06.020

Collini, L., Pirondi, A., Bianchi, R., Cova, M., Milella, P.P., 2011. Influence of casting defects on fatigue crack initiation and fatigue limit of ductile cast iron. Procedia Eng. 10, 2898–2903. doi:10.1016/j.proeng.2011.04.481

Davis, J.R., 1996. ASM specialty handbook: cast irons. ASM international.

de la Torre, U., Lacaze, J., Sertucha, J., 2016. Chunky graphite formation in ductile cast irons: effect of silicon, carbon and rare earths. Int. J. Mater. Res. 107, 1041–1050. doi:10.3139/146.111434

de la Torre, U., Loizaga, A., Lacaze, J., Sertucha, J., 2014. As cast high silicon ductile irons with optimised mechanical properties and remarkable fatigue properties. Mater. Sci. Technol. 30, 1425–1431. doi:10.1179/1743284713Y.0000000483

Deguchi, T., 2017. Fatigue Strength Evaluation of Ferritic-Pearlitic Ductile Cast Iron with Notches and Holes of Various Sizes. Adv. Exp. Mech. 2, 87–91.

Deguchi, T., Kim, H.J., Ikeda, T., 2017. Fatigue limit prediction of ferritic-pearlitic ductile cast iron considering stress ratio and notch size. J. Phys. Conf. Ser. 842, 012067. doi:10.1088/1742-6596/842/1/012067

Deguchi, T., Kim, H.J., Ikeda, T., Yanase, K., 2017. Influence of mean stress on fatigue strength of ferritic-pearlite ductile cast iron with small defects. J. Phys. Conf. Ser. 843, 012049. doi:10.1088/1742-6596/843/1/012049

Deguchi, T., Matsuo, T., Takemoto, S., Ikeda, T., Endo, M., 2016. Effects of graphite and artificial defects on the fatigue stregnth of ferritic pearlitic ductile cast iron, in: Proceedings of the 5th International Conference on Fracture Fatigue and Wear,. pp. 93–98.

Di Cocco, V., Iacoviello, F., Cavallini, M., 2010. Damaging micromechanisms characterization of a ferritic ductile cast iron. Eng. Fract. Mech. 77, 2016–2023. doi:10.1016/j.engfracmech.2010.03.037

Di Cocco, V., Iacoviello, F., Rossi, A., Cavallini, M., Natali, S., 2013. Graphite nodules and fatigue crack propagation micromechanisms in a ferritic ductile cast iron. Fatigue Fract. Eng. Mater. Struct. 36, 893–902. doi:10.1111/ffe.12056

Di Cocco, V., Iacoviello, F., Rossi, A., Iacoviello, D., 2014. Macro and microscopical approach to the damaging micromechanisms analysis in a ferritic ductile cast iron. Theor. Appl. Fract. Mech. 69, 26–33. doi:10.1016/j.tafmec.2013.11.003

Ecob, C.M., 2005. A review of common metallurgical defects in ductile cast iron.

Endo, M., 2000. Fatigue Strength Prediction of Ductile Irons Subjected To Combined Loading, in: ECF13, San Sebastian.

Endo, M., 1989. Effects of graphite shape, size and distribution on the fatigue strength of spheroidal graphite cast irons. J. Soc. Mater. Sci. Japan 38, 1139–1144. doi:10.2472/jsms.38.1139

Endo, M., Iseda, K., 2006. Prediction of the Fatigue Strength of Nodular Cast Irons under combined loadings. Int. J. Mod. Phys. B 20, 3817–3823.

Endo, M., Wang, X.B., 1994. Special Issue on Fracture Mechanics. Effects of Graphite and Artificial Small Defect on theFatigue Strength of Current Ductile Cast Irons. J. Soc. Mater. Sci. Japan 43, 1245–1250. doi:10.2472/jsms.43.1245

Endo, M., Yanase, K., 2014. Effects of small defects, matrix structures and loading conditions on the fatigue strength of ductile cast irons. Theor. Appl. Fract. Mech. 69, 34–43. doi:10.1016/j.tafmec.2013.12.005

Ferro, P., Fabrizi, A., Cervo, R., Carollo, C., 2013. Effect of inoculant containing rare earth metals and bismuth on microstructure and mechanical properties of heavy-section near-eutectic ductile iron castings. J. Mater. Process. Technol. 213, 1601–1608. doi:10.1016/j.jmatprotec.2013.03.012

Ferro, P., Lazzarin, P., Berto, F., 2012. Fatigue properties of ductile cast iron containing chunky graphite. Mater. Sci. Eng. A 554, 122–128.

Foglio, E., Gelfi, M., Pola, A., Goffelli, S., Lusuardi, D., 2017a. Fatigue Characterization and Optimization of the Production Process of Heavy Section Ductile Iron Castings. Int. J. Met. 11, 33–43. doi:10.1007/s40962-016-0112-9

Foglio, E., Gelfi, M., Pola, A., Lusuardi, D., 2017b. Effect of Shrinkage Porosity and Degenerated Graphite on Fatigue Crack Initiation in Ductile Cast Iron. Key Eng. Mater. 754, 95–98. doi:10.4028/www.scientific.net/KEM.754.95

Foglio, E., Lusuardi, D., Pola, A., La Vecchia, G.M., Gelfi, M., 2016. Fatigue design of heavy section ductile irons: Influence of chunky graphite. Mater. Des. 111, 353–361. doi:10.1016/j.matdes.2016.09.002

Glavas, Z., Strkalj, A., Stojakovic, A., 2016. The properties of silicon alloyed ferritic ductile irons. Metalutgija 55, 293–296.

Herfurth, K., Gorski, R., Beute, K., Hering, M. Cast material for mechanical engineering with higher strength and breaking elongation and highly homogeneous hardness distribution. http://www.gontermann-peipers.de/uploads/media/fachartikel_GOPAG_engl_01.pdf.

Hsu, C., Chen, M., Hu, C., 2007. Microstructure and mechanical properties of 4 % cobalt and nickel alloyed ductile irons. Mater. Sci. Eng. A 444, 339–346.

Iacoviello, F., Cocco, V. Di, 2015. Degenerated graphite nodules influence on fatigue crack paths in a ferritic ductile cast iron. Frat. ed Integrita Strutt. 9, 406–414. doi:10.3221/IGF-ESIS.34.45

Iacoviello, F., Cocco, V. Di, 2010. Ductile Cast irons: microstructure influence on fatigue crack propagation resistance. Frat. ed Integrità Strutt. 13, 3–16. doi:10.3221/IGF-ESIS.13.01

Iacoviello, F., Di Bartolomeo, O., Di Cocco, V., Piacente, V., 2008. Damaging micromechanisms in ferritic–pearlitic ductile cast irons. Mater. Sci. Eng. A 478, 181–186. doi:10.1016/j.msea.2007.05.110

ISO 148-1: 2009. Metallic materials – Charpy pendulum impact test – Part 1: Test method.

ISO 12107: 2012. Metallic materials-Fatigue testing-Statistical planning and analysis of data.

ISO 6506-1:2005 Metallic materials -- Brinell hardness test -- Part 1: Test method.

ISO 6892-1:2016 Metallic materials — Tensile testing — Part 1: Method of test at room temperature.

Itofuji, H., Uchikawa, H., 1990. Formation mechanism of chunky graphite in heavy-section ductile cast irons. Trans. Am. Foundrymen's Soc. 98, 429–446.

Jiyang, Z., Schmitz, W., Engler, S., 1989. Formation of austenite shell around spheroidal graphite and its effect on deterioration of graphite. Acta Metall. Sin. 2, 261–265.

Kainzinger, P., Guster, C., Severing, M., Wolf, A., 2013. Influence of micro-shrinkage on the fatigue behavior of ductile iron., in: 13 International Conference on Fracture. pp. 1–9.

Kainzinger, P., Wohlfahrt, M., Grün, F., 2015. Einfluss der lokalen Gefügeausbildung auf die Schwingfestigkeit von Gusseisen mit Kugelgraphit. BHM Berg- und Hüttenmännische Monatshefte 160, 2–8. doi:10.1007/s00501-014-0328-z

Kallbom, R., Hamberg, K., Wessén, M., Bjorkegren, L.E., 2005. On the solidification sequence of ductile iron castings containing chunky graphite. Mater. Sci. Eng. A 414, 346–351.

Karsay, S.I., 1976. Ductile Iron: Production: the State of the Art, Quebec Iron and Titanium Corporation.

Kasvayee, K.A., Ghassemali, E., Svensson, I.L., Olofsson, J., Jarfors, A.E.W., 2017. Characterization and modeling of the mechanical behavior of high silicon ductile iron. Mater. Sci. Eng. A 708, 159–170. doi:10.1016/j.msea.2017.09.115

Labrecque, C., Gagné, M., 1998. Ductile Iron: Fifty Years of Continuous Development. Can. Metall. Q. 37, 343–378. doi:10.1179/cmq.1998.37.5.343

Larker, R., 2009. Solution strenghened ferritic ductile iron ISO 1083/JS/500-10 provides superior Consistent properties in hydraulic rotators. China Foundry 6, 343–351.

Larrañaga, P., Asenjo, I., Sertucha, J., Suarez, R., Ferrer, I., Lacaze, J., 2009. Effect of antimony and cerium on the formation of chunky graphite during solidification of heavy-section castings of near-eutectic spheroidal graphite irons. Metall. Mater. Trans. A Phys. Metall. Mater. Sci. 40, 654–661. doi:10.1007/s11661-008-9731-y

Lin, H., Lui, T., Chen, L., 2003. Effect of Silicon Content on Intergranular Embrittlement of Ferritic Spheroidal Graphite Cast Iron Suffered from Cyclic Heating. Mater. Trans. 44, 173–180. doi:10.2320/matertrans.44.173

Loper, C.R., Heine, R.W., Reesman, R.W., Shah, B.H., 1967. Thermal Analysis of Ductile Iron. Trans. Am. Foundrymen's Soc. 75, 541–547.

Luo, J., Harding, R.A., Bowen, P., 2002. Evaluation of the fatigue behavior of ductile irons with various matrix microstructures. Metall. Mater. Trans. A Phys. Metall. Mater. Sci. 33, 3719–3730. doi:10.1007/s11661-002-0244-9

Luo, J., Harding, R.A., Bowen, P., 2002. Evaluation of the fatigue behavior of ductile irons with various matrix microstructures. Metall. Mater. Trans. A Phys. Metall. Mater. Sci. 33, 3719–3730. doi:10.1007/s11661-002-0244-9

Minnebo, P., Nilsson, K.-F., Blagoeva, D., 2007. Tensile, Compression and Fracture Properties of Thick-Walled Ductile Cast Iron Components. J. Mater. Eng. Perform. 16, 35–45. doi:10.1007/s11665-006-9005-z

Mourujärvi, A., Widell, K., Saukkonen, T., Hänninen, H., 2009. Influence of chunky graphite on mechanical and fatigue properties of heavy-section cast iron. Fatigue Fract. Eng. Mater. Struct. 32, 379–390. doi:10.1111/j.1460-2695.2009.01337.x

Murakami, Y., 2002. Metal fatigue: effects of small defects and nonmetallic inclusions, Elsevier.

Murakami, Y., 1994. Inclusion rating by statistics of extreme values and its application to fatigue strength prediction and quality control of materials. J. Res. Natl. Inst. Stand. Technol. 99, 345. doi:10.6028/jres.099.032

Murakami, Y., Endo, M., 1986. Effects of Hardness and Crack Geometries on DeltaKth of Small Cracks Emanating from Small Defects, in: Proceedings, The Behaviour of Short Fatigue Cracks, Mechanical Engineering Publications. pp. 275–294.

Nadot, Mendez, Ranganathan, Beranger, 1999. Fatigue life assessment of nodular cast iron containing casting defects. Fatigue Fract. Eng. Mater. Struct. 22, 289–300. doi:10.1046/j.1460-2695.1999.00162.x

Nadot, Y., 2004. Influence of casting defects on the fatigue limit of nodular cast iron. Int. J. Fatigue 26, 311–319. doi:10.1016/S0142-1123(03)00141-5

Nakae, H., Fukami, M., Kitazawa, T., Zou, Y., 2010. Influence of Si , Ce , Sb and Sn on chunky graphite formation. China Foundry 8, 96–100.

Okunnu, R., 2015. High Strength Solution-Strengthened Ferritic Ductile Cast Iron. Aalto University.

Ostensoon, B., 1972. Influence of Microshrinkage Cavities on the Endurance Limit of Nodular Cast Iron. J Iron Steel Inst Sept, 628–631.

Regordosa, A., Llorca-Isern, N., 2017. Microscopic Characterization of Different Shrinkage Defects in Ductile Irons and their Relation with Composition and Inoculation Process. Int. J. Met. 11, 778-789.doi:10.1007/s40962-016-0120-9

Sertucha, J., Suárez, R., Asenjo, I., Larrañaga, P., Lacaze, J., Ferrer, I., Armendariz, S., 2009. Thermal Analysis of the Formation of Chunky Graphite during Solidification of Heavy-section Spheroidal Graphite Iron Parts. ISIJ Int. 49, 220–228. doi:10.2355/isijinternational.49.220

Shinde, V.D., Ravi, B., Narasimhan, K., 2012. Solidification behaviour and mechanical properties of ductile iron castings with varying thickness. Int. J. Cast Met. Res. 25, 364–373. doi:10.1179/1743133612Y.0000000024

Shiraki, N., Usui, Y., Kanno, T., 2016. Effects of Number of Graphite Nodules on Fatigue Limit and Fracture Origins in Heavy Section Spheroidal Graphite Cast Iron. Mater. Trans. 57, 379–384. doi:10.2320/matertrans.F-M2015841

Shirani, M., Härkegård, G., 2014. A review on fatigue design of heavy section EN-GJS-400- 18-LT ductile iron wind turbine castings. Energy Equip. Syst. 2, 5–24.

Shirani, M., Härkegård, G., 2012. Damage tolerant design of cast components based on defects detected by 3D X-ray computed tomography. Int. J. Fatigue 41, 188–198. doi:10.1016/j.ijfatigue.2011.09.011

Shirani, M., Härkegård, G., 2011a. Large scale axial fatigue testing of ductile cast iron for heavy section wind turbine components. Eng. Fail. Anal. 18, 1496–1510.

Shirani, M., Härkegård, G., 2011b. Fatigue life distribution and size effect in ductile cast iron for wind turbine components. Eng. Fail. Anal. 18, 12–24. doi:10.1016/j.engfailanal.2010.07.001

Stets, W., Löblich, H., Gassner, G., Schumacher, P., 2014. Solution Strengthened Ferritic Ductile Cast Iron Properties, Production and Application. Int. J. Met. 8, 35–40. doi:10.1007/BF03355580

Sujakhu, S., Castagne, S., Sakaguchi, M., Kasvayee, K.A., Ghassemali, E., Jarfors, A.E.W., Wang, W., 2018. On the fatigue damage micromechanisms in Si-solution–strengthened spheroidal graphite cast iron. Fatigue Fract. Eng. Mater. Struct. 41, 1–17. doi:10.1111/ffe.12723

UNI EN 1563:2012, Founding - Spheroidal graphite cast irons.

UNI EN ISO 6506-1:2006, Metallic materials - Brinell hardness test - Part 1: Test method.

Weiß, P., Brachmann, J., Bührig-Polaczek, A., Fischer, S.F., 2015. Influence of nickel and cobalt on microstructure of silicon solution strengthened ductile iron. Mater. Sci. Technol. 31, 1479–1485. doi:10.1179/1743284714Y.0000000735

Weiß, P., Tekavčič, A., Bührig-Polaczek, A., 2018. Mechanistic approach to new design concepts for high silicon ductile iron. Mater. Sci. Eng. A 713, 67–74. doi:10.1016/j.msea.2017.12.012

Wessén, M., Svensson, I.L., Aagaard, R., 2003. Influence of antimony on microstructure and mechanical properties in thick-walled ductile iron castings. Int. J. Cast Met. Res. 16, 119–124.

Zhang, Z., Flower, H.M., Niu, Y., 1989. Classification of degenerate graphite and its formation processes in heavy section ductile iron. Mater. Sci. Technol. 5, 657–664. doi:10.1179/mst.1989.5.7.657

Zhou, Jiyang, 2009. Colour metallography of cast iron. China foundry.

List of Publications

Borsato, T., Berto, F., Ferro, P., Carollo, C., 2016. Effect of in-mould inoculant composition on microstructure and fatigue behaviour of heavy section ductile iron castings. Procedia Struct. Integr. 2, 3150–3157. doi:10.1016/j.prostr.2016.06.393

Borsato, T., Ferro, P., Berto, F., Carollo, C., 2016. Mechanical and Fatigue Properties of Heavy Section Solution Strengthened Ferritic Ductile Iron Castings. Adv. Eng. Mater. 18, 2070–2075. doi:10.1002/adem.201600256

Borsato, T., Ferro, P., Berto, F., Carollo, C., 2017. Fatigue strength improvement of heavy-section pearlitic ductile iron castings by in-mould inoculation treatment. Int. J. Fatigue 102, 221–227. doi:10.1016/j.ijfatigue.2017.02.012

Borsato, T., Ferro, P., Berto, F., Carollo, C., 2017. Mechanical and fatigue properties of pearlitic ductile iron castings characterized by long solidification times. Eng. Fail. Anal. 79, 902–912. doi:10.1016/j.engfailanal.2017.06.007

Borsato, T., Ferro, P., Berto, F., Carollo, C., 2017. Fatigue properties of solution strengthened ferritic ductile cast irons in heavy section castings. Metall. Ital. 109, 25–32.

Borsato, T., Ferro, P., Berto, F., 2018. Novel method for the fatigue strength assessment of heavy sections made by ductile cast iron in presence of solidification defects. Fatigue Fract. Eng. Mater. Struct. 41, 1746-1757.

Borsato, T., Ferro, P., Berto, F., Carollo, C., 2018. Influence of solidification defects on the fatigue behaviour of heavy section silicon solution strengthened ferritic ductile cast irons. Fatigue Fract. Eng. Mater. Struct. 41, 2231-2238.

Borsato, T., Ferro, P., Berto, F., Carollo, C. Effect of section thickness and solidification time on microstructural, mechanical and fatigue properties of solution strengthened ferritic ductile iron. (under review).

Conferences:

21st European Conference on Fracture, ECF21, 20-24 June 2016, Catania, Italy. "Effect of in-mould inoculant composition on microstructure and fatigue behaviour of heavy section ductile iron castings".

36° Convegno Nazionale AIM 21-23 settembre 2016, Parma, Italy. "Influenza dei lunghi tempi di solidificazione sulle proprietà meccaniche e microstrutturali di ghise sferoidali rafforzate per soluzione solida".

ICF14 14th International Conference on Fracture, Rhodes, Greece, June 18-23, 2017. "Characterization of heavy section ductile irons critical radius based on SED approach".

Fatigue 2017, 7th International Conference on Durability and Fatigue, Downing College, University of Cambridge, 3rd-5th July 2017. "Fatigue properties of solution strengthened ferritic ductile cast iron in heavy section castings".